Photon correlations on a room temperature semi-conductor single photon emitter.

Samir Bounouar

UNIVERSITÉ DE GRENOBLE

THÈSE

Pour obtenir le grade de

DOCTEUR DE L'UNIVERSITÉ DE GRENOBLE

Spécialité : **Physique**

Arrêté ministériel : 7 aout 2006

Présentée par

Samir BOUNOUAR

Thèse dirigée par **K. Kheng**
et codirigée par **J.P. Poizat**

préparée au sein **de l'Institut Néel**
et de **l'Université de Grenoble**

Corrélation de photons sur un émetteur de photons uniques semi-conducteur à température ambiante

Thèse soutenue publiquement le **6 Février 2012**,
devant le jury composé de :

Mr Guillaume Cassabois
Professeur de l'Université Montpellier II, Rapporteur
Mr Jean-Pierre Hermier
Professeur de l'Université de Versailles Saint Quentin, Rapporteur
Mr Michel Orrit
Professeur de l'Université de Leiden , Examinateur
Mr Xavier Marie
Professeur de l'INSA Toulouse , Examinateur
Mr Kuntheak Kheng
Professeur de l'Université Joseph Fourier, Directeur de thèse
Mr Jean-Philipe Poizat
Directeur de recherche, Institut Néel, Co-Directeur de thèse

b

UNIVERSITÉ DE GRENOBLE

THÈSE

Pour obtenir le grade de

DOCTEUR DE L'UNIVERSITÉ DE GRENOBLE

Spécialité : **Physique**

Arrêté ministériel : 7 aout 2006

Présentée par

Samir BOUNOUAR

Thèse dirigée par **K. Kheng**
et codirigée par **J.P. Poizat**

préparée au sein **de l'Institut Néel**
et de **l'Université de Grenoble**

Corrélation de photons sur un émetteur de photons uniques semi-conducteur à température ambiante

Thèse soutenue publiquement le **6 Février 2012**,
devant le jury composé de :

Mr Guillaume Cassabois
Professeur de l'Université Montpellier II, Rapporteur
Mr Jean-Pierre Hermier
Professeur de l'Université de Versailles Saint Quentin, Rapporteur
Mr Michel Orrit
Professeur de l'Université de Leiden , Examinateur
Mr Xavier Marie
Professeur de l'INSA Toulouse , Examinateur
Mr Kuntheak Kheng
Professeur de l'Université Joseph Fourier, Directeur de thèse
Mr Jean-Philipe Poizat
Directeur de recherche, Institut Néel, Co-Directeur de thèse

d

Sommaire

Introduction

The union of quantum mechanics and information science opened the way to quantum information which gave rise to numerous fundamental advances and powerful applications. In this broad field, single photon emitters are promised to a central place. Since the theory and the demonstration of the sub-poissonian emission from atoms by J. Kimble, L. Mandel and M. Dagenais[1, 2],the realization of two photons interferences[3], single photons proved to be essential to convey quantum information [4, 11], and to be the best candidates for the implementation of quantum networks[5], and for the realisation of quantum computing operations[12]. Early works on atoms and ions proved they were very well suited systems for proof of principle demonstrations, but they lack integration possibilities, for their use in technological developpement and in real life. Therefore, the need for more suitable alternatives forced the community to investigate new systems in solid state physics.

Researchers produced large efforts to provide nanoscale condensed matter systems, able to emit single photons on demand in a scalable, robust, and practical way. In this quest, they developped a very large variety of different emitters such as nitrogen vacancy centers, nanocrystals, molecules and semiconductor quantum dots. These systems proved to be very efficient single photon emitters, but showed diverse performances regarding the three main requirements: tunability, robustness, and stability.

The strength of condensed matter systems is their tunability. Engineering on solid state system provide the possibility to change the properties of the emitter at will. The colour of photons emitted by nanocrystals is determined by their size and can cover wavelength ranging from infrared to UV[6]. This is also true for semi conductor quantum dots, and the wide range covered by the possible emission energies is made accessible by the variety of semi-conductor materials which can compose the quantum dot. Even if such considerations are often overlooked, the nanometric size of these structures are also bringing important processes dominating their physics: carriers-phonon coupling, exchange interaction between confined carriers spins or coupling between carriers and magnetic spins eventually inserted in or outside the quantum dot. However, the control of the size and of the semi-conductor composition is limited by the growth conditions imposed by the conventionnal Stranski-Krastanov (SK) method. The quantum dots are self-assembled by release of elastic energy accumulated by lattice mismatch between the semiconductor host matrix and the quantum dot semi-conductor. Thus, control of the quantum dot dimensions is difficult. Alternative techniques enabling growth of quantum dots embedded in nanowires are suppressing these limitations, allowing a large choice of the composing materials, and offering, in principle, the possibility to tune the quantum dots dimensions: they are putting scalability of semiconductor heterostructures at a higher level.

For the second one, robustness, nitrogen-vacancy centers and nanocrystals showed remarquable successes, in particular for their ability to operate at room temperature[7, 8, 9]. Semiconductor quantum dots showed interesting potential in this domain but occurence of effective non-radiative processes and correlated emissions of photons coming from different transitions

of the same quantum dot created some limitations in the use of these objects as reliable single photon emitters at high temperature. Large efforts, in the optimisation of existing growth processes, in the developpement of very confining heterostructures and in the diversification of growth modes, have been devoted to overcome these difficulties. In this aspect, fabrication of quantum dots embedded in nanowires obeys to very different rules than self assembled quantum dots. In addition to being less restrictive in the choice of the materials, quantum dots are no longer interconnected by a 2D layer (wetting layer), cutting off one of the main channel for escape of the carriers. This is a very promising feature, combining important confinement and potential good resistance against temperature.

The weak point of condensed matter systems is their stability. The environnement is highly influencing the emission of these objects. The interaction of the emitter with the numerous degrees of freedom of the surrounding solid leads to random fluctuation of the emission energy and eventually to blinking. Coupling of the emitter with phonon modes in the crystal creates a dephasing, which is not linked to a loss of population of initial state of the radiative transition. The effect of this coupling gets worst when temperature is increased and transition energy linewidths become extremely large. Fluctuations of the electronic environnement are also a source of dephasing. This random Stark-shift of the emission energy is called spectral diffusion. In opposition with phonon coupling, which is a non correlated process, spectral diffusion is time correlated and it is is a reasonable approximation to considere it as a Markovian process. Thus, these two different random processes, with two different statistics, are major obstacles to any two-photons interference operation, and therefore to the use of condensed matter systems for quantum computing. They can even lead to problems in the use of semi-conductor quantum dots to more simple single photons applications like quantum cryptography and can be the source of the blinking phenomen in nanocrystals, leading to long periods of time with no emission.

The work proposed in this thesis is based on the use of the photon correlation technique. It is known since the pioneer works on the correlation of the light by Handbury-Brown and Twiss (HBT) that such experiments give access to the emission statistic of the studied object [10]. Slight modification of the original HBT setup gives access to the correlation between photons emitted by different transitions of the same quantum dot. And by pushing further this technique, one can also have access to the emission energy statistic. Results obtained in this thesis are, in some way, very specific to the optical properties of the studied object - ZnSe/CdSe nanowire quantum dots- but in some points, they are general to condensed matter systems and they are strongly related to the three key issues addressed above.

This manuscript is organized as follows:

- In the first chapter, we will recall the most basic notions about semiconductor nanowire quantum dots and the quantum treatment of light detection and correlation.

- In the second chapter, we present the dynamic of neutral nanowire quantum dots, and in particular the influence of the dark exciton states, and the exciton- phonon coupling efficiency on the emission.

- In the third chapter, we present the use of such neutral quantum dots as single photon emitters at room temperature: this is the first time epitaxied quantum dots reach this achievement. We discuss the causes of the limitations of their performances as a single photon emitter, and explain the obtention of this result by investigating their optical properties, in particular with temperature.

- The fourth chapter is devoted to the dynamic of charged quantum dots, leading to conclusions about the spin relaxation of the excited trion, the measurement of the p-hole spin flip time, and giving some indication on the possible doping nature of the quantum dot.

- In the last chapter, we investigate the spectral diffusion problem by photon correlation tech-

nique. By a theoretical work, we show that the measured halfline auto-correlation function bears at the same time the signature of the sub-poissonian emission (anticorrelated) of the quantum dot, the correlated first order Markovian (short memory) emission energy fluctuation and the (uncorrelated) Poissonian emission energy of the homogeneous linewidth, imposed by radiative lifetime and phonon braodening. After describing the different signatures of these combined energy and emission processes on the correlation function, we explain how to extricate the correlated and the uncorrelated processes, and experimentally determine separately the homogeneous linewidth and the fluctuation amplitude due to the spectral diffusion. Finally, we apply this work on nanowire quantum dots by performing temperature and power dependent experiments. This led us to conclusions on the energy statistic of the emitter at high temperature, and by interpretations using the Kubo-Anderson model, we also conclude on the environnement fluctuations behaviour when the two parameters (temperature and power) are changed.

Chapter 1

Introduction

In this introduction chapter, we will recall the basic ideas necessary for the good understanding of this manuscript. First, we'll briefly describe the structure of the single photon emitter used for the following studies, its characteristics and advantages. Then, we will give a few theorical and experimental elements on the quantum treatment of light detection and correlation, containing the basics of the work we will present in the other chapters.

1.1 Nanowire quantum dots

1.1.1 Semiconductor nanostructures

Band structure of a II VI semiconductor compound

II VI semiconductor materials are composed by two elements, each of them characterized by their 4 external levels (1 type S and 3 type P). Hybridisation of these atomic orbitals result in 4 bounding states (1 S orbital and 3 P orbitals) and 4 anti-bounding states (1 S and 3 P orbitals). The type II element (Cd,Zn) has two electrons on its external layer and the type VI (Se) has 4 electrons. The 4 bounding orbitals are populated by the 6 electrons and form the valence band. The 4 antibounding orbitals are initially empty. The lowest empty state is the antibounding S orbital. It is the conduction band. The energy between the conduction and valence band is defined as the energy bandgap E_g (1.7 eV for CdSe and 2.7 eV for ZnSe)

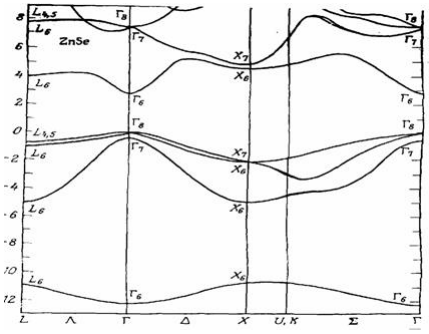

Figure 1.1: ZnSe Band structure

The optical properties of the material are controlled by the bands symetry at k=0 (the so called Γ point). Electrons, belonging to the the conduction band, formed by the S antibounding orbital, have an angular momentum null and their total angular momentum is J=1/2 .

For the valence band, the spin orbit coupling lifts the degeneracy at k=0 between states of total angular momentum J=1/2 and J=3/2 coming from the P angular momentum L=1 of the P bounding states and the spin 1/2. Thus, the valence band is decomposed in two level groups: a J=3/2 quadruplet and a J=1/2 doublet separated by a spin orbit coupling energy Δ_{so} .

For the conduction band, around k=0, one can describe the dispersion relation by a parabolic approximation:

$$E(k) = E_g + \gamma_c \frac{\hbar k^2}{2m_0}$$

where m_o is the free electron energy. The effective mass of the electron in the material is $m_e^* = m_o/\gamma_c$.

Excitation of a semi conductor material

By laser excitation or electrical excitation one can promote in the conduction band an electron residing on the valence band. The result is a system composed by a J=1/2 electron on the S type conduction band and an absence of electron in the P type valence band. This is the hole particle. It can be described as a quasi-particle of total angular momentum J=3/2 (heavy hole) or J=1/2 (light hole) and effective mass $m_h^* = m_o/\gamma_v$.

The resulting electron and hole are interacting via Coulomb interaction, which lowers the energy of this complex called "exciton". This system can be described by a Schrodinger equation similar to the hydrogen atom.

$$\left[\frac{p_e^2}{2m_e^*} + \frac{p_h^2}{2m_h^*} - \frac{q^2}{4\pi\epsilon\epsilon_o \mid r_e - r_h \mid}\right] \psi(r_e,r_h) = E.\psi(r_e,r_h)$$

The solutions of this equation are well known and it is easy to derive the energy and the effective Bohr radius of the 2 particle system:

$$a^* = \frac{a_0.\epsilon.m_0}{\mu}$$

with $\mu = \frac{1}{m_e^*} + \frac{1}{m_h^*}$, the reduced mass, $a_0 = 0.0529nm$ the Bohr radius of the Hydrogen atom, ϵ the material dielectric constant. In bulk CdSe the Bohr radius has been measured at 5.6 nm. This value is important as it defines for which dimension it is possible to confine the exciton, which is necessary to impose to this particle a discrete density of state and create a quantum dot.

Confinement of the carriers

It exists a few way of reducing the dimensions of a semi-conductor. By creating small particles of semi-conductor materials as for the colloidal quantum dots, or by inserting a small gap semi conductor in a larger gap semi conductor, one can realize different confinements from quantum wells to quantum wire or quantum dots. Thus by reducing the confinement dimensions from bulk to the order of the Bohr radius, one confine the exciton and make its energy discrete.

The full calculation of the exciton energy in a quantum dot requires to take into account the confinement energy of the hole and the electron, to consider effective mass anisotropy of the hole, strain contributions, and an evaluation of the binding energy. This calculus is relatively challenging and is most commonly done by a variational calculation [13]. The result is highly influenced by the confinement potential considered. The most simple and efficient are the finite

or harmonic confinement, but as the real confinement potentials of the quantum dots are rarely well known they only provide approximated values.

One can experimentally probe this value by spectrally analyzing the photons coming from the recombination of the exciton. As in a quantum dot it has a discrete density of states, one expect a very sharp band emission energy. As electrons and holes are fermions of total angular momenta projection $\pm\frac{1}{2}$ or $\pm\frac{3}{2}$, one can put at maximum 2 carriers on the same confined level. The resulting combinations of charges in the quantum dots are compiled in fig. 1.2. The exciton can coexist with an extra carrier: it is the charged exciton. When the exciton recombination happens in the presence of an extra carrier, the emission energy is shifted because of Coulomb interaction between the exciton and the charge. Thus one can separate spectrally the emission of the different possible combinations of charges in the quantum dot. The same way, the biexciton is the presence of two excitons at the same time in the quantum dot and the charged biexciton is composed by two excitons and an extra carrier in the P shell.

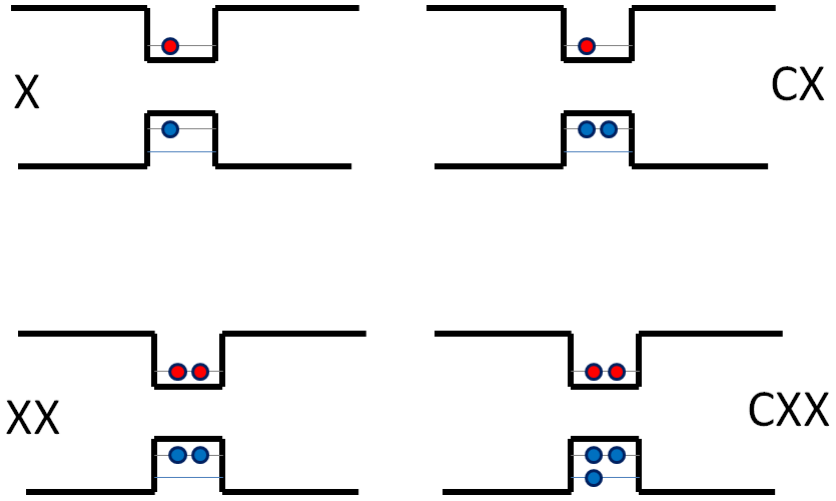

Figure 1.2: Different states of a quantum dot

1.1.2 Nanowire quantum dots growth

There are a few methods to grow epitaxied quantum dots. The vast majority of reports on epitaxied quantum dots were done on self assembled systems. However, some alternatives exist, and nanowire quantum dots proved to be a very credible and advantgeous method in many aspects.

SK growth method

This the most common and investigated method to produce self assembled quantum dots. These quantum dots are fabricated by epitaxial growth of one type of crystal on top of another. If the lattice constants differ noticeably (e.g. In(Ga)As/GaAs), small islands of the top material are formed to minimize the strain. This growth mode is called Stranski-Krastanov growth. Finally the islands are additionally overgrown by the substrate material to form quantum dots. Depending on the underlying semiconductor materials, self-assembled quantum dots can cover a broad spectral range from ultra-violet to the infra-red regime. The wetting layer forms a

quantum well, which usually shows photoluminescence above the quantum dot emission energy. Finally the islands are overgrown by the substrate material to form quantum dots.

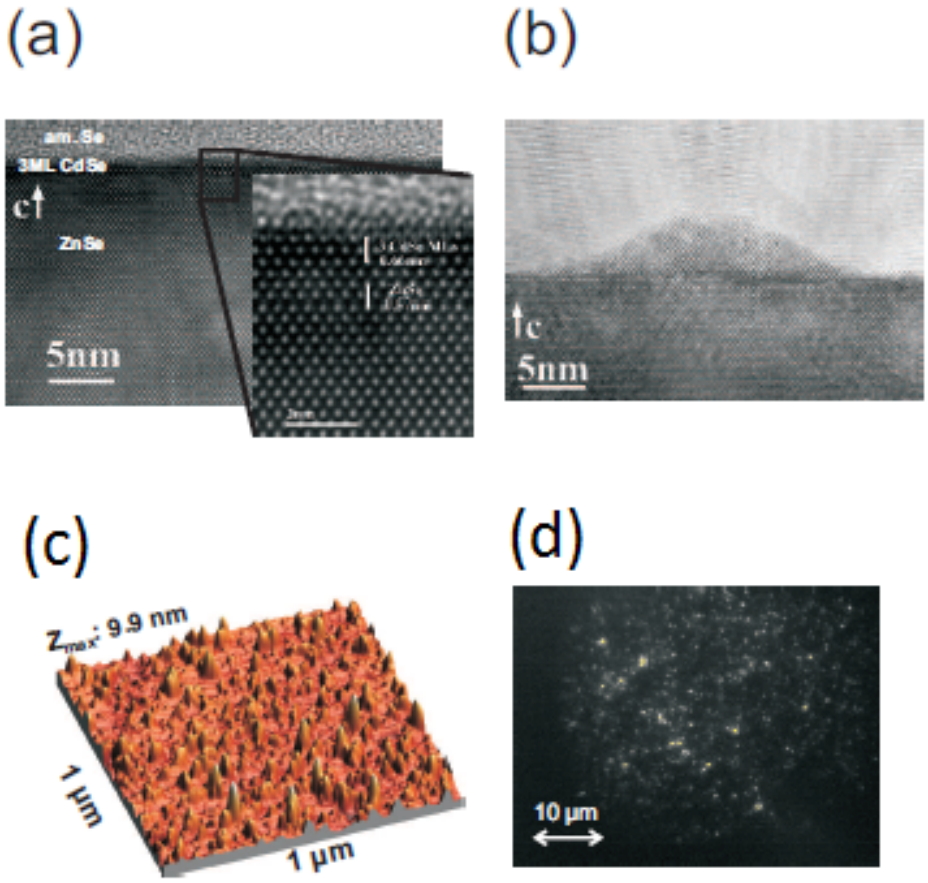

Figure 1.3: (a) TEM image of a CdSe layer on ZnSe below the critical thickness (3 ML). (b) Above the critical thickness it relaxes by forming a QD. (c) AFM image of CdSe QDs distributed on a ZnSe surface. (d) Micro-photoluminescence image of InP quantum dots in GaInP. The image was taken through a bandpass filter to suppress excitation stray light. (a)–(c) taken from [22], (d) from [23]

Despite being the most used growth method for epitaxied quantum dots, a few noticeable disadvantages exist. As the quantum dots are self-assembled, there is no control of their size or shape. Secondly, as the quantum dots are surrounded by a wetting layer, that may introduce undesired non-radiative decay channels. Finally, this is very uneasy to control the spatial density of the quantum dot, and one usually need some processing, as etching or masks to achieve single quantum dot spectroscopy.

All these problems mostly don't exist in the growth method of nanowire quantum dot that is exposed in the next section, the VLS method.

VLS growth method.

The growth of the sample from where are extracted all the results presented in this manuscript was performed by Miryam Elouneg Jamroz. We briefly describe here the VLS method used for

the growth of the nanowires.

The Vapour-Liquid-Solid (VLS) growth method is the most frequently employed technique for the growth of semi-conductor nanowires[15, 16]. Starting from 1990s, this technique was employed by many researches to form nanowires and nanorods from a rich variety of materials: elemental semiconductors[17, 18] , III-V semiconductors [19], II-VI systems [20], and oxides[21]. The employed growth techniques comprise diverse epitaxial methods, such as Chemical Vapor Deposition (CVD) , or Molecular Beam Epitaxy (MBE).

In the VLS method, one starts with nanometer-sized metal particles, that are deposited on the surface. During the growth, the substrate is heated above the melting point of the metal nanoparticles to a temperature at which it forms an eutectic phase with one of the epitaxial semiconductor reactants. The continued feeding of the semiconductor atoms into the liquid droplet supersaturates the eutectic. This alloy acts as a reservoir of reactants, which favorites the growth at the solid-liquid interface and thus forms a one-dimensional nanowire with the alloy droplet remaining on the top. The size of the metal particle also affects the diameter of the nanowire and its growth speed [21].

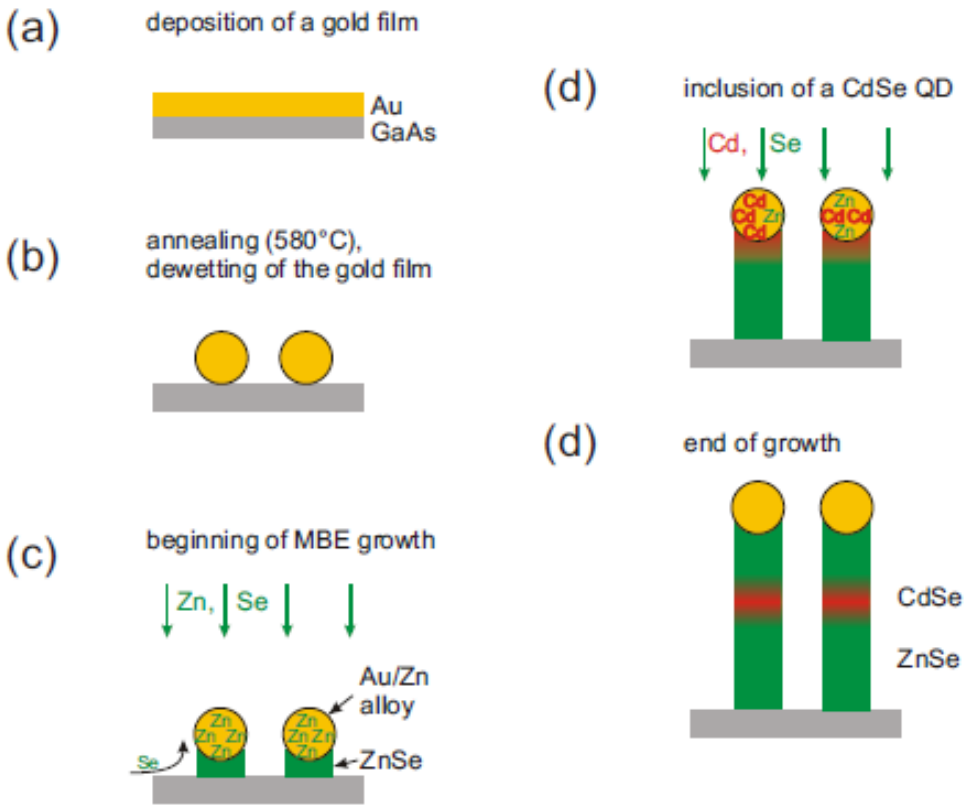

Figure 1.4: ZnSe nanowire growth process via MBE VLS method

fig. 1.4shows the growth process on the example of MBE grown ZnSe nanowires. It started with the desoxidation of a GaAs (100) wafer at high temperature (>640°C) followed by MBE growth of a (>300nm) GaAs layer (100) in a III-V MBE chamber and a ~30nm ZnSe (100) thin film in a II-VI MBE chamber. ZnSe surface is chosen to initiate the growth of the NWs, to benefit from homoexpitaxy and promote oriented nanowire growth, and also to shield the NWs

from potential Ga and As dopants. A small amount of Au was then evaporated onto the surface in a separate chamber and the sample was returned to the II-VI chamber where the Au film was dewetted at 510°C for 20 min. Finally the sample temperature was lowered to 410°C and the rotating sample was exposed to fluxes of Zn and Se for 20 min to obtain the nanowires. The CdSe QD segment of the nanowires was achieved at the 15th minute of growth simply by switching the Zn flux for a Cd flux for 30 s. The fluxes were 3.4(Zn), 2.2(Cd), 10(Se) x10-7 Torr. The entire process was performed under UHV conditions. This recipe permitted to obtain low density ($15/\mu m^2$), homogeneous 10 nm diameter nanowires, with a length of around 200 nm (see fig. 1.5) . The low density was a crucial condition for the nanowires not being in competition during the growth.

Some recent studies showed some indications that the growth process could actually be VSS (Vapor solid solid) with the gold catalyst being solid instead of liquid as in the classical VLS method. This work is in progress and is out of the scope of this manuscript.

1.1.3 Microscopy characterization

We give here a short outlook of microscopy experiments used to help the growth and obtain structural informations about the nanowire quantum dots. It has to be mentioned that all the microscopy work presented here was performed by Martien Den-hertog.

SEM microscopy

Several advanced microscopy techniques were used. In fig. 1.5, in the SEM Top view and in the perpendicular SEM view, we can see the "as grown" nanowires growing along 2 directions. They tend to grow mostly in the Zn-terminated B direction of the substrate crystal for reasons that are still unknown, and a smaller fraction grows vertically along the (100) direction.

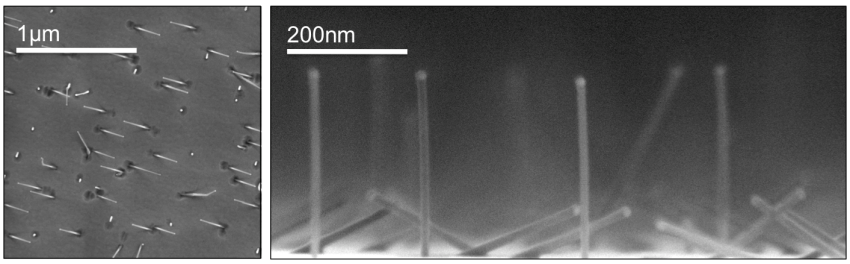

Figure 1.5: ZnSe/CdSe/ZnSe NWs grown a ZnSe buffer. a, Top view SEM image showing a majority of uniform NWs inclined respect to the substrate surface. The bright dots are the NWs standing straight up. b, Perpendicular SEM view of the same sample.

HRTEM

The Nanowires were studied by high resolution transmission electron microscopy (HRTEM) and high resolution high angle annular dark field scanning TEM (HAADF STEM)[24]. fig. 1.6 presents the HRTEM image of a full NW from the ZnSe substrate to the gold particle. Its diameter, constant all along the NW, is of 10nm. Generally the NWs have the [0002] hexagonal wurtzite (WZ) structure with numerous stacking fault defects and some small regions with the [111] cubic zinc blende (ZB) crystal structure, as shown in fig. 1.6 a-b.The Geometrical Phase Analysis (GPA) technique can be used on HRTEM images of NWs to map the interplanar spacing along the wire axis. Since the CdSe (0002) interplanar spacing (0.350nm) is larger than the ZnSe

interplanar spacing (0.327nm) this technique allows us to obtain the size of the QD and its localization along the NW. The GPA analysis of the whole NW reveals no change of lattice space all along the wire except in a region at about 120nm from the gold particle (Fig. 3c). That corresponds to the estimated position of the CdSe quantum dot. The interplanar change obtained from a line profile along this region (Fig. 3e) indicates that in fact the QD is not the pure CdSe compound but a ZnxCd1-xSe ternary alloy as its maximum is smaller than the value of pure CdSe. The QD size is estimated as the full width half maximum of the interplanar lattice spacing along the growth direction of the peak obtained by the GPA analysis. It varies between 2.5 and 4 nm and four out of five observed QDs had a size of 3.7 to 4 nm.

These measurements were done on the sample giving the best optical results. Some others were done on the many previous samples, and permitted to make a correlation between the optical and the microscopic measurements, from sample to sample.

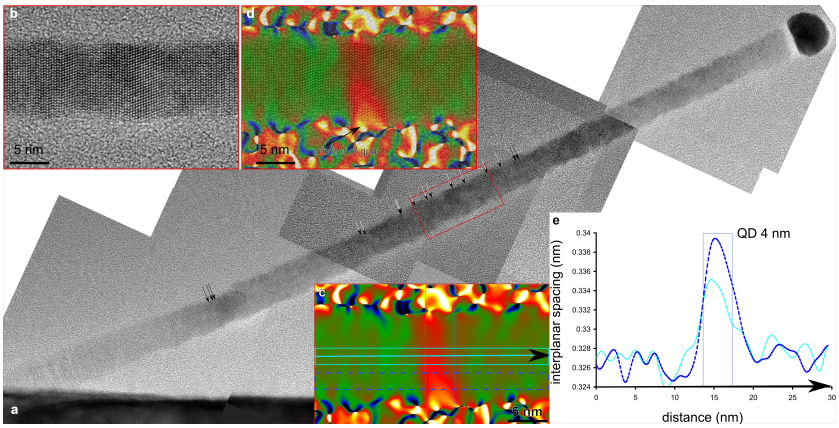

Figure 1.6: Structural analysis by transmission electron microscopy of a single ZnSe/CdSe/ZnSe NW. a, series of HRTEM images along the whole NW. stacking faults and small cubic regions are indicated by arrows. b, HRTEM of the boxed region in a. c, geometrical phase analysis of the growth plane. d, overlay of the gpa map on the HRTEM image. e line profiles made in c along the arrow (line profile) and along the dashed boxed region (dashed profile), taken from reference [24].

Optical and microscopy correlation

In fig. 1.7 is presented the luminescence energy of quantum dots coming from different samples. There is a correspondence between these energies and the size of quantum dots determined by HRTEM techniques. Indeed, the results of models taking into account a mixed composition of the CdSe quantum dots, and measured quantum dot sizes are fitting the experimental datas. Despite the dispersion of measured quantum dot sizes, and the difficulty to make this kind of measurements on more than a few nanowires per sample, it confirms the validity of the microscopy work by optical measurements.

For the sample giving the best optical performances, and for the others, the best fit is given by the 60% Cd concentration quantum dot curve. This result is also confirmed by EDX measurements (chemical composition) showing lower Zn presence in the Quantum Dot area.

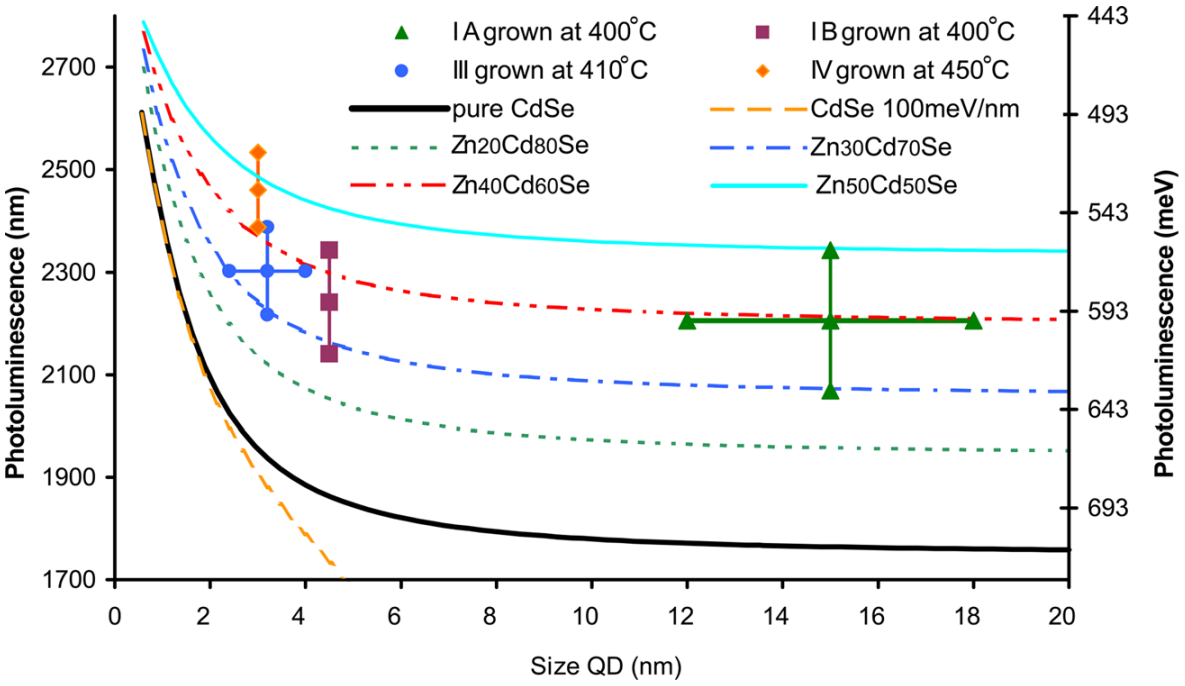

Figure 1.7: Photoluminescence energy vs QD size for different samples. Size error bars are based on the distribution of values obtained by TEM observations, and energy errors bars are based on the PL emission range of a given sample. Calculations were done by Regis Andre.

1.1.4 Sample preparation

Substrat lithography

For single quantum dot spectroscopy, it is necessary to mark the substrates with reperes. It was done by optical lithography on silicon wafers.

A negative resine was spread on the masked substrate before insulation with deep UV flashes. After titanium and gold deposition and lift off, we obtained μm size gold plots organized in an marked pattern.

Nanowire depositions

Nanowire were dispersed on the silicon marked substrate by direct contact with the as grown sample and rubbing. The result is a non homogeneous disposition of the nanowires with areas of high density of nanowires but with numerous low density areas fig. 1.9, with one or two luminating nanowires in the beam spot.

1.1.5 Photoluminescence setup

In this section we describe the elements of the basic photoluminescence setup(see fig. 1.10) .

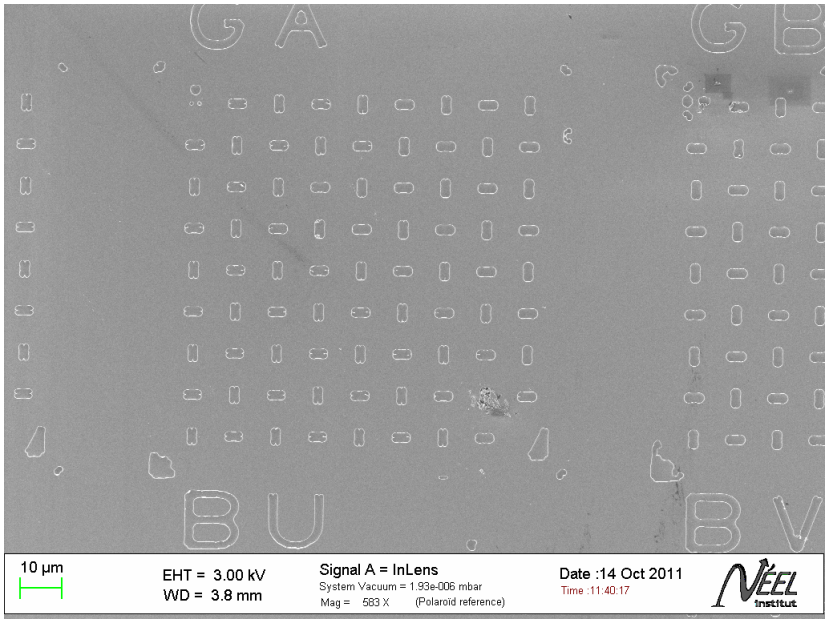

Figure 1.8: Lithography pattern

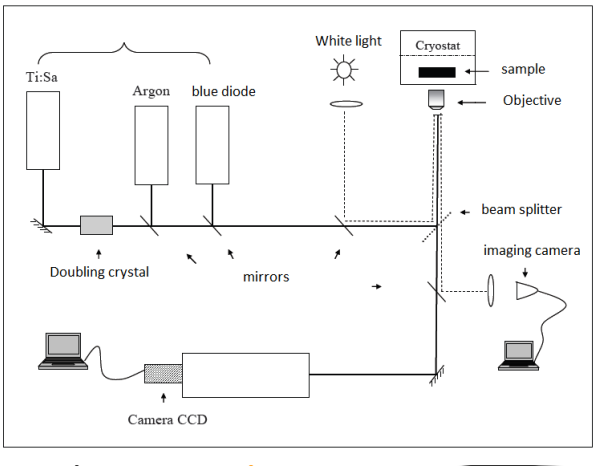

Figure 1.10: Basic photoluminescence setup

Excitation lasers

Three different lasers were available for our experiments.

A continuous 405 nm blue diode, a 475 nm monomode laser, and an near infra red Ti-Sa Laser. For pulsed excitation, the latter can be used in pulsed regime with Pulse time width 1ps and a repetition rate of 80Mhz. As the studied quantum dots are emitting in the visible range, we need to double its frequency (divide by two the wavelength) with the help of a non linear LBO doubling crystal. It is wavelength tunable and we can provide sharp-band excitation from 400nm to 590nm.

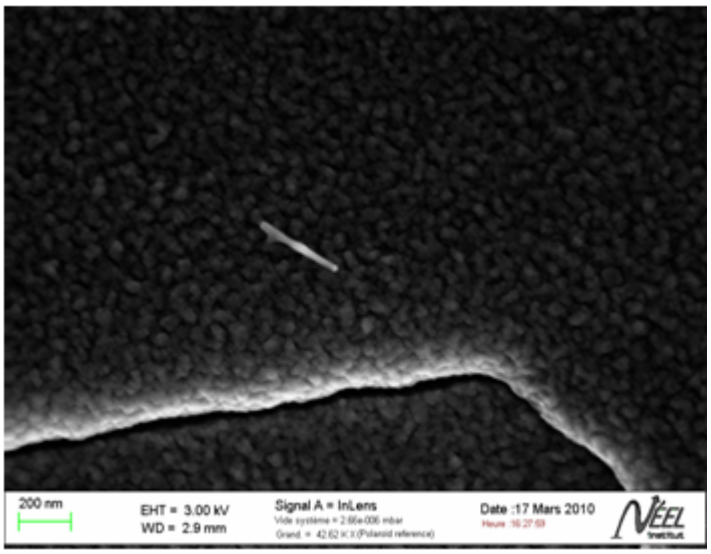

Figure 1.9: nanowires after deposition

Polarizers and densities

Lasers being linearly polarized, $\lambda/2$ polarizers are placed in the excitation and detection path. Nanowires are strongly linearly polarized along the direction of the nanowire [31] and to optimize the detection and excitation efficiency, one need to control the polarizations. On the contrary, as explained in the previous section, nanowires are seen by the side, thus we have no acces to the circularly polarized fine exciton structure and no circular polarizer is used in this work.

In addition, to precisely control excitation power, an additional $\lambda/2$ polarizer and a polarization selecter are coupled on the excitation path. For rough power tuning, one use optical densities.

Cryostat

Two different cryostats were used in this work.

The He microstat is a Helium circulation cryostat, highly adaptated to optical experiments involving high temperatures, requiring high stability, in time and in temperature. The latter qualities were crucial for experiments requiring very long integration times and performed at room temperature. Such performances are obtained because Helium is circulating directly around the sample and there is no long coldfinger connecting the helium and the sample, introducing large inertie to temperature and mechanical dilatations, which affect the stability. For rough displacement of the excitation along the sample, the cryostat is mounted on micrometer stages and for fine position optimization, Piezolelectric controls are implemented.

Objective

This is an Olympus NA =0.4 objective. This relatively weak numerical aperture is due to long working distance. It is however not well optimized for the photons correlation experiments exposed in this thesis, as integration time depends quadratically on the collected intensity. Fortunately, nanowire quantum dots are very efficient emitters, which permitted many different

photons correlation measurement with no major difficulty. Only the beam splitter (T=92%, R=8%) was chosen to increase the collection efficiency.

Spectrometers

Two spectrometers were used in this work. The first one is a 500 SI/SM of 50 cm focal Chromex spectrometer. Two gratings were used for high resolution (1200 gr/mm) and low resolution (150 gr/mm) spectroscopy. The second one is a 50 cm focal IHR 55 with same resolution gratings.

Combined with respectively an Andor (1024 lateral pixels) and a PIXIS camera (1340 lateral pixels), both of them have approximately the same spectral resolution ($\sim 200\mu eV$).

Avalanche photodiodes

The choice of photodetectors for the correlation experiments is very important. For high resolution experiments, we use Idquantique 40 ps resolution APD's. They are very useful to probe very fast phenomenons, especially for cross-correlation experiments. They are also a little more difficult to use as their detection chip is small (20 μm diameter) and require attention for the choice of the optics focusing the collection beam on it.

For low time resolution experiments, we use Perkin Elmers APDs, with 400 ps resolution. They allow to probe phenomenons in the nanoscale range and are very easy to align as their detection ship is 250 μm of diameter. The main interest of these APD's is that their quantum efficency is twice larger (55% at 550 nm) than the efficiency of the fast APD's.

1.2 Quantum treatment of light detection and correlation

The light coming from the single photon emitter, we described above is a special type of emission. We are now interested in how it is possible to detect and measure correlation of the outcoming light. In our particular case, the semi-classical theory of light detection is not appropriate. As we will see, the sub poissonian emission statistic is the result of a the quantum mechanical state of the optical field, and to describe it properly, we have to give the main elements of the quantum light detection theory, and also the experimental setup used to obtain evidence of such statistic.

1.2.1 Detection probability

Our photons detectors are using the photoelectric effect: light falls on a metallic or semiconductor surface, which sometimes makes bound electrons being released from the metal: they are the photoelectrons. If a positively charged electrode is placed near the photoemissive cathode so as to attract photoelectrons, an electric current can flow in response to the incident light (fig. 1.11). The device therefore becomes a photoelectric detector.

In the assumption that the incident light is in a coherent state $\mid \{\nu\}\rangle$, it can be shown that the probability of detection of the light by one electron is [25]:

$$P_{1e}(r,t,\Delta t) = \eta I(r,t)\Delta t,$$

with η the detection efficency, Δt the detection time and $I(r,t)$ the intensity of the light at position r and time t.

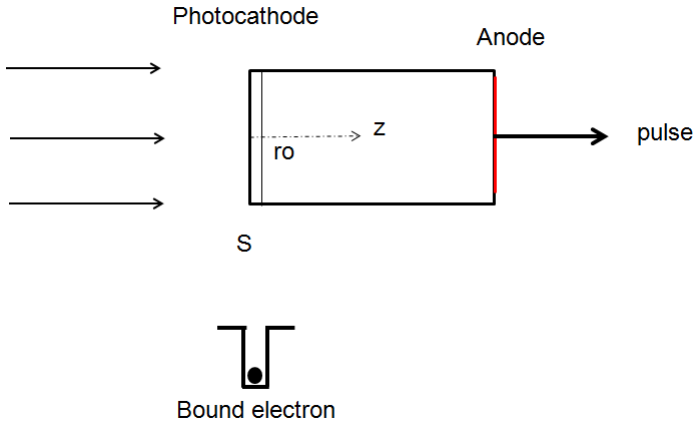

Figure 1.11: Idealized photodetector with a bound electron in a potential well

The probability $P(r,t,\Delta t)$ of photodetection by one or more of the N bound electrons is given by the binomial sum

$$P(r,t,\Delta t) = \sum_{n=1}^{N} C_N^n \left[\eta I(r,t)\Delta t\right]^n \left[1-\eta I(r,t)\Delta t\right]^{N-n}$$

If $N\eta I(r,t)\Delta t \ll 1$, the dominant term in the series is the first and:

$$P(r,t,\Delta t) \approx N\eta I(r,t)\Delta t \tag{1.1}$$

More generally, η measuring the likelihood of detection by one electron may not be the same for all electrons but may depend on the position r within the cathode. We should replace eq. 1.1 by a more general integral relation:

$$P(r_0,t,\Delta t) = \int g(r)\eta(r)I(r,t)\Delta t.d^3r,$$

in which $g(r)$ is the bound electron density and r_0 is the midpoint of the cathode. If g is constant and η and I vary only with the z position,

$$P(r_0,t,\Delta t) = Sg\int_0^{\delta z} \eta(z)I(z,t)\Delta t.dz$$

for $I(z,t) = I(r_0,t)f(z)$,the detection probability takes the form

$$P(r_0,t,\Delta t) = \alpha cSI(r_0,t)\Delta t = AI(r_0,t)\Delta t,$$

where

$$\alpha = (g/c)\int_0^{\delta z} \eta(z)f(z)dz$$

the dimensionless quantum efficiency of the detector.
The detection probability is proportional to Δt , then we will write the detection probability:

$$P(r,t,\Delta t) = P_1(r,t)\Delta t$$

with the understanding that P_1 is a probability density.

To calculate the photodetection probability on the two different photodetectors, one need to calculate the photodetection probability for the first one at t_1 , which is on the form $A_1 I(r_1, t_1)\Delta t_1$, to take the state after the first detection, and calculate the photodetection probability on the second detector at t_2 . But as the initial state was taken to be a pure coherent state, the state remains unchanged after the first detection. Thus the joint probability can be written:

$$P_2(r_1, t_1; r_2, t_2)\Delta t_1 \Delta t_2 = A_1 I(r_1, t_1)\Delta t_1 . A_2 I(r_2, t_2)\Delta t_2 \tag{1.2}$$

To generalize the last expression to any initial state (not necessarily a pure coherent state), we can consider that we have to deal with an ensemble of coherent states. If each realization $|\{\nu\}\rangle$ of the ensemble is characterized by a weight $\phi(|\{\nu\}\rangle)$, so that the initial density operator ρ_F of the field is:

$$\rho_F = \int \phi(|\{\nu\}\rangle)\,[|\{\nu\}\rangle\langle\{\nu\}|]\,d\{\nu\}\,.$$

We can rewrite the joint probability given by fig. 1.2:

$$\begin{aligned} P_2(r_1, t_1, \Delta t_1; r_2, t_2, \Delta t_2) &= \int \phi(|\{\nu\}\rangle) A_1 I(r_1, t_1)\Delta t_1 . A_2 I(r_2, t_2)\Delta t_2 d\{\nu\} \\ &= \langle A_1 I(r_1, t_1)\Delta t_1 . A_2 I(r_2, t_2)\rangle_\phi \\ &= A_1 A_2 \langle I(r_1, t_1) I(r_2, t_2)\rangle_\phi \Delta t_1 \Delta t_2 \end{aligned}$$

We now make use of the so-called optical equivalence theorem, which asserts that the expectation value of any normally ordered field operator can be written as an ensemble average, in which the creation and annihilation operators are replaced by their left and right eigenvalues and the average is taken with the space functional $\phi(\{\nu\})$ used as weighting functional. The eigenvalues $a^*(r, t)$, $a(r, t)$ on which the intensities $I(r, t) = a^*(r, t).a(r, t)$ are then to be replaced by the corresponding creation and annihilation operators $a^\dagger(r, t)$, $a(r, t)$ and the quantum expectation is to be calculated.

$$P_2(r_1, t_1; r_2, t_2)\Delta t_1 \Delta t_2 = A_1 \Delta t_1 . A_2 \Delta t_2 \langle a_1^\dagger(r_1, t_1).a_1(r_1, t_1).a_2^\dagger(r_2, t_2).a_2(r_2, t_2)\rangle \tag{1.3}$$

1.2.2 Photoelectric correlations

It is an immediate consequence of eq. 1.3 for the joint probability that if

$$\langle I(r_1, t_1) I(r_2, t_2)\rangle \neq \langle I(r_1, t_1)\rangle\langle I(r_2, t_2)\rangle, \tag{1.4}$$

then

$$P_2(r_1, t_1; r_2, t_2) \neq P_1(r_1, t_1) P_1(r_2, t_2)$$

where $P_1(r, t)$ is the single probability density for photodetection.

This implies that the two photodetections at r_1, t_1 and r_2, t_2 are not independent but are correlated. Only for special states of the field does the inequality in eq. 1.4 have to be replaced by an equality, and then the joint probability factorizes into a product of the separated probabilities. An example of that is provided by a pure coherent state $|\{\nu\}>$, or by a randomly phased single mode laser.

By introducing the normalized intensity correlation function $\lambda(r_1, t_1, r_2, t_2)$ defined by the formula:

$$\lambda(r_1, t_1, r_2, t_2) = \frac{\langle I(r_1, t_1) I(r_2, t_2)\rangle}{\langle I(r_1, t_1)\rangle\langle I(r_2, t_2)\rangle} - 1, \tag{1.5}$$

we can re express the joint detection probability in the form

$$\begin{aligned} P_2(r_1,t_1;r_2,t_2)\Delta t_1\Delta t_2 &= A_1\langle I(r_1,t_1)\rangle\Delta t_1 A_2\langle I(r_2,t_2)\rangle\Delta t_2\,[1+\lambda(r_1,t_1;r_2,t_2)] \\ &= P_1(r_1,t_1)\Delta t_1 P_1(r_2,t_2)\Delta t_2\,[1+\lambda(r_1,t_1;r_2,t_2)] \end{aligned} \tag{1.6}$$

This shows clearly that the normalized function $\lambda(r_1,t_1,r_2,t_2)$ provides a measurement of the lack of statistical independence of the photoelectric pulses.

1.2.3 Bunching effect: Handbury-Brown and Twiss experiment

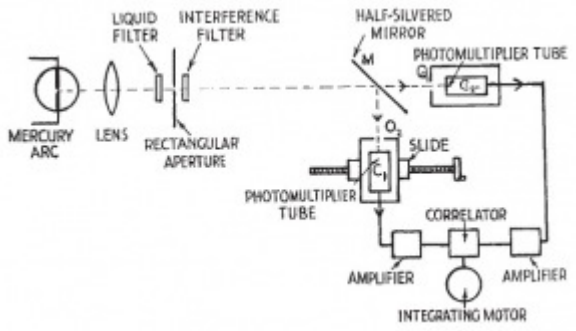

Figure 1.12: Hanbury Brown and Twiss setup as presented in their nature publication (1956)

For states for which photoelectric correlations exist, the photoelectric pulses produced by illuminated photodetectors evidently do not occur strictly at random, and by studying their correlations in space and time, one should be able to obtain information about the nature of the optical field. The first experimental proof of this, and the first evidence for the existence of photoelectric correlations, was provided by the experiments performed in the 1950's by Handbury-Brown and Twiss (1956,1957)[26, 32] with the apparatus shown in fig. 1.12. The light beam from a mercury arc was divided into two by a beam splitter, and the two beams fell on two photomultipliers, one of which could be translated across the field.

As the light is produced by a stationary thermal source, the average intensity doesn't depend on time and the normalized correlation function $\lambda(r_1,t_1,r_2,t_2)$ depends only on the time difference $t_2-t_1=\tau$ and can be denoted $\lambda(r_1,r_2,\tau)$ can be simply related to the normalized second order correlation function:

$$\gamma(r_1,t_1,r_2,t_2) = \frac{\langle a_1^\dagger(r_1,t_1).a_2(r_2,t_2)\rangle}{[\langle I(r_1,t_1)\rangle\langle I(r_2,t_2)\rangle]^{1/2}}$$

For stationary light, $\lambda(r_1,r_2,\tau) =\mid \gamma(r_1,r_2,\tau)\mid^2$

Equation eq. 1.6 becomes

$$P_2(r_1,t_1;r_2,t_2)\Delta t_1\Delta t_2 = A_1\langle I(r_1)\rangle\Delta t_1 A_2\langle I(r_2)\rangle\Delta t_2\left[1+\mid\gamma(r_1,r_2,\tau)\mid^2\right]$$

which shows that photoelectric correlations are expected at r_1 and r_2 so long as the degree of coherence is not zero at these points. This is confirmed by experimental results which showed a bunching of the joint probability decreasing with the separation length between the two detectors. We won't enter into the details of photocurrent correlation theory necessary to

describe a measurement in which the individual photoelectric pulses may not be resolved because of the relatively slow electronics at disposal of the experimentalists. However it showed that the measurement of the quantity $\mid \gamma(r_1, r_2, \tau) \mid^2$ is possible by setting up two photodetectors in an optical field, and materializes the correlated character of the light by a bunching effect on the joint probability versus the delay between two photodetections. This effect is easily transposable on the experiment we will present in chapter 5 of the manuscript where we will probe the correlation of the energy of the emitter.

The autocorrelation experiment used in this thesis is a direct derivative of the HBT experiment. However we will use it in a first step, not to prove the correlation of an optical field, but to prove the anti correlation of a special optical field. This is the anti bunching effect.

1.2.4 Antibunching effect

Correlation of a quantum state of the optical field

In the experiment considered above, photoelectric pulses occurring exhibit bunching, as shown by the fact that the joint detection probability always satisfies the inequality

$$P_2(r, t; r, t + \tau) \leqslant P_2(r, t; r, t)$$

According to eq. 1.5 and eq. 1.6, this implies that

$$\langle I(r, t) I(r, t + \tau) \rangle \leqslant \langle I^2(r, t) \rangle$$

In other words, the two-time intensity autocorrelation function either falls from its initial value at $\tau = 0$ or remains constant. One can show from the Schwarz inequality that this equation must hold generally for a stationary field. It follows that for such states the photoelectric pulses must exhibit either bunching or complete randomness; antibunching, which implies that $P_2(r, t; r, t + \tau) > P_2(r, t; r, t)$ is impossible under these circumstances. Both thermal light and laser light have to be excluded. Observation of photoelectric antibunching therefore provides evidence for an explicitly quantum mechanical state of the optical field, whereas bunching carries no such implication. This is in agreements with the predictions of the quantum theory of resonance fluorescence and it was first observed by Kimble, Dagenais and Mandel in 1977 [27].

As we have seen, the joint probability that a photodetector exposed to the atomic fluorescence registers two photons at time t and $t+\tau$ is proportional to the second order intensity correlation:

$$\Gamma^{(2)}(r, t, t + \tau) = \langle I(r, t) I(r, t + \tau) \rangle. \tag{1.7}$$

It can be demonstrated that, in the case of the atomic fluorescence, the intensity correlation can be expressed such as ([28] Kimble, Mandel 1976):

$$\langle I(r, t) I(r, t + \tau) \rangle = \langle I(r, t) \rangle \langle I(r, \tau) \rangle_G \tag{1.8}$$

The first factor $\langle I(r, t) \rangle$ is proportional to the probability that one photon is emitted at time t, and it becomes constant at steady state. But in the process of emission the atom makes a quantum jump to the ground state, and the second factor $\langle I(r, t) \rangle_G$ is proportional to the probability that another photon is emitted after a subsequent time delay τ , given that the atom is in the ground state at time $\tau = 0$.

A Sub-poissonian source

If the number of photons n emitted by the atom in a short interval T is counted, then the photon statistic must be sub-poissonian. It can be shown that the variance of n is given by

$$\langle(\Delta n)^2\rangle = \langle n\rangle(1 + \langle n\rangle\theta(T)/T),$$

where the function $\theta(T)$ is defined by the integral

$$\theta(T) = \int_{-T}^{T}(1- \mid \tau \mid /T)\lambda(\tau)d\tau.$$

For a sufficiently short time interval T, $\lambda(\tau)$ may be replaced by $\lambda(0)$ under the integral so that

$$\theta(T) \approx \lambda(0)\int_{-T}^{T}(1- \mid \tau \mid /T)d\tau = \lambda(0)T.$$

Hence the variance becomes

$$\langle(\Delta n)^2\rangle = \langle n\rangle(1 + \lambda(0)\langle n\rangle),$$

From equations eq. 1.7 and eq. 1.8, $1 + \lambda(0) = 0$, or

$$\lambda(0) = -1,$$

so that,

$$\langle(\Delta n)^2\rangle = \langle n\rangle(1 - \langle n\rangle),$$

Thus the detected photons are sub-poissonian as $\langle(\Delta n)^2\rangle < \langle n\rangle$, The Q factor characterizing the departure from the Poisson statistic is defined as:

$$Q = \frac{\langle(\Delta n)^2\rangle - \langle n\rangle}{\langle n\rangle}$$

The first experimental confirmation of subpoissonian statistics in resonance fluorescence was demonstrated in 1983 by Short and Mandel [30].

Antibunching measurement

To characterize experimentally the antibunching effect, the photoelectric pulses from the two detectors are fed to the start and stop of a time-to-digital converter, that registers their separation τ . The number of pulse pairs $n(\tau)$ is a direct measure of the joint photodetection probability and therefore of $\Gamma^{(2)}(r; t, t + \tau)$. After renormalization, one obtain the intensity correlation function in the steady state or long time $t \to \infty$:

$$g^{(2)}(\tau) = 1 + \lambda(\tau) = \frac{\langle I(r,t)I(r,t+\tau)\rangle}{\langle I(r,\infty)\rangle^2} \tag{1.9}$$

In fig. 1.13 a) is represented the antibunching setup which permits the measurement of this quantity. As quantum dots are “artificial atoms”, ie a two level system which is emitting photons one by one, one expect the photons emission to obey a sub poissonian statistic. First evidences of antibunching in quantum dots were demonstrated by P. Michler et al. in colloidal quantum dots [33]. We will discuss this in more details in the third chapter of this manuscript, devoted to room temperature antibunching measurement.

From eq. 1.6 and eq. 1.9, one can express the second order correlation function with probabilities:

$$g^{(2)}(\tau) = \frac{p(t+\tau;t)}{p(t)p(t+\tau)} = \frac{p(t+\tau \mid t)}{p(t+\tau)}$$

$p(t)$ is the photodetection probability at any time t , $p(t+\tau \mid t)$ is the probability to detect a photon at time $t+\tau$ knowing that a photon was detected at time t, and as the quantum dot emission is stationary,

$$g^{(2)}(\tau) = \frac{p(\tau \mid 0)}{p(\tau)}$$

One can model this measurement by considering a two-levels system (fig. 1.13 b)), and the level populations n_x, n_0 such as $n_x + n_0 = 1$. The detection of a photon at time 0 means that the system is such as $(n_x(0) = 0, n_0(0) = 1)$. By letting the system evolve from these initial conditions, one can evaluate $g^{(2)}(\tau)$,

$$g^{(2)}(\tau) = \frac{(n_x(\tau) \mid n_x(0) = 0)}{n_x(\infty)}.$$

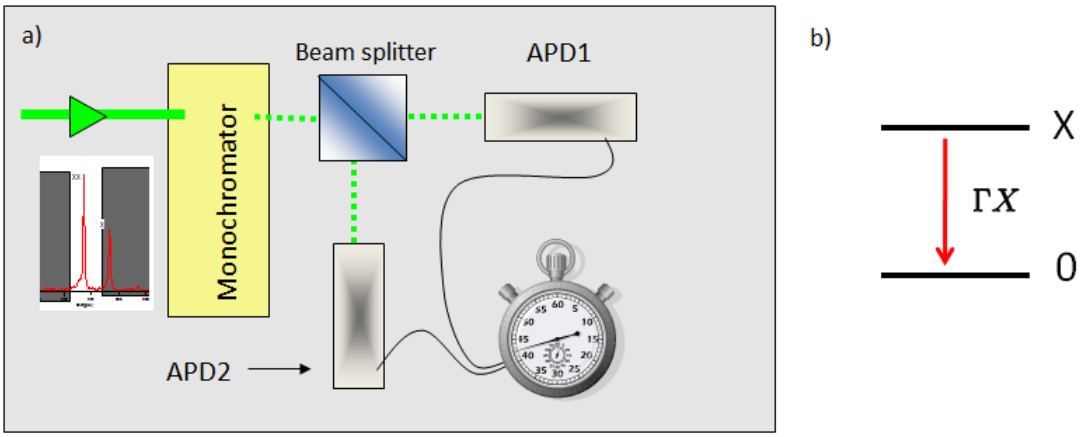

Figure 1.13: a) autocorrelation (antibunching) setup, b) two level system model

Cross-correlation measurement

It is also possible to slightly modify this setup and instead of measuring correlation of photons emitted by the same transition, measuring correlation between different transitions of the quantum dot. This is the cross correlation setup. One can probe the quantum dot dynamic and obtain different interesting informations about nature of the transitions, delays between the transitions, spin-flip or carrier relaxation times. To do so, the setup is put in the configuration represented in fig. 1.14 a). We send photons coming from two transitions on two separated photodetectors. A typical situation where cross correlation experiment can be performed as presented in fig. 1.14 b): for example, a three-level system with the levels linked two by two by a transition $(2 \rightarrow 1, 3 \rightarrow 2)$ rate. The aim of such an experiment is to characterize the link between the two resulting transitions. In this case, if a photon has been emitted by the upper transition, the system is in the initial state $(n_1(0) = 0, n_2(0) = 1, n_3(0) = 0)$ and

$$g^{(2)}(\tau) = \frac{(n_2(\tau) \mid n_2(0) = 1)}{n_2(\infty)}.$$

We'll use this modelization principle mainly in the chapter 4 of this manuscript, where we will probe the dynamic of a charged quantum dot.

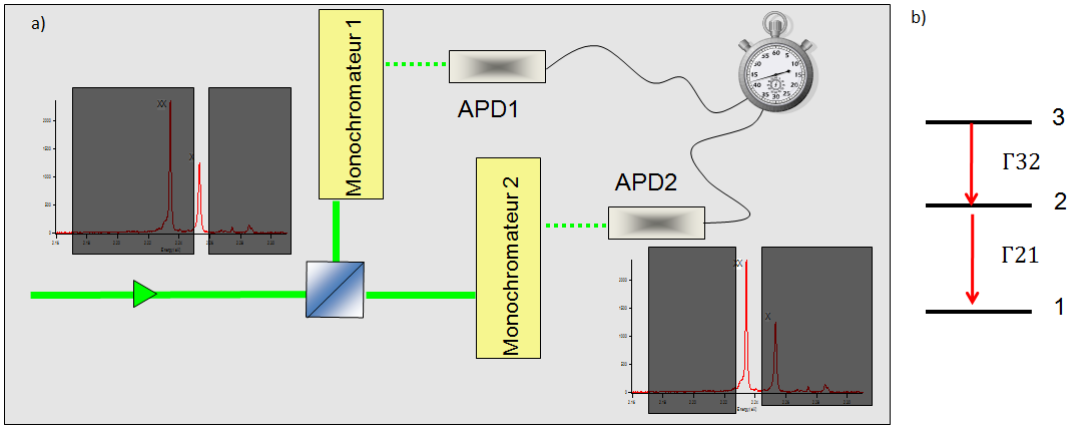

Figure 1.14: a) cross-correlation setup, b) example of model with a 3 levels system

Chapter 2

Neutral nanowire quantum dots dynamic

In this section we investigate the dynamic of a neutral nanowire quantum dot. What is meant by the word "neutral" is the fact that the recombinations of the exciton and of the biexciton are done without the presence of any excedentary carrier. We will summarize here the optical experiments which permitted to identify the emission lines, to describe the exciton and biexciton dynamic and to probe and model how the temperature is influencing it. The understanding of this dynamic, especially the dark exciton influence, is very precious for the application presented in the chapter 3, dealing with the emission of single photons at room temperature.

2.1 Emission lines characterisation

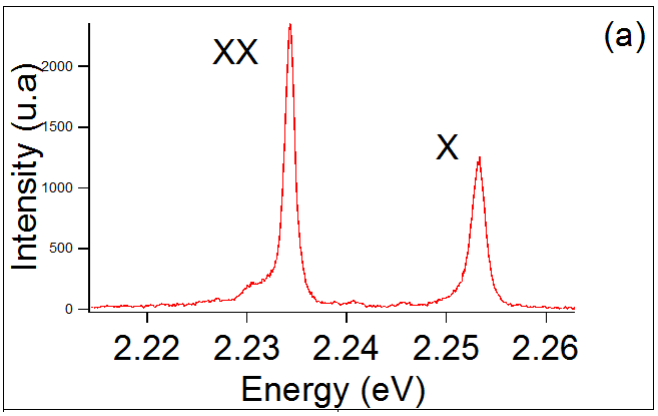

Figure 2.1: Typical spectrum of a neutral quantum dot

In fig. 2.1 is shown a typical spectrum of a nanowire neutral quantum dot emission. The two lines correspond to the exicton and biexciton recombination. They are separated by a 20 meV binding energy. We summarize in this section the different basic experiments allowing us to label these emission lines.

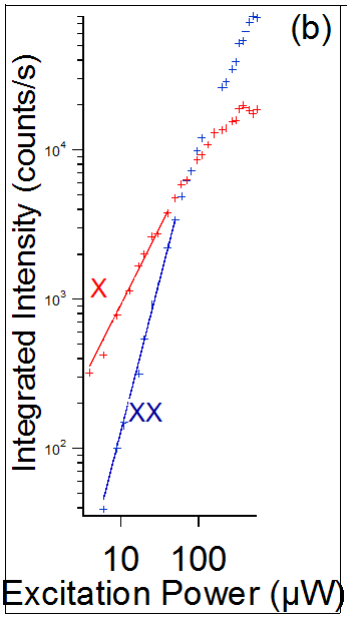

Figure 2.2: Typical power dependence of the integrated lines intensity at 4 K

2.1.1 Power dependence.

In fig. 2.2 is plotted the integrated line intensity versus the excitation power P. This is pulsed excitation at wavelength $\lambda = 420nm$. The two lines don't show the same behaviour. Whereas the exciton line shows linear dependence ($I_x \propto P^{1.05}$), the biexciton one is quadratic ($I_{xx} \propto P^{1.9}$). This is because the biexciton needs the relaxation of 2 excitons in the quantum dot. Thus, at low power the exciton is more luminescent and at high power it is overcome by the biexciton luminescence. The most interesting point of this figure is the saturation values of the 2 lines, which are different. In pulsed excitation, at saturation power (ie the probability to have a biexciton after each pulse equal to 1) and if we model the quantum dot by a 3 level system (exciton, biexciton, empty states), saturation values should be the same, as a biexciton recombination is followed by an exciton recombination. We will discuss this more in details in the section dedicated to the dark exciton influence in this structure.

2.1.2 Lifetime experiment

By decay time experiment, we have access to the probed level population in time. One can describe this population by the rate equation:

$$\frac{dn_x}{dt} = -\frac{1}{\tau_{dx}}.n_x \tag{2.1}$$

τ_{dx} is defined as the decay time of the population n_x, which is from eq. 2.1.
The decay time is decomposed as follows:

$$\frac{1}{\tau_{dx}} = \frac{1}{\tau_{x'}} + \frac{1}{\tau_{nr}}$$

τ_x is the radiative lifetime and τ_{nr} takes into account the loss of excitonic population by non

radiative processes. At 4 K the latters are supposed to be null, then eq. 2.1 becomes:

$$\frac{dn_x}{dt} = -\frac{1}{\tau_{x'}} n_x \tag{2.2}$$

for the biexcton one have the same expression

$$\frac{dn_{xx}}{dt} = -\frac{1}{\tau_{xx}} . n_{xx}$$

At T=4K, the excitonic population decays exponentially with a time $\tau_{x'}$, the radiative lifetime. In fig. 2.3, are plotted the two decay curves of the exciton and the biexciton. It is clear that the exciton is decaying slower than the biexciton ($\tau_{x'} = 400$ ps, $\tau_{xx} = 300$ ps). This can be explained by the fact that the biexciton is composed by two excitons, and thus have a larger probability to decay. In a very simple picture, we would say that we should have $\tau_x = 2\tau_{xx}$. However this picture is wrong if we take into account the Coulomb interaction in the biexciton and it can be shown the ratio between exciton and biexciton lifetime depends on the confinenement [43]. We'll also see that, for the exciton the measured decay time is not the real radiative lifetime. The transition towards dark states must be added, as we will do in the dark exciton section.

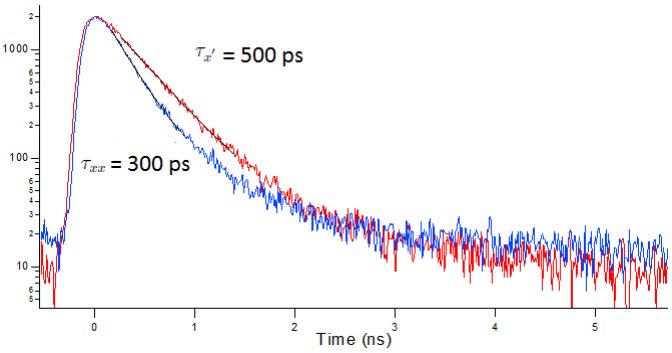

Figure 2.3: Decay of the exciton (blue) and biexciton (red) populations at T=4K.

2.1.3 Cross-correlation measurement:

In the introduction chapter, we discussed about how correlation measurements could help to understand the dynamic of a multi-state emitter. We use here this technique to probe the link between the two transitions appearing on the spectrum. In fig. 2.4, is plotted the result of the cross correlation between the excitonic and biexcitonic lines. The asymetric shape and the bunching appearing for positive delays of the curve is characteristic of a radiative cascade. We first try to explain and model it with a 3 levels system (ground state, exciton, biexciton) in fig. 2.4 c). For the positive delay, the initial condition is that a photon coming from the biexciton recombination was detected at $\tau = 0$, the system is in the exciton state. The bunching is due to the fact that under such initial conditions, the probability to have an exciton in the quantum dot is much larger than the probability to have it at any time and the decrease of this bunching with the delay is due to the decay rate of the exciton. The value of this bunching is interesting: for $\tau = 0$ and if we define $p_x(0,0)$ the probability to have an exciton in the quantum dot at time

0, knowing that a photon from the biexciton was detected : we measured

$$g^2(0) = \frac{p_x(0,0)}{p_x(\infty)} = 4.3.$$

The probability to have a an exciton after a biexciton recombination is 1 ($p_x(0,0) = 1$).Thus, one can deduce $p_x(\infty) = 0.23$, the probability of presence of the exciton in the quantum dot in the steady state. The dashed curve in fig. 2.4 a) is obtained from the 3 levels system (fig. 2.4 c)). It is immediatly obvious that we underestimated here the $g^2(0)$, ie the exciton is generally less present in the quantum dot than predicted by the model. Thus, the exciton decays in an additionnal state, that we introduce in the next section.

Though these three different experiments, we were able to determinate the origin of the lines observed on the spectrum and conclude that we were studying a neutral quantum dot. However, this set of experiments is also indicating the strong influence of the dark exciton, which will be part of our model for the next section.

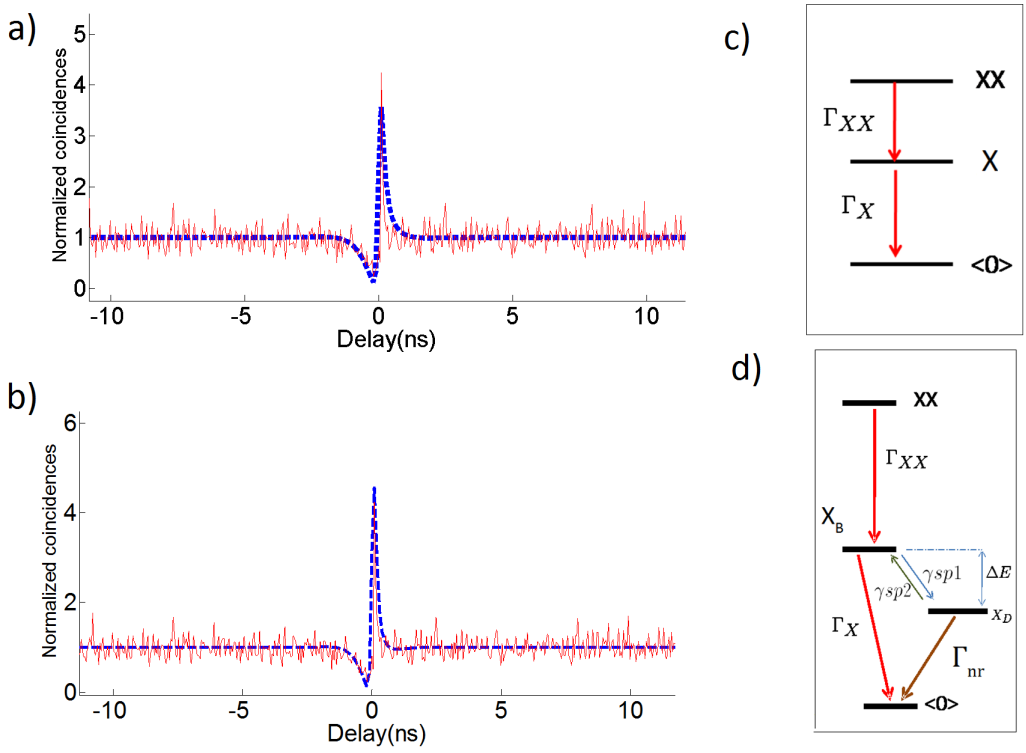

Figure 2.4: a)exciton/biexciton cross correlation figure, (dashed line) simulation obtained from the 3 levels model (c)). (b) exciton/biexciton cross correlation figure, (dashed line) simulation obtained from the 4 levels model (d)) including the dark exciton. For both models, the pump rate was fixed at $r = 3ns^{-1}$

2.2 Influence of the dark exciton

2.2.1 exciton fine structure

In the introduction chapter, we explained that spin-orbit coupling resulted in the presence of light hole of total angular $J_h = 1/2$ and heavy hole $J_h = 3/2$ states in the valence band. The anisotropic strains imposed by the lattice mismatch between the quantum dot material and the nanowire material lifts the degeneracy of these states at the Γ point through the so called Bir Pikkus hamiltonian contribution. Thus, we only consider the heavy hole states to understand optical properties of the exciton. Conduction band being formed by a S orbital, Electrons have a total angular momentum $J_e = 1/2$. The exciton states are split into higher energy states of total angular momentum projection $J_z = \pm 1$, and lower energy states of total angular momentum projection $J_z = \pm 2$. They are separated by the exchange interaction energy ΔE, as the transition between the 2 energy levels is a spin flip of the hole or the electron. We represented these states and the possible transitions between them in fig. 2.4 d).

The high energy states ($J_z = \pm 1$) are radiative, as momentum conservation allows the exciton recombination by a photon emission. On the contrary, the low energy states ($J_z = \pm 2$) are non radiative. This will have an important effect on the photon emission of the studied object.

2.2.2 Interaction energy measurement

Spin flip rates

We pointed out in the previous chapter that power dependence and lifetime experiments were showing strong signatures of dark exciton influence. We will use this in order to measure spin flip rates between the dark and the bright exciton.

Under pulsed excitation, and when the biexciton is saturated, after biexciton radiative recombination, a bright exciton is present in the quantum dot. As shown in fig. 2.4 d), this exciton can recombine radiatively or have one of its carrier spin flip and transit through the dark exciton. The latter is then stored and exciton doesn't produce any photon. We have the evidence of such a mechanism in fig. 2.2. At 4K, exciton and biexciton power dependences don't show the same saturation values, wich means that a photon coming from the biexciton recombination is not always followed by an excitonic photon. If we consider the four-levels model presented in fig. 2.4 d), and set the initial conditions of biexciton saturation ($n_{xx}(0) = 1$, $n_{xb}(0) = n_{xd}(0) = n_{\langle 0 \rangle}(0) = 0.$), and considering that , at 4K, the dark to bright spin flip rate $\gamma_{sp2} = 0$, one can easily solve the associated rate equation and find that the exciton/biexciton ratio at saturation is:

$$r_{x/xx(sat)} = \frac{\Gamma_x}{\Gamma_x + \gamma_{sp1}}. \tag{2.3}$$

This rate can vary a lot, depending on the spin flip rate towards the dark state, thus, depending on the importance of the depopulation of the bright exciton state. We'll see that the range of measured bright to dark spin flip is very important, and led, for the fastest spin flips to ratios such as $r_{x/xx(sat)} \sim \frac{1}{5}$ .From the lifetime experiment we extract the exciton decay time τ_{dx} (see eq. 2.2). This decay time takes into account all the possible decay channels of the excitonic population. In the model we consider, the exciton can recombine radiatively with a radiative lifetime τ_x or spin flip towards the dark state with a spin flip time τ_{sp1}:

$$\frac{1}{\tau_{dx}} = \frac{1}{\tau_x} + \frac{1}{\tau_{sp1}} = \Gamma_x + \gamma_{sp1} \tag{2.4}$$

From eq. 2.3 and eq. 2.4, one can determinate separately Γ_x and γ_{sp1}. For the quantum dot where the presented decay time curves are extracted in the previous section we found $\tau_x = 550$ ps and $\tau_{sp1} = 1.2$ ns. The measurement of the exciton decay time is performed at very low power, so that the population of the biexciton can be neglected.

Interaction energy determination

In the section above, we fixed the exciton radiative lifetime τ_x and the bright to dark spin flip time τ_{sp1} at 4K. We now increase the temperature and measure again the decay curve of the exciton.

Spin flip of the carriers are assisted by acoustic phonons. The speed of this mechanism will depend on how efficiently the carrier couples to these phonons (we will see that in section 2.3), and also on the avaible phonon population. Thus, spin flip transition rates depend on the phonon population that follows a Bose-Einstein distribution $N_B(T, \Delta E) = \frac{1}{1-exp(\Delta E/(k_B T))}$. The spin flip rates γ_{sp1} (bright to dark) and γ_{sp2} (dark to bright) can be written as:

$$\gamma_{sp1} = \Gamma_0(N_B(T, \Delta E) + 1)$$
$$\gamma_{sp2} = \Gamma_0 N_B(T, \Delta E) \tag{2.5}$$

Γ_o is the spin flip rate at 0K. This quantity was determined in the previous section, as $\Gamma_0 \approx \gamma_{sp1}(4K)$.

By increasing the temperature, one increase the phonon population, and make the spin flip rates increase. These enhancements can be followed through temperature dependant decay time measurements. In fig. 2.5 is presented the evolution of the decay time curve for different temperatures from 4K to 80 K. It is mono-exponential at 4 K and becomes multiexponential as the temperature increases with the apparition of a slow component which corresponds to the non radiative recombination time of the dark exciton. The spin flip transition γ_{sp2} (dark to bright) is activated and we observe a phenomenon of repopulation of the bright level from the dark state. This is why the curve becomes biexponential. The importance of this repopulation increases with temperature and the weight of the slow component is enhanced until the dark and bright states are thermalized. Eventually, the slow component dominates the measurement and the decay time curve becomes mono-exponential again.

The parameters involved in the fit of these curves are the following: Γ_x, γ_{sp1},γ_{sp2},Γ_{nr}. The radiative recombination rate is considered as constant with temperature and is calculated from the first decay time measurement at 4K. It is possible to extract the three other temperature dependent rates, as they act differently on the shape of the decay time curve. Indeed, γ_{sp1} is related to the fast component, Γ_{nr} to the slow component occuring with temperature, γ_{sp2} acts on the weight of the slow component as it determinates the importance of the repopulation of the bright state from the long lived dark state.

In fig. 2.2.2 are reported the measured spin flip rates as a function of the temperature for a typical quantum dot. We fit them with eq. 2.5, with Γ_0 fixed from the 4 K measurement, the interaction energy ΔE is tuned in order to fit the experimental datas.

Statistics on several quantum dots

The process described above was reproduced on nine different quantum dots. As shown in fig. 2.2.2, measured splittings range from 4.2 meV to 9.2 meV. A clear trend is appearing: splittings

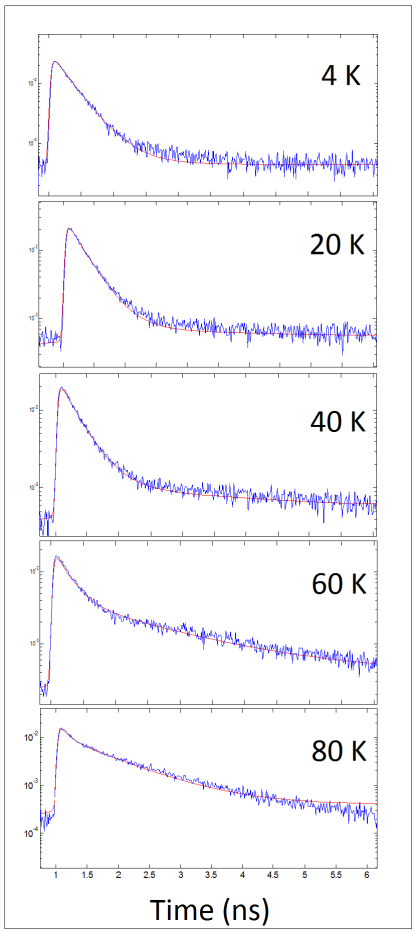

Figure 2.5: Temperature dependent decay time curves from 4K to 80K

measured for low energy emission QDs are generally smaller compared to splittings measured for high energy emission QDs. The latters correspond to small size QDs, where electron and hole wave functions overlap very well, so that their exchange energy is large, leading to large ΔE. Such relationships between QD sizes and energy splittings have been calculated for colloidal QDs[36, 44] . Change in composition of the CdxZn1-xSe QD can also act the emission energy and the value of ΔE. Our measurements do not follow exactly a smooth law. The shape of the confinement has also a strong influence on the wave function forms, and consequently on their correlation function. For example the prolate or oblate nature of the QD geometry appears to have an important effect[36]. This explains why we obtained a cloud of experimental points following a general trend instead of a strict dependence.

2.2.3 Exciton-phonon coupling efficiency

Bright to dark spin flip rate

As explained in section 2.2, at 4 K one have access to the bright to dark spin flip rate $\Gamma_{sp1} \approx \Gamma_0$. In fig. 2.8 are plotted the measured Γ_0 for the nine different quantum dots versus the dark bright energy splitting ΔE. It can be first noted that the measured rates are comparable and even larger than the excitonic radiative rate. This is why the bright exciton is so depopulated

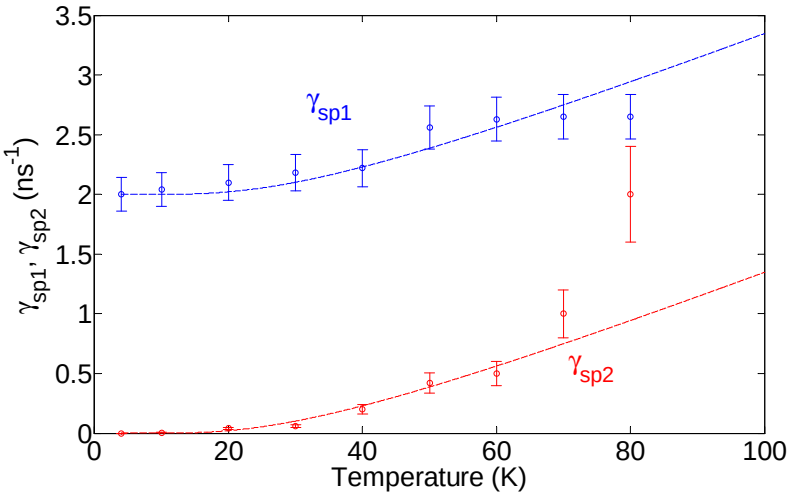

Figure 2.6: Spin flip rates versus temperature. dashed line is obtained from acoustic phonon model. The exchange interaction extracted from the fit is $\Delta E = 7.2$ meV.

compared to the biexciton in all the QDs investigated. The results displayed in fig. 2.8 also show an enhancement of the transition rate with ΔE. This indicates that large ΔE splittings lead to extremely fast depopulation of the bright state.

This rate quantifies the speed of the spontaneous emission of phonons resulting from such a downward transition. Thus, it depends on the efficency of the coupling between one of the exciton carrier and acoustic phonons.

$$\Gamma_0 \propto R(\Delta E)$$

$R(\Delta E)$ is the phonon spectral density in the quantum dot and quantifies the efficency of the exciton-phonon coupling. It depends on the exciton wave function and on the quantum dot geometry and dimensions[34, 35]. We calculate it in the next section and propose a quantitative explanation for the increase observed in fig. 2.8.

Phonon spectral density

We shall only consider longitudinal acoustical (LA) compression modes since longitudinal optical (LO) phonons have energies of about 30 meV far above the dark - bright exciton splitting ΔE. In the following we will perform this calculation both in the 3D and in the 1D case for the available phonon modes. The NW geometry is obviously somewhere in-between these two extreme cases that will only give us a qualitative behavior. We first consider the 3D situation. The phonons dispersion is bulk-like, approximated by the Debye law $\omega(k) = c_l k$, with c_l the sound speed for LA phonons in the semiconductor material. Piezoelectric interactions and longitudinal optical (LO) phonon couplings are neglected. The exciton-phonon interaction is dominated by the hole-phonon interaction [37]. We therefore consider only the latter, whose Hamiltonian can be written, in the second quantization representation with respect to the carrier states, as:

$$H_h = \frac{1}{\sqrt{N}} \sum_{knn'} a_n^\dagger a'_n f_{h,nn'}(k)(b_k + b_{-k})$$

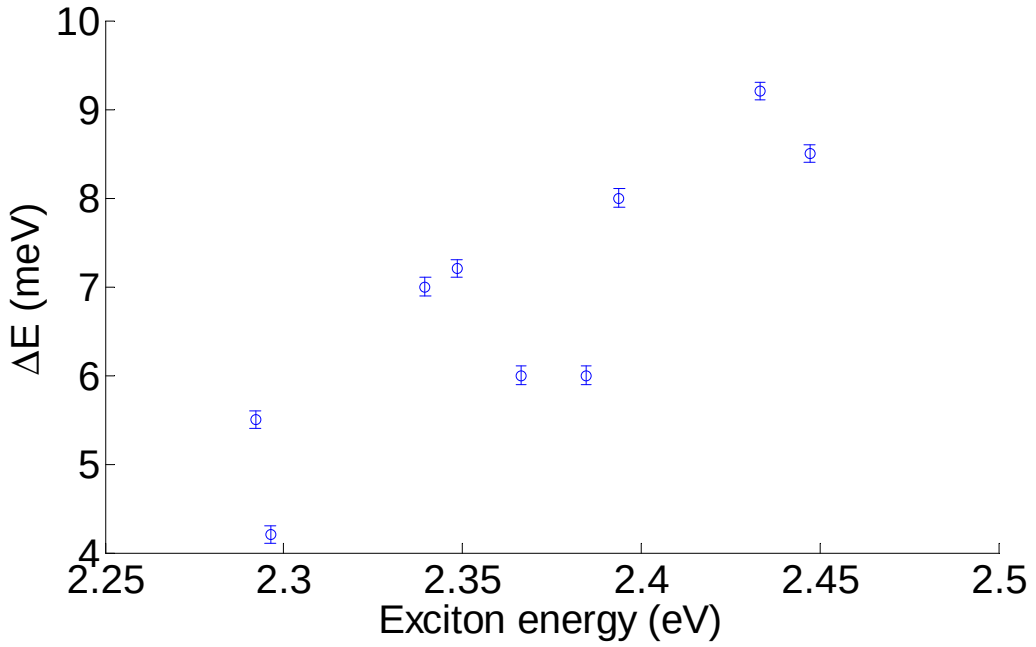

Figure 2.7: Increase of exchange interaction energies ΔE between DS and BS measured on nine QDs as a function of their excitonic emission energy.

where $a_n^\dagger$ and a_n are the hole creation and annihilation operators, $b_k^\dagger$ and b_k are LA phonon creation and annihilation operators. The index n represents the excitation level of the hole, and k the phonon mode.

The coupling constant is defined as:

$$f_{h,nn'}(k) = \sigma_h \sqrt{\frac{\hbar k}{2\rho V c_l}} F_{nn'}(k),$$

where σ_h is the deformation potential for holes, V is the unit cell volume, ρ is the CdSe volumic mass. The quantity $F_{nn'}(k)$ is a purely geometrical form factor given by[38]

$$F_{nn'}(k) = \int_{-\infty}^{\infty} d^3 r \psi_n^*(r) e^{ikr} \psi_{n'}(r).$$

In order to evaluate the coupling constant for the lowest hole state $f_{11}(E)$ we consider the harmonic oscillator potential ground state as the wave function of the hole:

$$\psi(r) = \frac{1}{\pi^{3/4} l_\perp \sqrt{l_z}} \exp\left[-\tfrac{1}{2}\left(\tfrac{r_\perp}{l_\perp}\right)^2 - \tfrac{1}{2}\left(\tfrac{z}{l_z}\right)^2\right],$$

where $r_\perp$ is the position component in the xy plane and $l_\perp, l_z$ are respectively the in plane, and out of plane (z direction) localization widths. For this wave function the form factor is easily found as

$$F_{11}(k) = \exp\left[-\left(\frac{k_\perp l_\perp}{2}\right)^2 - \left(\frac{k_z l_z}{2}\right)^2\right].$$

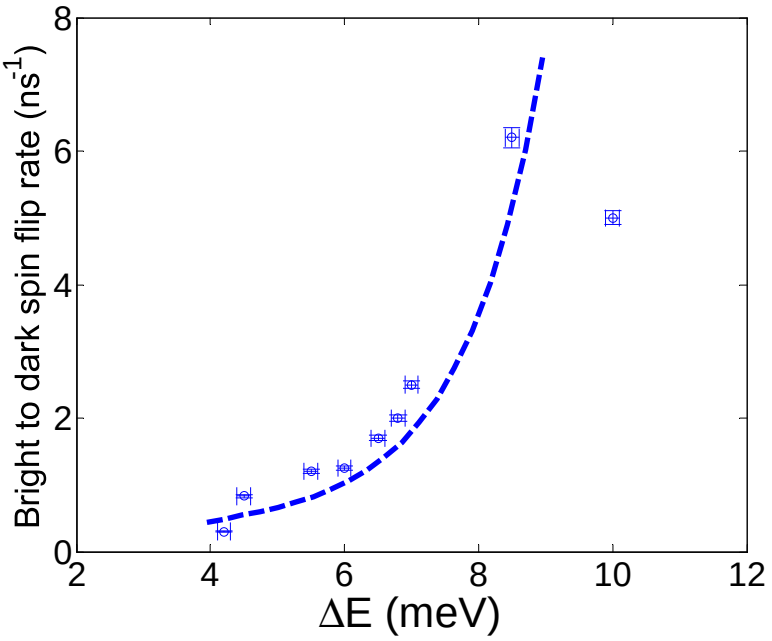

Figure 2.8: Transition rate from BS to DS Γ_{sp1} at 4K plotted as a function of splitting energy ΔE between DS and BS for nine dierents QDs. The dashed line is a guide for the eyes

For the lowest hole state, the phonon spectral density in the QD is:

$$R(E) = \frac{1}{\hbar^2}(N_B(E)+1) \times \frac{1}{N}\sum_k f_{11}(k) f_{11}^*(k)[\delta(E-E(k)) + \delta(E+E(k))].$$

After performing the summation over k in the continuum limit, introducing the quadratic density of state of the phonons corresponding to the 3D case, the phonon spectral density is :

$$R(E) = R_o E^3 g(E),$$

with

$$R_o = \frac{(\sigma_h)^2}{8\pi^2\hbar\rho c_l^5}.$$

The quantity R_o contains all material parameters. The cubic dependence is due to the quadratic phonon density of state in a 3D geometry, and the function g(E) is a function of the energy and of the geometrical parameters of the QD[39]

$$g(E) = \int_{-\frac{\pi}{2}}^{\frac{\pi}{2}} \zeta \cos\zeta \exp\left[-\frac{(l_\perp)^2 E^2}{2\hbar^2 c_l^2} \times \left(cos^2\zeta + \frac{l_z^2}{(l_\perp)^2} sin^2\zeta\right)\right] d\zeta,$$

where ζ is the angle of the wave vector k with respect to the normal to the z direction.

Describing coupling of the hole to phonons confined in a nanowire the same way as in a 3D semi conductor bulk matrix seems a rough approximation. So we also considered the 1D case in which the nanowire is taken as an infinitely thin monomode phonon wave guide. The phonon density of state is constant and we consider that only the phonons propagating along the nanowire

(z direction) can couple to the hole whose wavefunction is taken as $\psi_h(r) \propto \exp[-(1/2)(z/l_z)^2]$. The spectral density becomes:

$$R_{1D}(E) \propto E g_{1D}(E),$$

with

$$g_{1D}(E) = \exp\left[-\frac{l_z^2 E^2}{2\hbar^2 c_l^2}\right].$$

The phonon spectral density is linear with energy but the geometrical factor $g_{1D}(E)$ has the same gaussian energy dependence as $g(E)$.

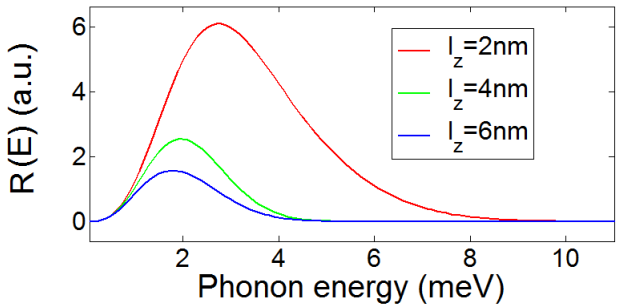

Figure 2.9: 3D Phonon spectral density for 3 different QD sizes along the z direction (red curve: l_z =2 nm, green curve: l_z=4 nm, blue curve: l_z=6 nm). Smaller QD z dimension shifts the maximum of the coupling constant toward the higher energies, and enhances its relative value.

Effects of the quantum dot size

After calculating the spectral density of the phonons in a quantum dot, we are now interested on how the size of the quantum dot is influencing it and affects the transition rate Γ_0.

Three calculated 3D phonon spectral densities corresponding to three different l_z values ($l_z = 2, 4, 6$ nm) are plotted in fig. 2.9. Because of its increase with energy (linear for 1D, cubic for 3D), $R(\Delta E)$corresponding to QDs with smaller l_z have their maximum enhanced and shifted toward the higher energies. As a consequence, in small QDs, high energy phonons couple more efficiently with the hole.

On the other hand by reducing the quantum dot size, one enhance the exchange interaction, and therefore the bright dark splitting shown in fig. 2.7. This increase can be evaluated by the calculus of the short range hole-electron exchange energy:

$$\Delta E = \Delta E^{3d} \frac{1}{|\varphi^{3d}(0)|^2} \int |\psi_e(r)|^2 |\psi_h(r)|^2 d^3r,$$

where $\psi_{e/h}(r)$ are the electron/hole wave functions, ΔE^{3d} is the exchange energy in the bulk material ZnCdSe [40] ($\Delta E^{3d} = 0.19$ meV, for a $Cd_{0.5}Zn_{0.5}Se$ composition of the QD as measured in high resolution TEM experiments [42]), and $|\varphi^{3d}(0)|^2 = 1/\pi a_B^{*3}$ with a_B^* the Bohr radius of the free exciton. To match the measured values of ΔE (from 4 meV to 9 meV), we set the lateral confinement parameter $l_\perp$ at 4nm. When l_z decreases ΔE increases. And as, for the energy

range we are interested in, the phonon spectral density $R(E)$ is decreasing with E, this would indicate that the coupling is less efficent for large ΔE.

As a conclusion, the size reduction has two opposite effects: It shifts towards high energies and enhances the phonon spectral density, which is favorable to a better coupling of the hole to the phonons, and at the same time it increases the energy of the transition ΔE, which is making this coupling less efficient.

Simulation of the spin flip rate increase.

In order to determinate which of the two opposite effects of the size reduction is dominating in our structure, we calculate the phonon spectral density $R(\Delta E)$ for QD with different bright dark splittings ΔE owing to their different sizes. This way we can conclude on how is evolving the hole-phonon coupling efficiency and obtain conclusions on how the spin flip rate should depend on the exchange interaction. This process is summarized on a simple sketch in fig. 2.10 a) for a small quantum dot (large ΔE) and a big quantum dot (small ΔE). The idea is to compare the variation of R(ΔE) resulting from a size reduction δl_z. If $R(\Delta E)$ is increased, we can conclude that the exciton-phonon coupling is more efficient for larger exchange interactions, as we experimentally find.

The results, for the 3D and 1D cases described above, are plotted in figure fig. 2.10 (b) and (c). Because of the simplicity of the considered exciton wave function, the aim of the calculation is neither to fit the experimental data nor to obtain a quantitative estimation of the transition rates. However, we can show that the hole-phonon coupling efficiency is increasing with ΔE in both cases, which is not a trivial result as the cut-off imposed by the dimensions of the QD makes this efficiency vanish for higher energy phonons. The effect of the confinement dimensions on the phonon spectral density can be a good explanation for the trend measured by the experiment in fig. 2.2.3. The two situations considered here are extreme cases and we can expect a real nanowire geometry to impose an intermediate behavior for the hole phonon coupling.

2.2.4 Consequence on the exciton luminescence

This increase of the exciton-phonon coupling efficiency with energy splitting has some consequences on the temperature dependent exciton-biexciton saturation ratio under pulsed excitation. This calculated ratio is represented in fig. 2.11 as a function of temperature and energy splitting ΔE. We used the level scheme presented in fig. 2.4 d) and the values of the transition rates given in section 1. The relation between $\gamma_{sp1}(4K)$ and ΔE is taken from the function used as a guide for the eyes in fig. 2.8. We also considered the increase of the dark exciton non radiative recombination $\Gamma_{nr}(T)$ with temperature following an Arrhenius law $\Gamma_{nr}(T) \sim exp(-E_a/k_BT)$, with an activation energy E_a. For the two QDs studied in fig. 2.12 we have measured $E_a = 30 \pm 5$ meV and we have taken $E_a = 30$ meV in the model used in figures fig. 2.11 and fig. 2.12. The particularity here is that the DS lifetime at $T = 4K$ ($1/\Gamma_{nr} = 5$ ns) is rather short compared to values reported in other systems (up to $1\mu s$ [41]) and is of the same order of magnitude as the exciton radiative lifetime when temperature is raised up to only several tens of K. A characteristic temperature behavior is shown in fig. 2.11. The exciton intensity is very small at low temperature (particularly in the high splitting region), increases as temperature is increased up to $T = 50$ K, and finally decreases with higher temperatures. The effect of repopulation of the bright exciton due to the DS to BS spin flip is compensated and overwhelmed by the exciton population loss caused by the faster dark exciton non radiative recombination.

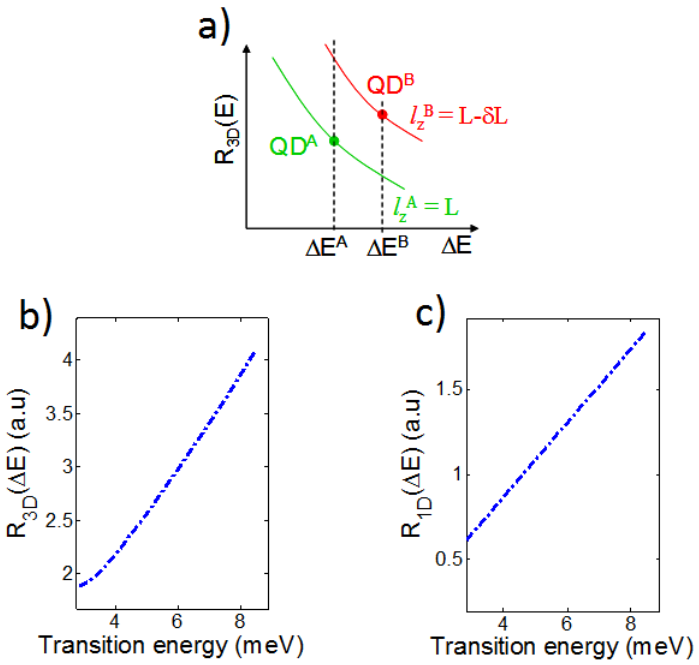

Figure 2.10: a) Zoom of the high energy side R(ΔE) curve, for two quantum dots QDA and QDB with size $l_z^A > l_z^B$ which leads to bright-dark splittings $\Delta E^A < \Delta E^B$. When going from a big dot (QD A) to a small dot (QD B), the size effect alone leads to a increase of R_{3D}, but the reduction of size comes with a increase of the bright-dark splitting which reduces the final value of R_{3D}. (b) Calculated 3D hole-phonon coupling efficiency vs transition energy ΔE. (c) Calculated 1D hole-phonon coupling efficiency vs transition energy

One can also observe that, at high temperature, the exciton emission intensity is still significantly weaker than the biexciton. This last conclusion is very important and will lead us to one of the arguments used in the next chapter dealing with the obtention of antibunching at room temperature.

As shown in fig. 2.12, representing the exciton-biexciton ratio versus temperature for 2 different QDs with different measured ΔE (4.5 meV and 8.5 meV), this exciton line intensity decrease is more sensitive for large ΔE. However, at 300K, the bright exciton is still less luminescent for large splittings. The overall conclusion is very important and will lead us to one of the arguments used in the next chapter dealing with the obtention of antibunching at room temperature. Indeed, as we will discuss later, the phonon broadening of the lines occuring at room temperature produces an overlap of the exciton and biexciton lines. Thus, at high temperature, one can not discriminate the lines spectrally and measurement of the autocorrelation of one line is inevitably degraded by contamination of the other line. We'll also see that this contamination has strong effect because exciton and biexciton are sending photons by bunches, which leads to a high probability to measure coincidences at the zero delay (see chapter 1, section 3 and chapter 3, section 1). We will take great advantages on the fact that one of the line intensity is weaker than the other, even at room temperature.

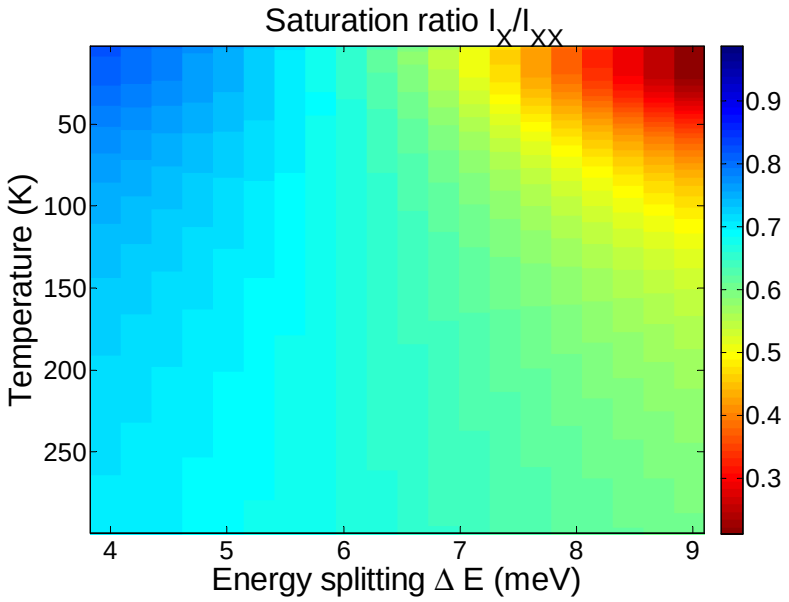

Figure 2.11: Calculated Exciton/biexciton intensity ratio as a function of the exchange interaction ΔE and the temperature

2.3 Conclusion

In this chapter, after identifying unambiguously the nature of transitions observed on the spectrum, we investigated the dynamic of the neutral quantum dot, discussing the balance of the transitions between the exciton states (dark and bright) and the biexciton. This led us to a better understanding on how the quantum dot size was influencing the exciton-phonon coupling, how the transition from the bright states to the dark states was affected and to explain the temperature behaviour of this system. The conclusions we made will help us to explain the possibility to use neutral quantum dots as efficient single photon source at room temperature.

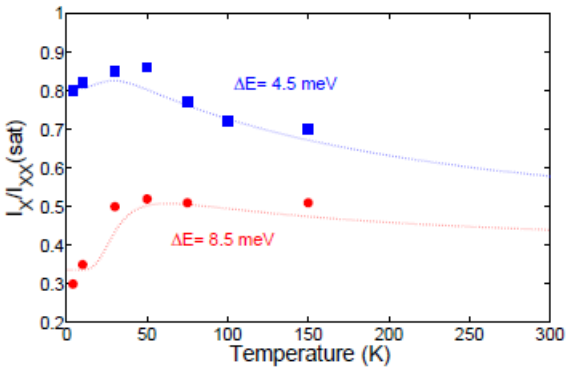

Figure 2.12: Exciton/biexciton intensity ratio as a function of the temperature for two different ΔE . Squares and dots are experimental values for 2 different quantum dots.

Chapter 3

Single photon emission at room temperature

For some applications using the ability of an emitter to send single photons, such as quantum cryptography [47], it is desirable to operate at room temperature. Amongst the numerous different emitters developped in the last 10 years, the vast majority are unable to fullfill this requirement. In this chapter, after defining the state of the art, we will demonstrate that the emitter we are studying in this thesis proved to be still operational at room temperature. In particular, we'll describe its advantages, quantify the degradation of the single photon signal quality with temperature, and study its resistance against temperature. The source of single photons is the biexciton recombination. This original choice is justified by the conclusions of the work exposed in chapter two. Specificities of the optical properties of nanowire quantum dot led us to the first demonstration of antibunching at room temperature from an epitaxied quantum dot.

3.1 State of the art

In this section we summarize briefly the different existing single photon sources, underlining their maximum operating temperature resistance. In fig. 3.1 is provided a list of the different reported single photon sources.

Two structures, NV centers and nanocrystals, are already routinely providing single photons at room temperature. For nanocrystals, the very common blinking phenomen is degrading their ability to emit single photons on demand. However some solutions were proposed to reduce and eventually anihilate such inconveniants during the last few years [55, 56]. The demonstration of single photon emission performed at room temperature in this thesis is the first reported on epitaxied quantum dots. AlN/GaN quantum dots [52], CdSe/ZnSe self assembled quantum dots [53], and the first generation of Cdse/ZnSe nanowire quantum dots [54] already exhibited single photon emission at high temperature ($\approx$200K).

The second point we emphasize is the radiative lifetime of the emitters displayed in fig. 3.1. This time is limiting the single photon emission rate. We measured for the biexciton (chapter 2, section 1) a radiative lifetime of 300 ps. This means that the emission rate (2.5 Ghz) potentially reacheable is an order of magnitude larger than for all the other emitters.

	Blinking	Bleaching	Temperature	Emitter lifetime
Atoms (Kimble, 1977)	No	No	mK	16.5 ns
Ions (Dietrich, 1987)	No	No	mK	3.5 ns
Dye molecules (Lounis 2000)	No	Yes	300K	3.8 ns
NV centers (Kurtsiefer 2000, Beveratos 2000)	No	No	300K	11.6 ns
Carbon nanotubes (Högele 2008)	No	No	50K	0.25 ns
Nanocrystals (Wang 2009)	No	No	300K	4.1 ns
Quantum dots (Bounouar 2011)	No	No	300K	0.3 ns

Figure 3.1: Summary of principle existing single photon sources

3.2 Antibunching measurement.

3.2.1 Pulsed and continuous excitation

We have two options concerning the excitation mode of the quantum dot during the antibunching measurement. Between these two options, the one which is allowing us to obtain the best signal to noise ratio for an integration time as short as possible is the best. In fig 3.2 are presented typical autocorrelation histograms for continuous and pulsed excitation obtained at 4 K. In fig 3.2 a), the antibunching in continuous excitation is represented by the characteristic dip around the zero delay. The correlation time of this symetrical dip is such as:

$$\frac{1}{\tau_d} = \gamma_{rad} + \gamma_{pump}$$

γ_{rad} is the radiative rate and γ_{pump} is the pump rate. Thus, the correlation time of the antibunching is at best the radiative lifetime. It is reduced when the pump power is increased. The conditions to observe the antibunching is to use a set up with a time resolution inferior to the radiative lifetime of the emitter (here 300 ps), and to set the counting channels time at least 10 times smaller ($\tau_c = 30$ ps). Let's note that the fast APD's with the required time resolution have a quantum efficiency (25%), twice smaller than slow APD which could be used under pulsed excitation. The advantage is that at saturation, the biexciton emits one photon per lifetime whereas in pulsed excitation, the emission rate is limited by the excitation rate ($\gamma_R = \frac{1}{T_R}$) of the pulsed laser (here 13 ns). The intensity gain (compared to pulsed mode) is $\frac{\gamma_{rad}}{\Gamma_R} \approx 40$.

In the situation where the single photon source intensity at saturation under continuous excitation is 4.10^5 photons per second. 2.10^5 photons per second hit each APD, and the detection counting rate for each APD is

$$N_1 = N_2 = 2.10^5.\frac{25}{100} = 5.10^4\, counts.s^{-1}$$

We considere to have an acceptable signal to noise ratio when we have N_c =25 counts per channel. The statistical noise is $\sqrt{25} = 5$ counts, and the signal to noise is $\frac{1}{5}$. Let us calculate

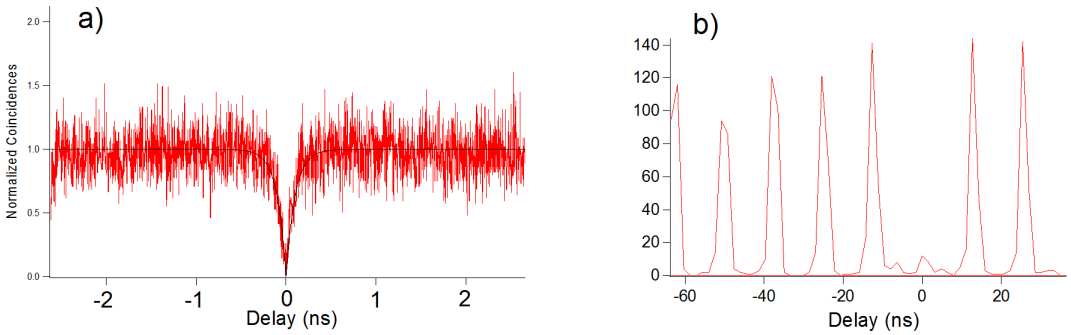

Figure 3.2: Typical biexciton autocorrelation histograms. a) under continuous excitation, b) under pulsed excitation

the integratio time T needed to obtain this signal to noise ratio under continuous excitation. The number of coincidence per counting channel should be, for a poissonnian source:

$$N_c = N_1.N_2.\tau_c.T,$$

Thus the corresponding integration time is.

$$T = \frac{N_c}{N_1.N_2.\tau_c} = 320\,s$$

In fig 3.2 b) is represented a typical biexciton autocorrelation histogram at 4 K. Each peak is separated by 13 ns and represents the coincidences recorded after successive excitation pulses. The zero delay pulse correspond to coincidences occured after the first excitation pulse. The antibunching signature is the abscence of zero delay peak in the histogram.

For the pulsed mode, we only need to set the counting channel time equal to the excitation repetition time T_R. The saturation intensity of the emitter has to be divided by 40, as it is only excited every 13 ns. And we take into account that slow APD with cumulated time resolution of 700 ps are appropriate, and that they have a quantum efficiency of 50%. The photons detected per second are $N_1 = N_2 = 2.5.10^3 counts.s^{-1}$

Therefore, the integration time becomes, in this case:

$$T = \frac{N_c}{N_1.N_2.\tau_c} = 300\,s$$

For the two situations, the integration time is similar. This is due to the very short radiative lifetime of the emitter, ie the large loss of intensity under pulsed excitation, which compensates the advantage given by the large counting channel time. However this configuration has other interests.

Depending on the quality of the single photon emission, this zero delay peak attenuation can be relative. And it's much easier to estimate the quality of the single photon emission by measuring the area of the central peak compared to the others. This is especially true at high temperature, where the degradation of the antibunching is very important, and for high excitation powers, where the correlation time of the antibunching under continuous excitation is very short. The last reason is more technical. When we performed this study, the only continuous laser at our disposal was a 405 nm diode. The pulsed laser permitted us to excite the quantum

dot below the ZnSe barrier, which revealed to be a cleaner and more efficient excitation. It also created less damages on the nanowire after long exposition, especially at high temperatures.

In the following, the presented antibunching measurements - and pulsed cross correlation measurements - were obtain with a 475 nm pulsed excitation.

3.2.2 Measurement

One can show that autocorrelation measurements on a signal composed by N emitters exhibit a $g^2(0) = 1 - \frac{1}{N}$ [58]. Thus, zero delay autocorrelation of a true single photon source should be below 0.5. In fig. 3.3 b), is shown the autocorrelation of the biexciton at 4K, exhibiting a very good antibunching. In fig. 3.3f) is shown the autocorrelation of the same line at 300K. The antibunching was degraded, but it is still demonstrating that the emitter is a single photon emitter. ($g^2(0)$ =0.48 from raw datas)

Similar result was obtained on an other quantum dot at 290K with a non corrected $g^2(0) = 0.42$. A few other quantum dots exhibited antibunching at 250 K and many at 200K. The main experimental problem for such high temperature measurements was the destruction or deterioration of the quantum dots with the joint temperature and optical excitation.

The degradation of the antibunching was progressive as temperature was increased (see fig. 3.4). We believe that one part of this degradation is due to the exciton parasitic emission caused by lines enlargement (around 18 meV at 300K), we'll see in the last chapter of this manuscript that this enlargement is only due to phonon braodening and not spectral diffusion. But the mixing between exciton and biexciton is not the only reason. In the next sections we explain how we extract the antibunching at zero delay value, how we remove noise background from the raw datas, and we discuss the possible causes of measurement degradation occuring with temperature.

3.2.3 Evaluation of $g^{(2)}(0)$

The $g^2(0)$ value is the area of the zero delay peak divided by the area of one of the other peaks. In order to avoid possible errors on this evaluation due to statistical fluctuations and any bunching effect (not present in our system) of the non zero peaks intensity, we normalize the autocorrelation figure more rigorously. The coincidences occuring at non zero delays are uncorrelated. (all the characteristic times of the quantum dot are much smaller than the repetition time of the excitation of 13 ns). Thus they are governed by a poissonnian statistic. It is possible to calculate the theoretical number of coincidences we should obtain for each peak if we know the count rate for each APD and the integration time:

$$N_c = N_1.N_2.T.T_R.$$

N_1 and N_2 are the count rates on APD 1 and APD 2, T the total integration time and T_R is the repetition time of the laser. At 300K, the number of counts rate per APD was approximately 4000 s^{-1}. We divide the peaks area by the calculated quantity N_c. In fig. 3.3f) the numbers indicted above each peak are deduced from this renormalisation. At 300K, the number of counts rate per APD was approximately 4000 s^{-1}. For the non zero delay peaks, fluctuation of these numbers around 1 is due to poissonian statistical fluctuation. The value of $g^2(0) = 0.48$ is also obtained from the renormalisation.

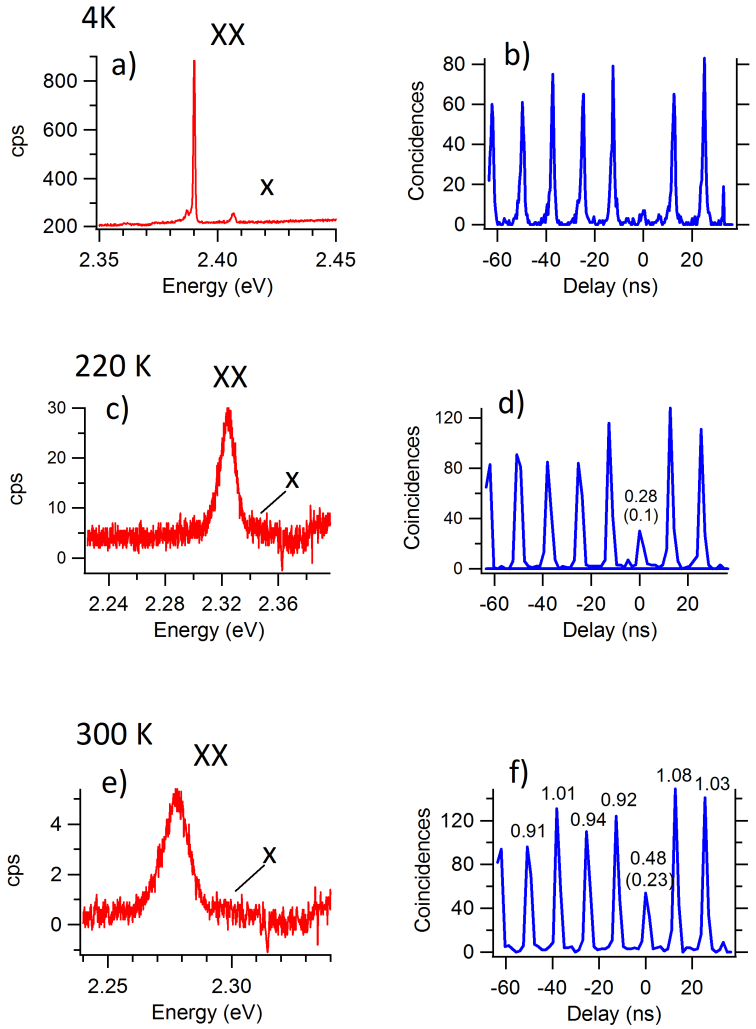

Figure 3.3: (a) and (b): spectra at 4K and 300K. (c) and (d): antibunching figure of the biexciton at 4K and 300K

3.2.4 Noise substraction

One can also evaluate degradation of the antibunching due to the noise coming from luminescence background and APD's dark counts. This noise is poissonian, and has no correlation with the single photon emission. One can show that, if we consider a signal to noise ratio $\rho = \frac{S}{S+B}$, with S the signal intensity and B the noise intensity, then the corrected zero delay normalized peak area is [58]:

$$g^{(2)}_{corr}(0) = (g^2(0) - (1-\rho^2))/\rho^2.$$

After noise substraction (the noise was estimated from spectra) we found a corrected $g^2_{corr}(0) = 0.23$. We discuss in the following why we don't obtain a perfect antibunching with $g^{(2)}_{corr}(0) \approx 0$.

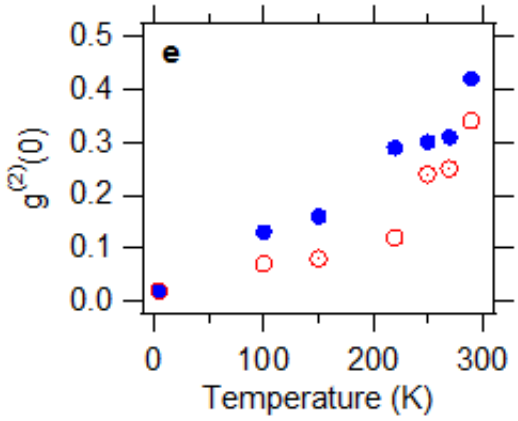

Figure 3.4: Degradation of antibunching with temperature. Blue dots are the measured non corrected $g^2(0)$, and red dots are the corrected values $g^2_{corr}(0)$.

3.3 Biexciton as single photon emitter: pollution from the exciton

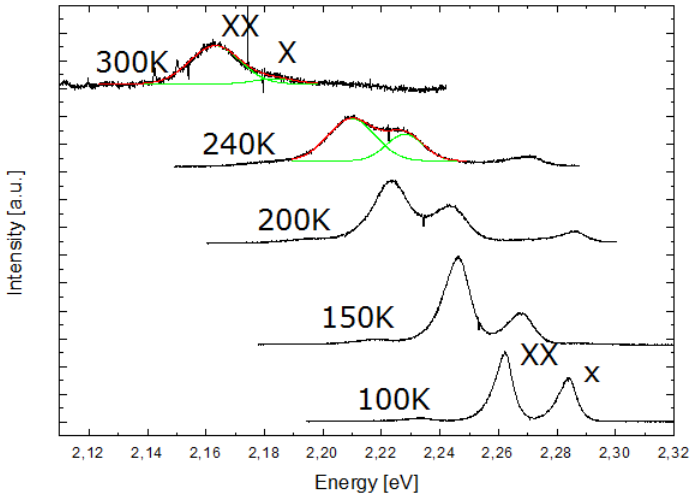

Figure 3.5: Neutral quantum dot spectra under pulsed excitation from 100K to 300K

In chapter 2, we concluded that the exciton luminescence intensity is weaker than the biexciton because the bright exciton state is very efficiently depopulated by a spin flip process towards the dark exciton state. This conclusion also holds at high temperature as shown in fig. 3.5 . Thus we choosed the biexciton as the most adequate transition for single photon production.

Exciton and biexciton send photons by bunches since they come from the same radiative cascade, thus pollution of one line by the other on the zero delay correlation function is enhanced. We can estimate the effect of the pollution of the biexciton single photon signal by the exciton

parasitic emission. Let us suppose we make the autocorrelation of a signal mixing exciton and biexciton emission such as the exciton fraction α is:

$$\alpha = \frac{I_x}{I_{xx} + I_x}$$

with I_x and I_{xx} the integrated intensities of the exciton and biexciton lines respectively sent towards the 2 APD's.

The general expression of the autocorrelation function derived in chapter 1 is:

$$g^2(\tau) = \frac{\rho(\tau \mid 0)}{\rho(\tau)}$$

we decompose this expression with the 4 possible configurations for the occurence of a coincidence caused by the 2 emission lines.

$$g^2(\tau) = \frac{1}{(I_x + I_{xx})^2 \left[\rho(X(\tau)) + \rho(XX(\tau))\right]} . (I_x^2 \rho(X(\tau) \mid X(0)) + I_x I_{xx} \rho(X(\tau) \mid XX(0)) + I_x I_{xx} \rho(XX(\tau) \mid X(0)) + I_{xx}^2 \rho(XX(\tau) \mid XX(0))) \quad (3.1)$$

with $\rho(X(\tau))$and $\rho(XX(\tau))$ the probability to detect a photon coming from the exciton and from the biexciton respectively.

Under pulsed excitation, and for $-T_R/2 \leq \tau \leq T_R/2$, with T_R the repetition time of the pulsed laser, ie after the first excitation pulse and before the second (the excitation pulses duration being around ps), on the 4 terms composing the right side of eq. 3.1, only the cross terms are non-zero, so:

$$g^2(\tau) = \frac{1}{(I_x + I_{xx})^2} \frac{I_x I_{xx} \rho(X(\tau) \mid XX(0))}{\rho(X(\tau)) + \rho(XX(\tau))} + \frac{1}{(I_x + I_{xx})^2} \frac{I_x I_{xx} \rho(XX(\tau) \mid X(0))}{\rho(X(\tau)) + \rho(XX(\tau))} \quad (3.2)$$

The relation between $\rho(X(\tau))$ and $\rho(XX(\tau))$ can be deduced from the ratio between the lines intensities:

$$\rho(X(\tau)) = \frac{I_x}{I_{xx}} \rho(XX(\tau)) \quad (3.3)$$

If we call $g^2(0)$, the quality of the antibunching and, the relative area of the zero delay peak, and not the value of the pulsed autocorrelation function at $\tau = 0$, this quantity can be expressed by integrating eq. 3.2 between $-T_R/2$ and $T_R/2$.

we inject eq. 3.3 in eq. 3.2 after integration,

$$g^2(0) = \frac{I_{xx} I_x}{(I_x + I_{xx})^2} . \int_{-T_R/2}^{T_R/2} \frac{\rho(X(\tau) \mid XX(0))}{\rho(X(\tau))(1 + \frac{I_{xx}}{I_x})} + \frac{I_{xx} I_x}{(I_x + I_{xx})^2} . \int_{-T_R/2}^{T_R/2} \frac{\rho(XX(\tau) \mid X(0))}{\rho(XX(\tau))(1 + \frac{I_x}{I_{xx}})}$$

$$g^2(0) = \left[\frac{I_x}{(I_x + I_{xx})}\right]^2 \frac{I_{xx}}{(I_x + I_{xx})} . \int_{-T_R/2}^{T_R/2} \frac{\rho(X(\tau) \mid XX(0))}{\rho(X(\tau))} + \left[\frac{I_{xx}}{(I_x + I_{xx})}\right]^2 \frac{I_x}{(I_x + I_{xx})} . \int_{-T_R/2}^{T_R/2} \frac{\rho(XX(\tau) \mid X(0))}{\rho(XX(\tau))} .$$

We express this equation with the exciton fraction α defined above.

$$g^2(0) = \alpha^2(1-\alpha)\int_{-T_R/2}^{T_R/2} \frac{\rho(X(\tau) \mid XX(0))}{\rho(X(\tau))} + \alpha(1-\alpha)^2 \int_{-T_R/2}^{T_R/2} \frac{\rho(XX(\tau) \mid X(0))}{\rho(XX(\tau))}. \tag{3.4}$$

$\int_{-T_R/2}^{T_R/2} \frac{\rho(X(\tau)|XX(0))}{\rho(X(\tau))}$ is the central peak relative area of the cross correlation between the exciton and the charged exciton. For the central peak, $\frac{\rho(X(\tau)|XX(0))}{\rho(X(\tau))}$ is non-zero for positive delays. It correspond to the case where the biexciton photon is the start of the measurement. In the same idea, $\frac{\rho(XX(\tau)|X(0))}{\rho(XX(\tau))}$ represents the cross correlation between the exciton and the biexciton, but the central coincidences occur when the exciton pulse arrives to the correlation card delayed with respect to the biexciton pulse. Thus, between $-T_R/2$ and $T_R/2$, this function is non zero only for the negative delays. In fact, $\frac{\rho(X(\tau)|XX(0))}{\rho(X(\tau))}$ and $\frac{\rho(XX(\tau)|X(0))}{\rho(XX(\tau))}$ would represent the same experiment except one difference: between the two experiments we would have switched the wires connecting the APD's to the counting card. After this, it is immediate to conclude that:

$$\int_{-T_R/2}^{T_R/2} \frac{\rho(X(\tau) \mid XX(0))}{\rho(X(\tau))} = \int_{-T_R/2}^{T_R/2} \frac{\rho(XX(\tau) \mid X(0))}{\rho(XX(\tau))}$$

therefore eq. 3.4 becomes

$$g^2(0) = \left[\alpha^2(1-\alpha) + \alpha(1-\alpha)^2\right] . \int_{-T_R/2}^{T_R/2} \frac{\rho(X(\tau) \mid XX(0))}{\rho(X(\tau))}$$

After rearranging the terms with α :

$$g^2(0) = \alpha(1-\alpha)\int_{-T_R/2}^{T_R/2} \frac{\rho(X(\tau) \mid XX(0))}{\rho(X(\tau))} \tag{3.5}$$

This is the product of a function depending on the exciton fraction α and $\int_{-T_R/2}^{T_R/2} \frac{\rho(X(\tau)|XX(0))}{\rho(X(\tau))}$ which is the value of the normalized zero delay peak of the cross correlation between the exciton and the biexciton. Note that for a pure excitonic emission ($\alpha = 1$), or a pure biexcitonic emission ($\alpha = 0$), the $g^2(0)$ is null, as expected for a pure single photon source. Between these two extrema there is a maximum ($\alpha = 0.5$) where the pollution (of the exciton by the biexciton or of the biexciton by the exciton) is the most efficient. In our case, the biexciton intensity is always, $\alpha \leq 0.5$. In fig. 3.6, is plotted $\alpha(\alpha - 1)$ as a function of α. This is the dependance of $g^2(0)$ with the exciton fraction.

$\int_{-T_R/2}^{T_R/2} \frac{\rho(X(\tau)|XX(0))}{\rho(X(\tau))}$ quantifies the correlation between excitation and biexciton emissions and is easily measurable experimentally. As explained in chapter 1 sec. 3 on the bunching effect, it takes values larger than 1. Thus the correlation between the exciton and the biexciton emissions enhances the degradation of the antibunching. In fig. 3.7 is presented a typical measured cross correlation between exciton and biexciton under pulsed excitation. Note that the central peak is symetrical in the measurement because the resolution of the setup (700 ps here) is much larger than the 300 ps of the biexciton lifetime, which, in principle, rules the decrease of the central peak for positive delays. The normalized zero delay peak area is a direct measurement of the correlation part of eq. 3.5. We measured here $\int_{-T_R/2}^{T_R/2} \frac{\rho(X(\tau)|XX(0))}{\rho(X(\tau))} = 3.5$.

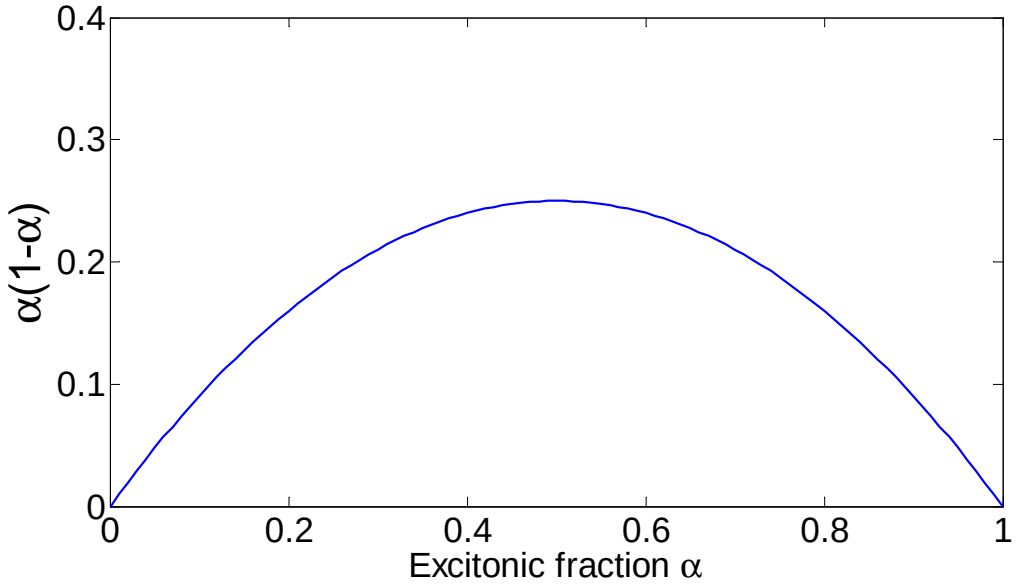

Figure 3.6: Dependance of $g^{(2)}(0)$ with α

Therefore a pollution of the biexciton antibunching by an exciton fraction α in the measurement of 5% results in a measured $g^2(0)$ of 0.17. Thus, because of the correlation between photons emitted by excitons and biexcitons, the degradation of the biexciton antibunching by the exciton is much more efficient than a random poissonnian noise.

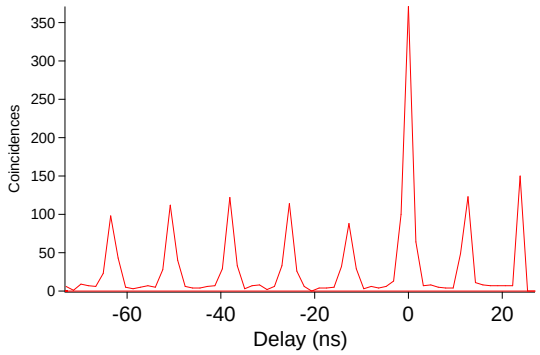

Figure 3.7: Cross correlation of the exciton and the biexciton under pulsed excitation

Weakness of the bright exciton was an advantage that other epitaxied structures able to keep luminescence at high temperature such as GaN quantum dots don't have. Exciton-biexciton mixing caused a too strong degardation of the antibunching ($g^2(0) = 0.7$ at 200K) [52]. Abscence of wetting layer is the cause of the second advantage proposed by the nanowire quantum dots: resistance against temperature.

3.4 Robustness against temperature

The antibunching degradation with temperature also comes from a decrease of the signal to noise ratio with the activation of non radiative processes. This effect can be quantitatively evaluated by investigating the temperature dependence of the biexciton lifetime (fig. 3.8). At low temperature, the biexciton decays radiatively with a decay time (see chapter 2)

$$\tau = \tau_{rad} = \frac{1}{\Gamma_{rad}} = 0.3\,ns$$

The decay rate Γ_{rad} is constant up to around 100 K and then increases due to the appearance of non-radiative channels represented by the rate γ_{nr}:

$$\Gamma = \Gamma_{rad} + \gamma_{nr}$$

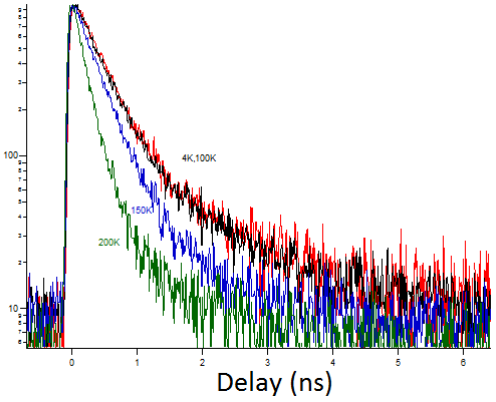

Figure 3.8: Temperature dependence of biexciton decay time

The measured values of $\gamma_{nr}(T)$ follow an Arrhenius law (fig. 3.9):

$$\gamma_{nr}(T) = \gamma_0 e^{-\frac{E_a}{(k_B T)}}$$

with activation energy Ea ranging from 40 to 170 meV depending on the quantum dots (fig. 3.9). Roughly speaking, the activation energy quantifies the energy barrier for the biexciton to disappear non-radiatively.

The actual mechanism is likely to be an escape of a hole to a nanowire surface state or to the ZnSe barrier (holes are less confined than electrons in CdSe/ZnSe heterostructures). With the latter assumption, the largest observed values of Ea are not compatible with a pure CdSe composition in the QD (valence band offset ~ 300 meV), but rather with a $Zn_xCd_{1-x}Se$ ternary alloy with $x \approx 0.5$ Zn intermixing. This QD composition is consistent with the TEM analysis (briefly presented in chapter 1). fig. 3.10 a) shows that low emission energy QDs exhibit large activation energies, fitting with the fact that more energy is required to escape from a deeper potential well (fig. 3.10 b)). According to this criteria, low emission energy QDs should be more robust with respect to temperature.

This study is consistent with temperature resolved macroPL of as grown quantum dots. When temperature is increased photoluminescence energy of quantum dots are shifting because

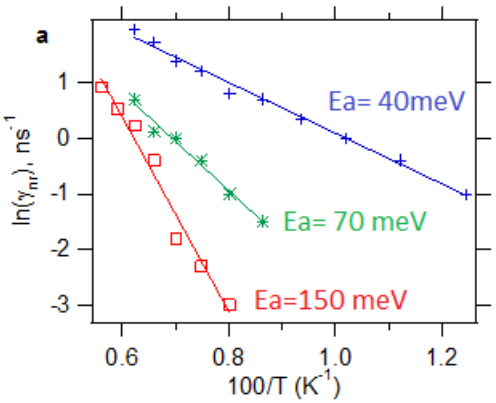

Figure 3.9: Evolution of the non radiative rate with temperature for 3 different nanowires

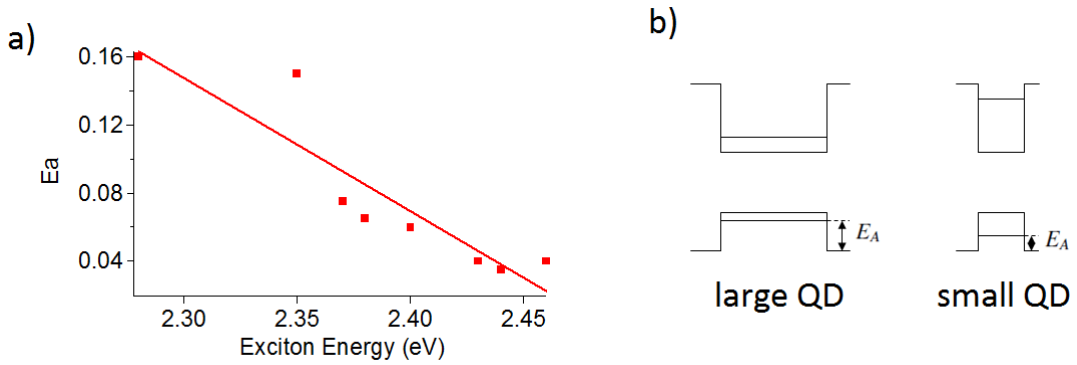

Figure 3.10: a) Activation energy versus exciton emission energy, b) simplified scheme of the interpretation of result presented in (a): E_a is smaller for good confinement, ie small quantum dots.

of dilatation of the crystal lattice . Such shift were measured and fitted using the Varshni's empirical expression.

$$E_x(T) = E_{xx}(0K) - \frac{\alpha T^2}{T + \beta}$$

The parameters values extracted from the fit are: $\alpha = 9.23$ eV/K and $\beta = 234$ K.

In order to study the evolution of photoluminescence of an ensemble with temperature, we removed from the experimental datas the single quantum dot red shift described above.

In fig. 3.11 a) are presented macrophotoluminescence experiment results for increasing temperature, after removal of the single quantum dot red shift caused by temperature on single quantum dots.

Despite this removal we still observe a red shift. This is due to the dependence of the activation energy, which is not the same for every emission energy. Low energy quantum dots are resisting better than high energy quantum dots. The high energy side of the gaussian distribution of luminescence energy is decreasing faster than the low energy side.

We reproduced theoretically this experiment by applying to a gaussian photoluminescence energy dispersion, similar to the experimental measurements, an activation energy determinated by the linear fit presented in fig. 3.10. Results of this simulation are plotted in fig. 3.11b). The

ensemble redshift simulated from 4K to 260K is around 20 meV, which is less than the 30 meV observed in the experimental datas. It can come from the fact that we don't really know how are resisting quantum dot emitting at energies lower than 2.25 eV, as we didn't identified any in microPL experiments. We don't even know if contribution to the macroPL curves at such small energies are coming from quantum dots. These macrophotoluminescence experiments are done on "as grown sample". The nanowires are standing on the ZnSe buffer, which luminescence (from defects) is also contributing to the measurement. Anyway, this shift observed in macro PL confirms the observations done on single nanowires.

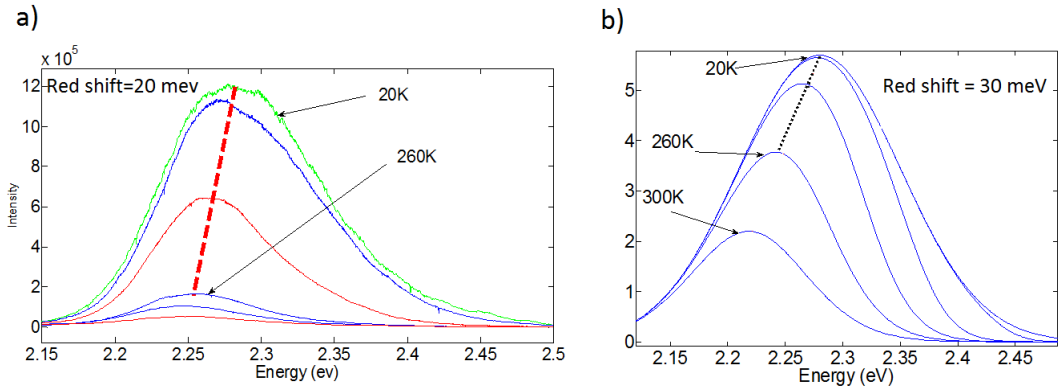

Figure 3.11: a) Experimental macroPL after removal of single quantum dot red shift, the red line represents the red shift of the emission caused by the temperature increase. It is measured at 20 meV, b) Simulated macroPl, black dashed line represents the red shift of the emission caused by the temperature increased from 20K to 260K. This shift is around 30 meV.

We conclude from this that low energy quantum dots are resisting better to temperature and are more appropriated for single photon emission at room temperature, from this point of view.

3.5 Conclusion

We have observed antibunching at 300 K on the biexciton line of CdSe/ZnSe nanowire quantum dots. This is the first time such a result is obtained on an epitaxied quantum dot.

The two important conclusions of this chapter are in contradiction. In one hand, we saw, in the chapter 2 devoted to the influence of the dark exciton, that the bright exciton intensity tends to be weaker for high emission energy quantum dots, reducing the pollution of the antibunching measurement at room temperature. On the other hand, we showed that low energy emission quantum dots were resisting better to temperature. Thus, the single photon quality one expect from a room temperature emitter is found in quantum dots which show the lowest resistance to temperature. In principle, a trade off should be found by picking up quantum dots emitting in average energy, which could show a good temperature robustness, and still have a reduced excitonic intensity.

It has to be said that all this study on the exciton and on temperature resistance was done after obtention of the room temperature antibunching. Therefore, no strategy in the choice of the potentially good quantum dots was adopted, which may have optimized this demanding experiment.

Chapter 4

Dynamic of a charged quantum dot

Until now, we only dealt with neutral quantum dots. In this chapter, we study the dynamic of charged quantum dots. Excitonic or biexcitonic recombinations can occur also in the presence of an excess charge. Coexistence of emission lines coming from charged and non charged excitons on the same spectrum indicates that there is a probability to capture a single charge in the quantum dot. Thus, the quantum dot switches from a "neutral" state to a "charged" state and vice versa. In this chapter we describe how we can identify emission lines of such charged quantum dots, model and optically probe the relations between its different states by photon correlation technique. Then, we will show that this experimental technique applied on biexciton lines allow us to investigate the fine structure of the excited trion, and obtain informations about its relaxation dynamic towards the trion state. At the end we will explain how such measurement provided an indication on the quantum dot charge type.

4.1 Characterisation

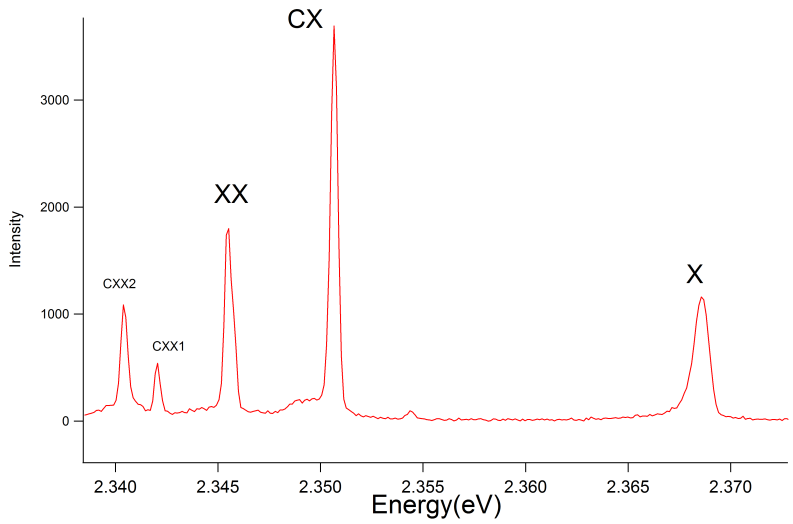

Figure 4.1: Typical spectrum of a charged quantum dot.

A typical spectrum of a charged quantum dot is plotted in fig. 4.1. The five lines correspond to different transitions of the same quantum dot. They come from recombinations of the exciton

X, the charged exciton CX (trion), the biexciton XX, and the two lines labeled CXX1 and CXX2 correspond to the recombination of the charged biexciton towards two different states of the excited trion. We will discuss this last point in section 3 of this chapter. For the understanding and the modeling of the cross-correlation measurements, we will use the equation derived in chapter 1, which is allowing us to simulate the cross correlation figure with a simple set of rate equations. In the case of a radiative cascade ($2 \rightarrow 1 \rightarrow 0$) the cross correlation between 1 and 2 states gives (see chapter 1), for $\tau > 0$

$$g^{(2)}_{1-2}(\tau) = \frac{(n_1(\tau)/n_1(0) = 1)}{n_1(\tau)}$$

with $n_1$and n_2 populations of the two excited levels.
And for $\tau < 0$

$$g^{(2)}_{1-2}(\tau) = \frac{(n_2(\tau)/n_0(0) = 1)}{n_2(\tau)}$$

with n_0 the ground state population.
The set of rate equations we will use is represented by the scheme pictured in fig. 4.3.

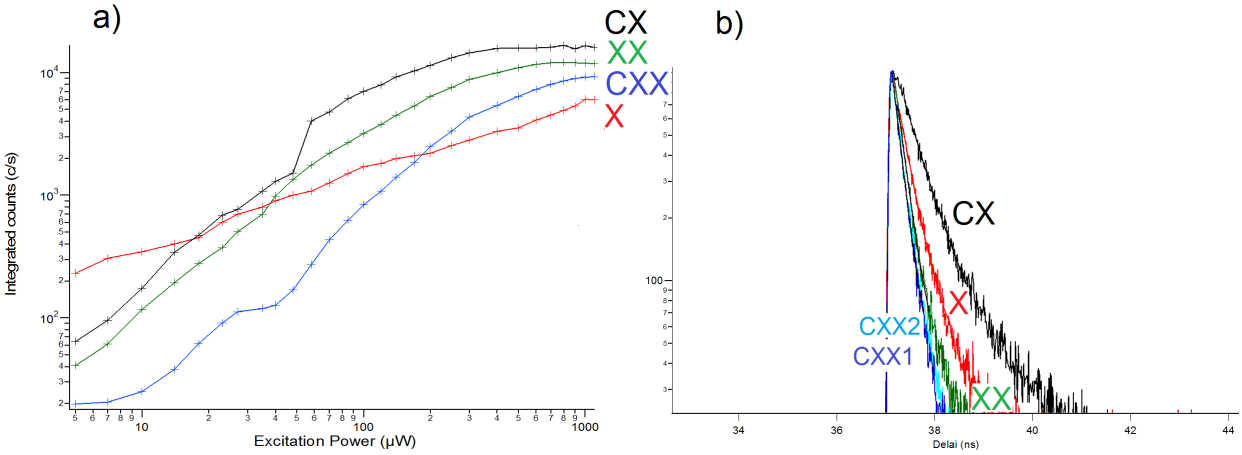

Figure 4.2: (a) Power dependence of the different lines of the charged quantum dot. The intensities of the two lines CXX_1 and CXX_2 were added. (b) Decay time curves of the 5 lines at very low excitation power.

The power dependencies of these transitions measured under pulsed excitation are plotted in fig. 4.2 a). Only the exciton shows linear dependence, the others, XX, CX and the sum of the 2 lines of CXX show quadratic dependence. The exciton saturation value is lower than the biexciton because of the presence of the dark exciton state as discussed in the chapter 2. The charged exciton stauration value is also larger than the biexciton, which would indicate that the quantum dot is more often charged than neutral. And we can also note that the charged exciton is saturating at a larger value than the charged biexciton. This would imply that some transitions from the charged biexciton recombination are missing or are non radiative.

In fig. 4.2 b) we plotted the decay curves for the five lines, at low excitation power in order to avoid effects of radiative cascades. We measured the following decay times: $\tau_d(X) = 320$ ps, $\tau_d(CX) = 400$ ps, $\tau_d(XX) = 250$ ps, $\tau_d(CXX) = 200$ ps. Decay time measurements on CXX1 and CXX2 give the same result. It is not surprising as we are here measuring the initial state

population evolution with time, and as these two transitions have the same initial state (charged biexciton), they show the same decay curve. The exciton has a shorter decay time than the charged exciton, which is unusual. This is also the consequence of very large transition towards the dark exciton state, which is making the decay of bright exciton population faster. The charge states of the quantum dot don't have such dark states.

These preliminary measurements provide informations about the indentity of the lines but they are unsufficient to demonstrate unambiguously their nature and to describe the quantum dot dynamic.

4.2 Dynamic of the charged exciton

Cross correlation measurements involving the charged exciton were performed by Gregory sallen during his thesis [60], on the first generation of nanowire quantum dots which were already exhibiting charge exciton line. As it can be seen in fig. 4.1, the line we attribute to the charged exciton is not at equal distance between the exciton and the biexciton as it has been reported by Sallen et al [59] or in this reference [61], for CdTe/ZnTe SK quantum dots, but is shifted at lower energy, closer to the biexciton. This can come from a different confinement in the quantum dot or by a different doping of the CdSe. We will discuss the problem of the doping type in an other section of this chapter (section 3).

The set of rate equations we will use to fit the datas is represented by the scheme pictured in fig. 4.3. As these experiments are done under continuous excitation, we represent the exciton pump rate by the quantity r, and the charge capture rates by γ_h, γ_e, for the hole and electron respectively. In principle the two last quantities are not equal, and we didn't justify yet the fact we describe the first charge captured as a hole in the model. We will try to bring arguments for this choice.

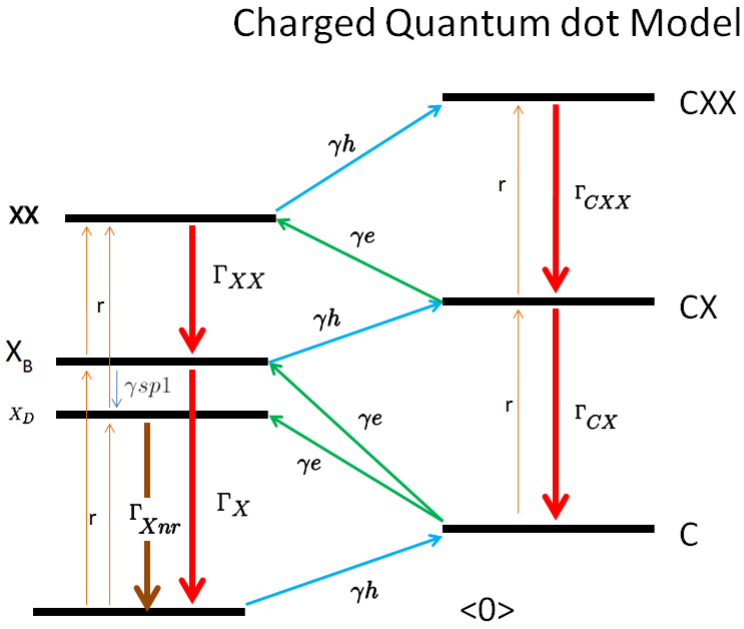

Figure 4.3: Model for a charged quantum dot

4.2.1 Neutral lines

The cross correlation measurement between exciton and biexciton shows similar result as the measurement exposed in chapter 2 about neutral quantum dots. However there is small difference. In fig. 4.4, we plotted the cross correlation figure obtained between exciton and biexciton. We find the typical figure of a radiative cascade with the asymetrical shape and the characteristic bunching at zero delay. In chapter 2, we explained that the zero delay value of the cross correlation function was giving an information about the presence of the exciton in the steady state. Here we measure

$$g^2(0) = \frac{p_x(0,0)}{p_x(\infty)} = 5.5$$

This means that $p_x(\infty) = \frac{1}{5.5} = 0.18$. This is lower than the probability to find an exciton in the neutral quantum dot (p=0.23). This can be explained by the fact that there is now more states in the quantum dot. However, from one quantum dot to the other, it's difficult to make definitive conclusions as the transition rate from bright to dark state of the exciton can change very much, and has a large influence on this measurement (chapter II, section 1).

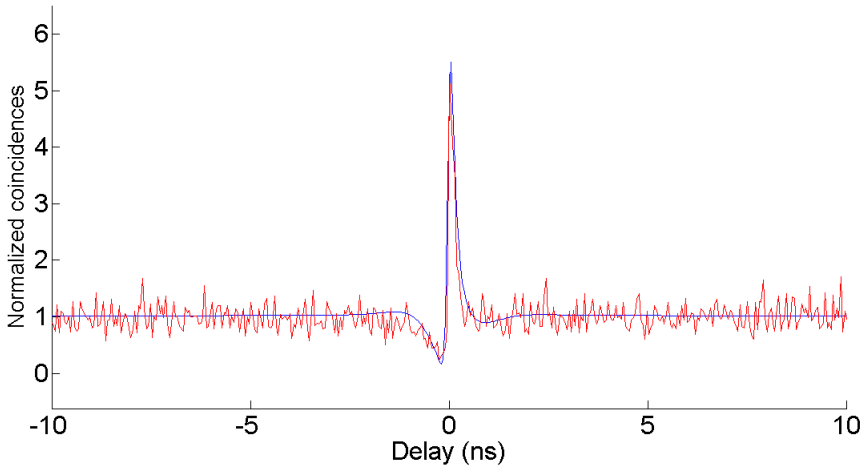

Figure 4.4: Cross correlation of the exciton and the biexciton

4.2.2 Charged lines

We now perform cross correlations between the charged exciton CX line and the neutral lines (X and XX). In fig. 4.5, is plotted the cross correlation figure between exciton and charged exciton. It is also asymetrical but there is no bunching as it was the case between the exciton and the biexciton. Indeed, the two states are not linked by a radiative cascade, but one need a charge capture to go from one to the other. If we consider the positive delays, in fig. 4.5, the start is given by the emission of a photon coming from the exciton. Thus at $\tau = 0$, the quantum dot is empty($\langle 0 \rangle$ state). The characteristic time of the coincidences increase with the delay corresponds to the time it takes for the quantum dot to be pumped in the charged exciton state. This can be done by the capture of 3 charges, or 1 exciton and 1 charge. For the negative delays, the start is given by the emission of a photon coming from the charged exciton recombination. At $\tau = 0$, there is a single charge in the quantum dot, the short time to recover an exciton in the quantum dot is the charge capture time. This is the same process to understand fig. 4.5

b), the cross correlation between CX and XX. This time, for the positive delays, the start is the recombination of a biexciton, and the long time is the time taken by the quantum dot to be pumped from the exciton state to the charged biexciton state. For negative delays, at $\tau = 0$, there is a charged exciton in the quantum dot, and the short time needed to have a charged exciton is the time needed to capture a single charge. To fit the datas, we set the exciton pump rate $r = 4\ ns^{-1}$, $\gamma_h = 0.28\ ns^{-1}$, $\gamma_e = 2.5\ ns^{-1}$. The probability to capture an electron is higher than the probability to capture a hole. But, the doping nature of the quantum dot depends also on the density of free holes or electrons around the quantum dot, thus these measured capture rates are not in contradiction with the hypothesis we made on the doping nature (the hole is captured first).

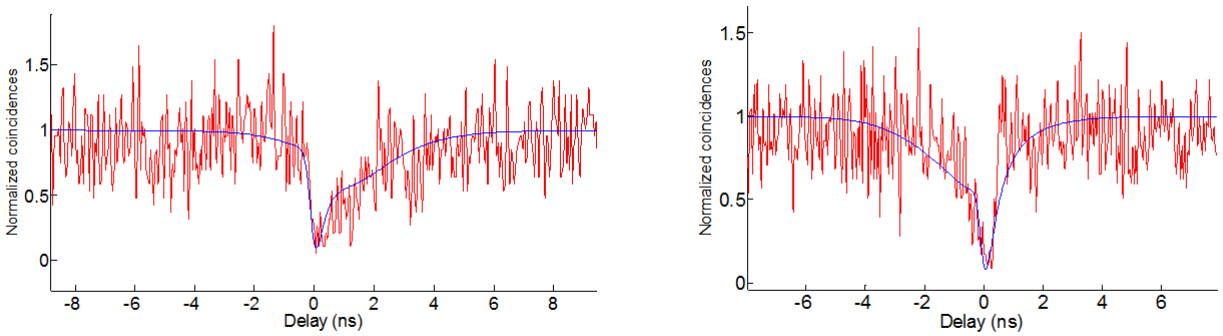

Figure 4.5: a) Cross correlation between exciton and charged exciton. b) cross correlation between charged exciton and biexciton.

In fig. 4.6 the charged biexciton $(CXX1 + CXX2)$/ biexciton cross correlation histogram is plotted. We find a similar non symetrical shape of the antibunching, caused by the non symmetry of pumping rates necessary to go from an exciton to a charged biexciton and to go from a biexciton to a charged biexciton. To fit this histogram, we set the pumping parameter such as: $r = 7\ ns^{-1}$, $\gamma_h = 0.2\ ns^{-1}$, $\gamma_e = 0.5\ ns^{-1}$. These rates are larger than the pumping rates used for the fit of cross correlation figures involving the charged exciton. This is because we used an excitation power larger in order to have enough counts coming from the charged biexciton and the exciton. At relatively low excitation power, in the continuous excitation regime, the exciton is intense, despite presence of the dark exciton, and cross correlation between charged exciton and exciton is easier. At high power, the exciton becomes small but lines corresponding to the biexciton and the charged biexciton are dominating, and the cross correlation measurement between the two charged lines is possible.

These measurements are unambiguous proof of the nature of the lines present in the spectrum plotted in fig. 4.1. We showed that the lines labeled "exciton" and "biexciton" were linked by a radiative cascade, as it was the case for neutral quantum dots. We showed that, a charged exciton line is coexisting with the neutral lines. The charged exciton is not as directly linked to neutral states (XX and X) as it is for a radiative cascade. One need a charge capture to go from an exciton to a charged exciton. In the next section we demonstrate that the two low energy lines CXX1 and CXX2 are coming from the recombination of an other charge state of the quantum dot (the charged biexciton CXX), and that this recombination leads to a much more complicated situation from the dynamic point of view.

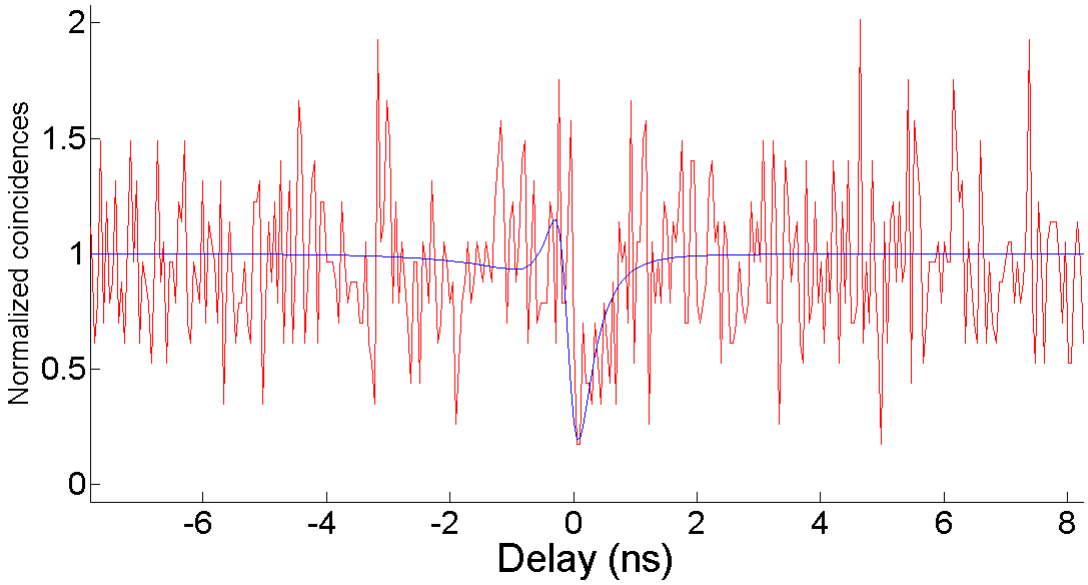

Figure 4.6: Charged biexciton ($CXX1 + CXX2$) / biexciton cross correlation

4.3 Relaxation dynamic of the excited trion

Negatively charged biexciton was already observed in SK CdSe/ZnSe quantum dots[62], with two characteristic emission lines, corresponding to two transitions towards two different states of the excited trion. We propose here to use the photons cross-correlation technique to probe the dynamic of the latter. After recalling the fine structure of the excited trion, we will show that these experiments can provide us some interesting informations about spin relaxation mechanisms and on the doping nature in the quantum dot. Concerning the last point, we will consider from the beginning that the excedentary charge in the quantum dot is a hole, and we will justify this hypothesis in the last part of this section.

4.3.1 Charged biexciton recombination

In fig. 4.7 a), we draw a scheme of the charged exciton recombination. The final state of this transition is a single hole in the quantum dot. The two states of the hole 3/2 spin projections -3/2 ($\Downarrow$) or +3/2 ($\Uparrow$) are degenerated if no magnetic field is applied. Since the charged exciton total hole spin M is zero, there is no Electron hole exchange interaction and, as a consequence, a single resonance appears in the optical spectra (line labeled CX). The situation is completely different for the charged biexciton recombination. As illustrated in fig. 4.7 b), The charged biexciton is composed by two excitons in the s shell and an excedentary hole in the p shell. When one exciton is recombining the final state is an exciton in the s shell and a hole in the p shell: we call this complex excited trion that we label X^{+*}. The fine strucure of this excited particle is complicated. As it consists of an electron-hole pair in the s-shell and a hole in the p-shell, there are $2^3 = 8$ possible spin configurations, which naively leads to the eightfold degeneracy. The latter is partially lifted if we take into account the h-h and e-h interaction energies. By describing the fine structure of the final state of the charged biexciton, one can understand the origin of the lines attributed to the charged biexciton recombination, and one can also explain

the mechanisms involved in such transitions.

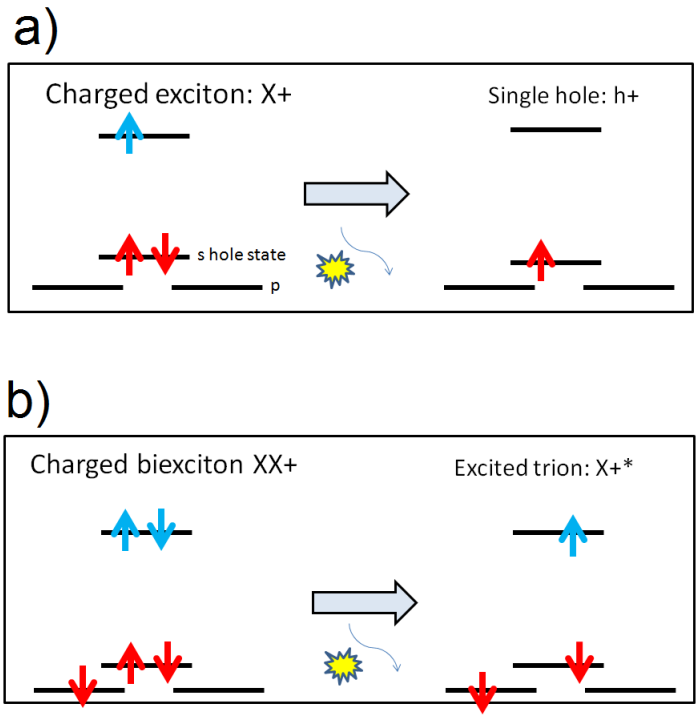

Figure 4.7: Scheme of the transition between a) charged exciton and single hole, b) charged biexciton and excited trion

4.3.2 Excited trion fine structure

In fig. 4.8, we explain how are organized the excited trion spin configurations. Because of holes-holes and electrons-holes carrier interactions , the eightfold degeneracy of X^+ is lifted to four degenerate doublets. The "singlet states" are antisymetrical and are composed by two spin antiparallel holes in the s- and p-shell defining a spin singlet, with total hole angular momentum M=0, and total spin z-projection $f_z = \pm 1/2$. These states can be written as follows in the representation $\mid M, M_z, f_z >$:

$$\mid 0, 0, \pm\frac{1}{2}\rangle = \frac{1}{\sqrt{2}}\left[(\Uparrow_p \Downarrow_s - \Downarrow_p \Uparrow_s) \uparrow\right]$$

with $\Uparrow_s$, $\Uparrow_p$, hole spins in the s and p shell respectively, and $\uparrow$ the electron spin. Only one of the possible spin configurations is presented for convenience.

The "triplet states"are 6 symetrical M=3 states. Their total spin z-projections are respectively

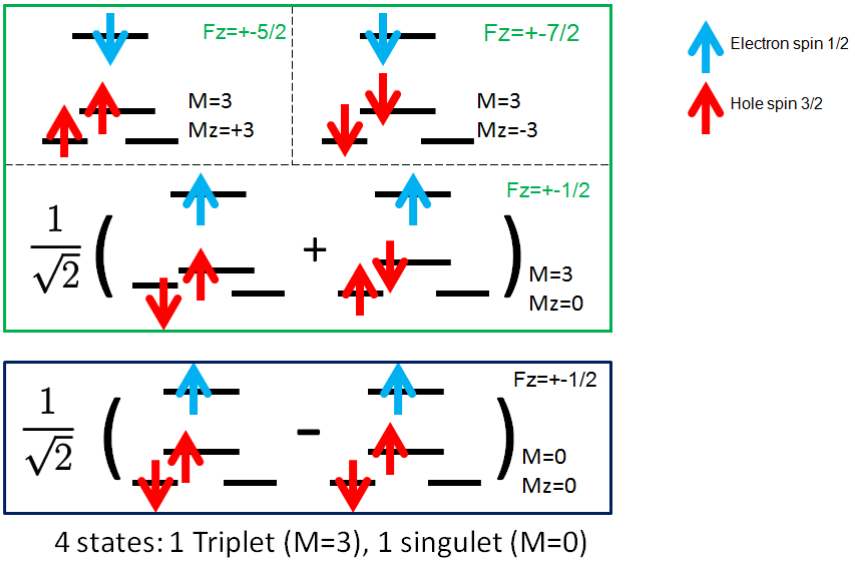

Figure 4.8: Spin configurations of the 4 excited trion states (Only one of the possible electron spin configuration is presented for convenience.)

$f_z = \pm\frac{1}{2}, \pm\frac{5}{2}, \pm\frac{7}{2}$.

$$|\, 3, 0, \pm\frac{1}{2}\rangle = \frac{1}{\sqrt{2}}\left[(\Uparrow_p \Downarrow_s + \Downarrow_p \Uparrow_s)\downarrow\right]$$

$$|\, 3, 3, \pm\frac{5}{2} >= \Uparrow_p \Uparrow_s \downarrow$$

$$|\, 3, -3, \pm\frac{7}{2} >= \Downarrow_p \Downarrow_s \downarrow$$

Total energy of the singlet state is higher than the triplet states due to the isotropic h-h exchange interaction being much larger than the e-h exchange interaction. The positive excited trion fine structure has been calculated by taking into account exchange interaction and coulomb interactions [64], and has been confirmed experimentally by photoluminescence and photoluminescence excitation experiments [64, 65]. In fig. 4.9 is described this fine structure, and the possible transitions from the charge biexciton to excited trion. We also indicated the total angular z-projections of the different states, this quantum number defining the optical selection rules. Thus, the transition from the charged biexciton ($F_z = \pm 3/2$) and the lower triplet state ($F_z = \pm 7/2$) is forbidden. We identitfy the higher charged biexciton energy line in the spectrum, labeled CXX1, to the transition from the charged biexciton to the state $\Uparrow_p \Uparrow_s \downarrow$, and CXX2, the lowest energy line, the transition to the higher energy triplet state $\frac{1}{\sqrt{2}}\left[(\Uparrow_p \Downarrow_s + \Downarrow_p \Uparrow_s)\downarrow\right]$. The transition from the charged biexciton to the singlet state is optically allowed. However, we don't observe it in photoluminescence spectrum. The line corresponding to such a transition should appear at low energy, at an energy difference from CXX1 much larger than the energy difference between CXX1 and CXX2. This transition was observed in positively charged InAs/GaAs quantum dots [67], but was at least one order of magnitude weaker than the two others. The equivalent of this transition in negatively charged CdSe/ZnSe quantum dots, exhibiting charged biexciton lines, was also not observed [62, 63].

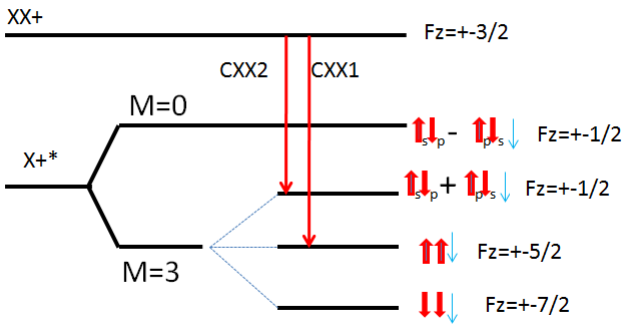

Figure 4.9: Excited trion fine splitting and observed transitions from the charged biexciton the the excited trion. Only electron spin down configuration is presented for convenience.

Spectroscopy on the charged biexciton gives us the opportunity to probe the fine structure of the excited trion, which is much more complex than the charged exciton fine structure. In this context we will see, in the next section that photon correlation is a powerful technique to study its spin dynamic.

4.3.3 Spin Relaxation in the excited trion

From the explanations above, we understand the origin of the observed charged biexciton lines, but we now have to understand how the excited trion can transit towards the charged exciton state. To do so, we will perform cross correlation measurements between the charged biexciton lines and the charged exciton line. In first approximation, one should observe a cross correlation figure similar to the measurements on exciton-biexciton radiative cascades. However, we saw in the previous discussion that an intermediate state (excited trion) exists between charged biexciton and charged exciton. Thus, we don't deal with a direct radiative cascade. We need to study the relaxation of the excited trion to the charged exciton state to understand the correlations between photons emitted from the charge biexciton and from the charge excitons. In fig. 4.10 are represented the relaxation processes of the excited trion leading to the charge exciton state.

After the transition CXX1, the quantum dot is projected in the state $\Uparrow_p\Uparrow_s\downarrow$. The two holes (on the p and s shells) have parallel spins. Because of the Pauli principle, the p hole has to spin flip before relaxing in the s shell and the final state of this spin flip is the singlet state $\frac{1}{\sqrt{2}}\left[(\Uparrow_p\Downarrow_s - \Downarrow_p\Uparrow_s)\uparrow\right]$. The antisymetrical singlet state has the same symetry as the charged exciton (as a fermion). Therefore the excited trion transits through this state before relaxing towards the charged exciton state.

The characteristic time of the p-hole spin flip can be of a few hundred picoseconds, ($\sim$ 1 ns in InAs/GaAs quantum dots [67] and around 70 ps for weakly confined p states in CdTe/ZnTe quantum dots). The singlet state can then relax to the charged exciton state

After the transition CXX2 the quantum dot is projected in the state $\frac{1}{\sqrt{2}}\left[(\Uparrow_p\Downarrow_s + \Downarrow_p\Uparrow_s)\downarrow\right]$. The total angular momentum z-projection of this state is $f_z = \pm\frac{1}{2}$, the same as the singlet state . Thus it only needs a relative phase $\pi-$shift for spin configuration to be excited to the singlet state and subsequently relax in the charge exciton state X^+. This phase shift is considered as very fast, at least an order of magnitude faster than the spin flip of the hole[66]. As a consequence the relaxation process following a CXX2 transition should be much faster than the relaxation process following a CXX1 transition. Then the situation can be simplified, as shown in fig. 4.11,

the charged biexciton recombinations are followed by 2 different relaxation processes, a fast one and a slow one. In the following interpretations, we considere the relaxation from the higher singlet state to the charge exciton state as instantaneous ($\gamma_3 \sim \infty$), and we convolute the figures obtained from the model by the experimental resolution ($\sim 100\ ps$).

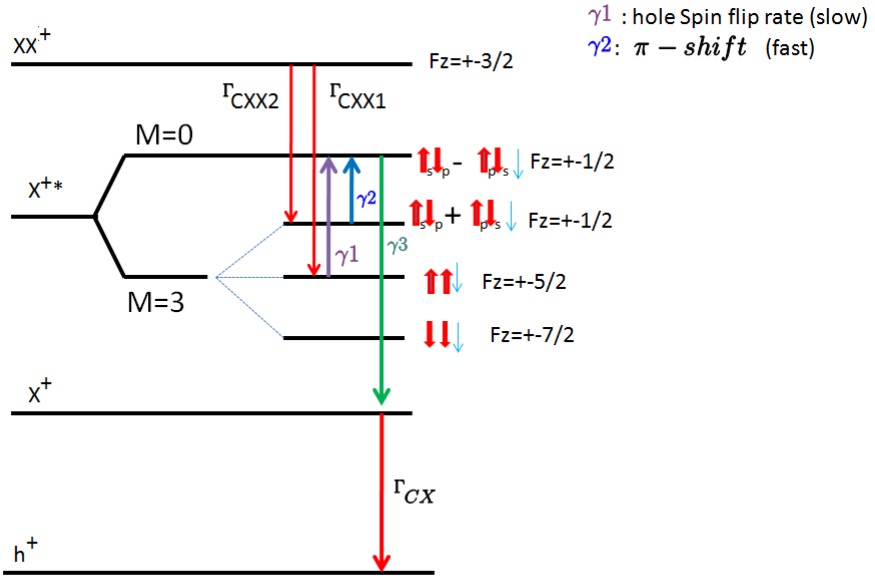

Figure 4.10: Relaxation processes of the excited trion

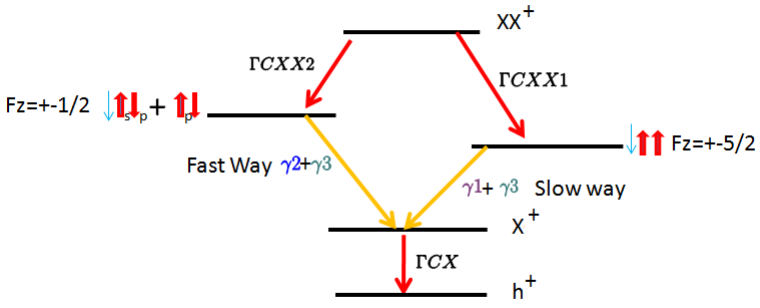

Figure 4.11: Two relaxation ways (fast and slow) for the excited trion

In order to probe these two relaxation times, we performed the cross correlation of the charged biexciton lines with the charged exciton. In fig. 4.12, are plotted the results of these measurements.

fig. 4.12a) shows the $CXX2/X^+$ cross correlation histogram. We obtain again an asymetrical figure, with a strong bunching for positive delays, characteristic of a direct radiative cascade. To fit the experimental datas, we had to set the pumping rate , from the higher energy triplet state to the singlet state, $\gamma_2 = \frac{1}{50}\ ps^{-1}$. The corresponding relaxation time is smaller than the experimental resolution (100 ps). In fig. 4.12 b) is plotted the $CXX1/X^+$ cross correlation

histogramm. We see here the appearence of a slight delay, around the zero delay value, and the bunching is reduced. This means that the quantum dot stayed in the excited trion state for a significant amount of time. From the fit we extract a relaxation time (from $\Uparrow_p\Uparrow_s\downarrow$ to the singlet state) $\tau_1 = \frac{1}{\gamma_1} = 200$ ps ± 50 ps. This is a direct measurement of the spin flip time of the p-hole. This process is here relatively fast compared to measured hole spiflip time in InAs/GaAs quantum dots (1ns) [67], but slower than the measured spin flip times for weakly confined p hole state (70 ps).

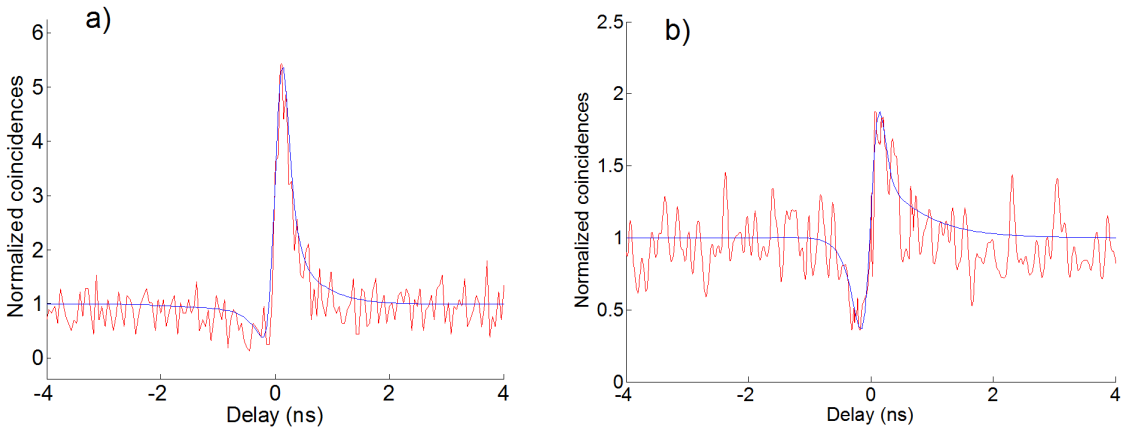

Figure 4.12: a) cross correlation $CXX2/X^+$, b) cross correlation $CXX1/X^+$

4.3.4 Nature of the doping

In the begining of this section, we made a strong hypothesis. We considered that the excedentary charge was a hole, and that the quantum dot was p-doped. This choice can be surprising because the ZnSe material is usually naturally n-doped. For such n doped quantum dots, the excited trion fine structure is different from what we described previously. Indeed the excedentary charge is not a 3/2 spin heavy hole but a 1/2 spin electron. Thus we have to modify the energy orders of the excited trions states. This fine structure[63, 67, 68] is presented and compared the positive excited trion fine structure in fig 4.13. The important modification is that higher triplet state is not an antiparalel electron spins state, but a state with parallel spins and total z-projection momentum $f_z = \pm 1/2$. The antiparalel electron spins state of momentum z-projection $f_z = \pm 5/2$ is at lower energy. In this configuration the excited trion relaxation following CXX2 (the lowest energy biexciton transition) should be the slower one, as it would involve a spin flip of an electron. But as we showed above, the measurements indicate an opposite behaviour. The explanation would be that the excedentary charge in the quantum dot is a hole and the doping is of p-type doping. The most convincing experiment would be to perform photoluminescence of Single-dot on a gated, charge tunable structure allowing the properties of both excitons and biexcitons to be studied in both charge neutral and negatively-charged environments in the presence of excess electrons [69]. However, electrical contacting of nanowire is very difficult and would request a long work of processing and optimization.

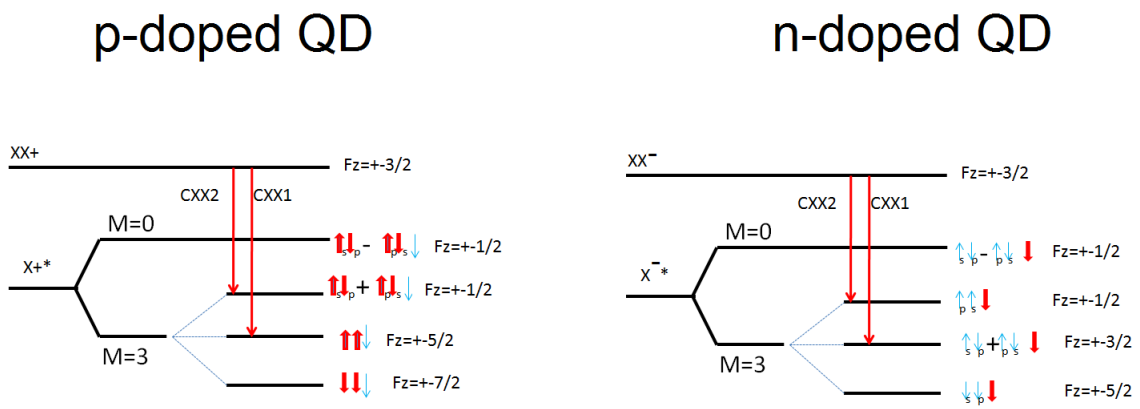

Figure 4.13: Fine structures of the excited trion in the case of a p-doped quantum dot and a n-doped quantum dot.

4.4 Conclusion

In addition of being a very precious tool for unambiguous identification of the numerous lines of a charged quantum dot, the photon correlation technique proved to be a powerful technique when used to study the charged exciton dynamic and the different processes ruling the relaxation of the excited trion different states, when their characteristic times were accessible to our limited temporal resolution. For exemple we saw that the spin flip time of the excess p hole was of the order of 200 ps, and that the relative phase $\pi-$shift was too fast to be measured by our setup. It also permitted to bring clues in the determination of the doping type of the quantum dot without electrical excitation.

Chapter 5

Spectral diffusion

In the introduction of this manuscript, one of the key issues we addressed was the stability of the single photon emitter. We underlined the fact that, as it is the case for any condensed matter system, the emitter is coupled with its environnement. The result of this undesirable coupling is an increase of the transition linewidth. The emitter produces photons at different energies, according to an energy distribution larger than what is imposed by the radiative lifetime. This is a severe limitation for two photons interference operations, as one needs to use photons as identical as possible. The nature of the environnement influences can be diverse. From all the possible processes, two have a strong impact in our system. The well known phonon-broadening is effective when the excitonic recombination can occur by the emission of a photon and the emission or absoprtion of a phonon from the surrounding crystal simultaneously. The energy of the photon emitted is randomly shifted depending on the energy of the emitted or absorbed phonon. In principle, for the next single photon emission, the system doesn't keep the memory of the previous emission energy. Thus, this is an uncorrelated process with respect to the time. On the contrary, the second process we will consider is very different: this is the spectral diffusion. It is caused by the electronic fluctuation of the environnement. As one can define a correlation time of such fluctuations, the spectral diffusion is a correlated process. The energy of an emission depends on the energy of the previous emission. One can approximate it as a first order Markovian process: the emission energy depends on the previous emission, but not on a older emission (see annexe). This type of process is sometimes called "short memory" process.

We saw in the third chapter that the autocorrelation of the emitted intensity field allowed us to define the emission statistic. We will show in this last chapter that, by putting energy conditions on the detection of this field, one can probe the emission energy statistic of the emitter. The two processes influencing its emission energy having very different statistics, they have different consequences on the correlation measurements we perform. The aim of this chapter is to describe and model the signatures of these processes and show that it is possible to extricate them and evaluate their relative importance.

At the end we will also study the influence of excitation power and temperature on the fluctuations of the environnement. Thanks to the Kubo Anderson model, which was recently adaptated to the physics of the semi-conductors [104], we will be able to interpret the experimental results.

5.1 Phenomenon description

5.1.1 Definition

Spectral diffusion is a random evolution of the emission energy of a single object or an ensemble of objects. This is the result of fluctuating properties of the environment regarding the spectrum of the studied object. This phenomen was observed in many different systems such as single molecules[81], ensemble of nuclear spins[73], organic glasses[74] and quantum dots[77]. The sources of spectral diffusion can be very diverse, depending on the nature of the fluctuating reservoir. The fluctuation times can range from nanoseconds to several seconds and the total amplitude from a few μeV to several meV[75]. This effect is an important inconvenience for the use of quantum dots as single photon emitters: the energy emission cannot be precisely determined. Colloidal quantum dots are highly concerned by this problem. Their emission can fluctuate on tens of meV and they are usually blinking at the same time[76], even if with careful processing, it recently became possible to reduce[79] or anihilate this effect[80].

5.1.2 Examples and sources

Spectral diffusion on magnetic nuclear resonance (NMR)

In 1954, Carr and Purcell showed that magnetic nuclear resonance spectra were influenced by spectral diffusion. In presence of a magnetic field the nuclear spin is orientated towards 2 directions: parallel and anti-parallel with respect to the magnetic field. The energy splitting between these two states is $\Delta E = \gamma \hbar B$ where γ is the gyromagnetic factor and B the magnetic local field.

In condensed phases, thermal activation perturbs the nuclear spin orientations, producing a fluctuation of the local magnetic field and modifying the splitting ΔE [73, 2]. The effect of these fluctuations on the NMR spectrum is a type of spectral diffusion. Temperature dependence of this fluctuations showed a very original effect[78]: the NMR spectrum narrowing, called motionnal narrowing with increasing temperature. This effect will be briefly mentionned in section 3.2.4. as a regime predicted by the Kubo Anderson model.

Organic glasses:

It is possible to mesure the absorption of organic glasses by making hole burning experiments[88] (see section 3.1.2). This is how Small et al. obtained hole width larger than the T_2 of the system[80]. This experimental result can be explained by molecular mouvements possible in glasses. In such disordered systems a lot of microarrangements are possible and the cristalline structure evolves with time. Schulte et al. modelized these structural microarrangement fluctuations by a two level system, TLS, (see section 3.2.1). They gave quantitative interpretations of the measured hole burning widths.

Single molecule:

Looking at single objects brings more informations about this phenomen as it becomes possible to measure the fluctuation time. Lu et al. studied Photoluminescence of a single cholesterol oxidase molecule[81] and were able to record its intensity fluctuation. They noticed that the latter evolves with time by random jumps fig. 5.1. This can be explained by considering the fluctuation of the molecule between a bright state and a dark state: it is the blinking phenomen. These two states correspond to two different chemical compositions of the molecule. The molecule in bright state

(called E-FAD) transits to the dark state (E-FADH_2) after a reduction reaction. The enzym can then go back to the bright state (oxidized state) in the presence of dioxygene. By mesuring in real time the intensity fluctuations it is possible to follow the kinetic of the chemical reaction sustained by the molecule.

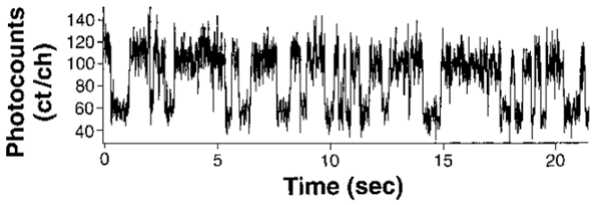

Figure 5.1: Emission evolution of the molecule with time [81]

Colloidal quantum dots:

Spectral diffusion on colloidal quantum dots was the subject of numerous studies in the last 15 years[75, 83, 84]. The typical spectral width of these structures can be relatively large, several orders of magnitudes larger than the lorentzian broadening imposed by the exciton or charged exciton lifetime. Measurements of the spectral jitter due to the spectral diffusion can be done on an ensemble of quantum dots or on a single object.

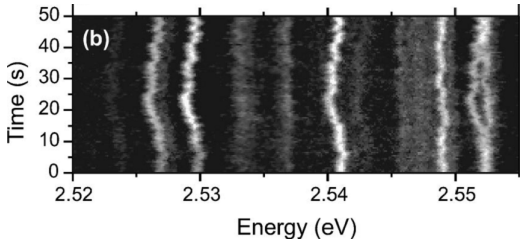

Figure 5.2: Temporal evolution of the emission of a few quantum dots[85]

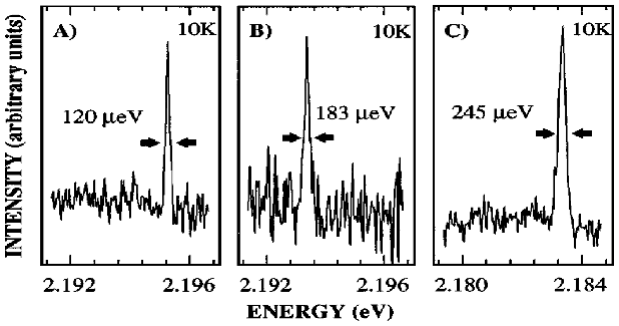

Figure 5.3: Three 1 min spectra of the same quantum dot.[75]

fig. 5.2 shows the temporal evolution of the emission of a small ensemble of quantum dots (QD's). We can clearly see that some groups of lines are jittering synchronously. The jitter of the lines is attributed to random change of the electronic environnement of the quantum

dots. Defects in the vicinity of the quantum dots randomly change their charge state, trapping or releasing carriers, and thus generating fluctuating electric fields that can reach a strength of several tens of kV/cm at the position of the QD's[86]. The measurement is here possible on a simple CCD camera with millisecond acquistition time because the fluctuations are slow (milliseconds to hundred of milliseconds charcteristic times).

Fig. 5.3 (S. A. Empedocles et al. [75]), shows 3 different spectra of the same single quantum dot integrated over 1 minute at low pump power. Not only the position of the line changes but its shape also evolves from one spectrum to the other, which means that fluctuations happen in a timescale much longer than 1 minute.

Another interesting information is the fluctuation amplitude under different conditions. It is easy to access it if this amplitude is larger than a few hundred of μeV as it can be mesured by a direct observation on single quantum dot spectra. On fig. 5.4 (a) is presented the linewidth (averaged on more than 30 quantum dots) versus the excitation intensity. It clearly shows that the amplitude gets larger as the pump rate is increased. This is consistent with the scenario of charges randomly trapped in the vicinity of the quantum dot as the amplitude of the Stark shifts created by them are dependent on the number of carriers injected near the nanocrystal.

fig. 5.4(b) shows the influence of the environnement. Overcoated quantum dots are less sensible to the excitation intensity than uncoated ones. This difference is explained by the presence of ZnS shell forcing trapped charges to reside farther away from the quantum dot, reducing the internal electrical field[87, 90].

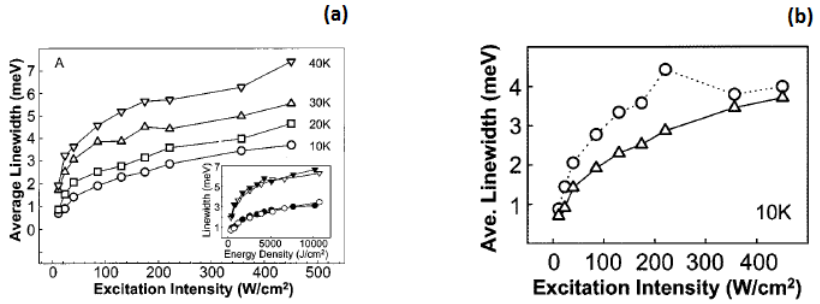

Figure 5.4: (a) Linewidth excitation intensity dependence at different temperatures, (b) influence of the quantum dot environnement: average linewidth power dependence in 56 uncoated quatum dots and 40 coated quantum dots (circles: uncoated, triangles: coated).[84]

Epitaxied quantum dots:

Similar observations were reported for epitaxied self assembled quantum dots [88, 89]. fig. 5.5 shows the temporal evolution of the emission spectrum of an ensemble of InAlAs quantum dots. The 2 arrows on the right of the figure indicate the time when power is increased. Spectral diffusion is activated during this high power period.

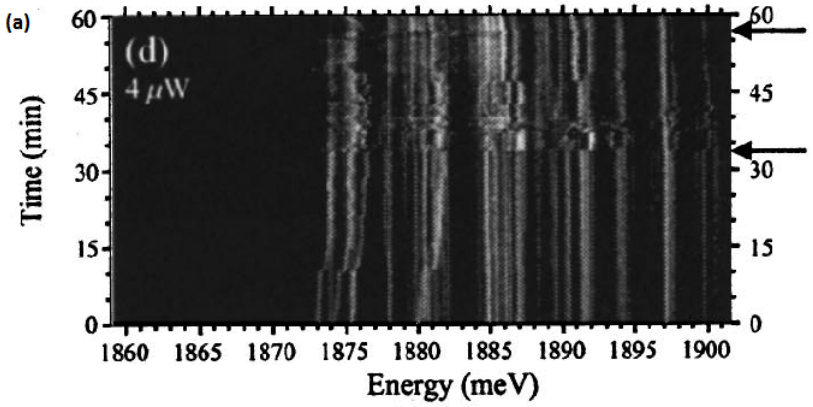

Figure 5.5: Temporal evolution of the emission spectrum of several InAlAs/GaAs quantum dots[88]

On single II-VI quantum dot emission spectrum (fig. 5.6), energy fluctuations can be followed in real time[88]. Optically excited carriers trapped in the vicinity of the quantum dots randomly screen the local electric field . Because of the Stark effect, the exciton emission energy is modified by the trapping or escape of the carriers surrounding the quantum dot. The synchronized fluctuations of the three energy lines show that they belong to the same quantum dot and are influenced by the same environnement. Fluctuations times are here on the order of several seconds and the "homogeneous" lines are larger than 100 μeV, which represents a two orders of magnitude higher energy than what is imposed by the $T_2$of the system. Robin et al. explain this carrier trap/escape influence by the presence of stacking defaults in the wetting layer (see fig. 5.1.2). As the carriers are photocreated, the more the power is increased, the more free charges are created, and thus, the more trap/escape processes happen. This explains the spectral diffusion activation with power indicated in fig. 5.5 for InAlAs quantum dots.

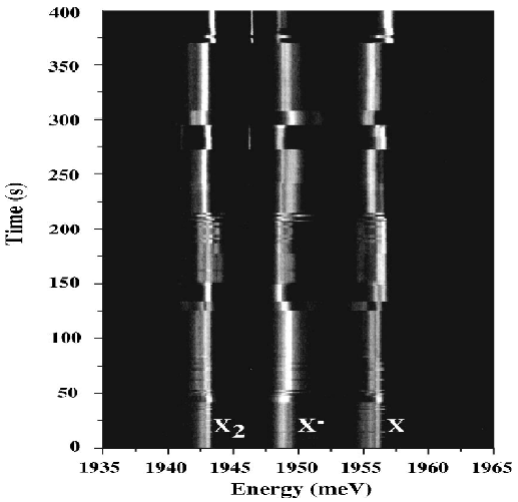

Figure 5.6: Temporal evolution of the emission spectrum of a single CdTe quantum dot[90]

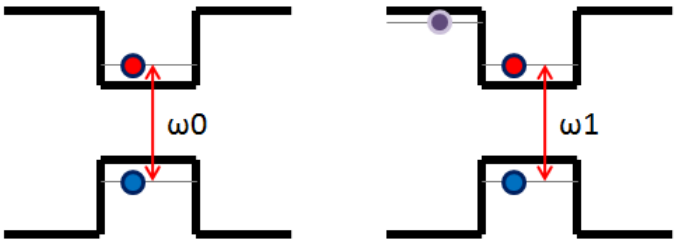

Figure 5.7: Quantum dot Stark effect modelisation. The presence of a charge in the vicinity of the quantum dot modifies the local electric field and Stark shifts the transition energy.

5.1.3 Problems of the spectral diffusion on the coherence of the quantum dots emission

Indistinguishable single photons emission

Most proposed applications for single-photon sources in the field of quantum information (except quantum cryptography[91]) involve two photons interference. Such applications include quantum teleportation[92], post selective production of polarization entangled photons[93], and linear-optics quantum computation[94]. To perform successfully these operations, consecutive photons emitted by a single photon source need to be identical and exhibit two-photon interference effects. If we consider two photons interfering at the same spatial point we can quantify their ability to interfer efficiently by the mean overlap between the two photons wavepackets:

$$V(\Delta t) = \langle | \int x(t) y^*(t+\Delta t) dt \, |^2 \rangle$$

with x(t) and y(t) the photons wave packets, Δt is the the time delay between the two photons arrivals. For two ideally indistinguishable photons, the overlap at zero delay is perfect and $V(0) = 1$.

After the early works of Hong ou and Mandel on two-photons interferences[124], the first result on indistinguishablility of single photons emitted by epitaxied quantum dots was reported by Santori et al.[95]. They tested the two photon-interference quality of semi-conductor quantum dots with the following methode: The quantum dot is excited twice every 13 ns by a pair of equally intense pulses with 2 ns separation. Two pulses, each containing zero or one photons, emerge from the single mode fibre. They are split into two arms by a beam splitter, with one arm $(2ns + \Delta t)$ longer than the other. The beams then recombine at a different place on the same beam splitter. The two outputs of this interferometer are collected by photon counters, and a photon correlation histogram is generated of the relative delay time $\tau = t_2 - t_1$ for two photons coincidence events, where $t_1$and t_2 are times at which photons are detected at detectors 1 and 2, respectively. The central peak of the resulting correlation figure gives them access to the mean overlap between the 2 successive photons $V(\Delta t)$. They find that the mean overlap decreases with Δt with a characteristic time similar to the radiative lifetime, as it should be the case for an ideal single photon emitter. However, interferometry measurements revealed relatively short coherence length ($\tau_c > 2\tau_s$), with τ_s the radiative lifetime. The conclusion is that the primary spectral broadening mechanism is a spectral diffusion occuring at a timescale of more than 2 nanoseconds.

This aspect is very interesting: one can avoid spectral diffusion mechanism by forcing the single photon source to emit photons at a rate larger than the diffusion rate, allowing to optimize

indistiguishability of emitted photons, and therefore, its ability to produce reliable 2 photons interference operations. Information about spectral diffusion such as correlation time of the fluctuations can be very helpful to choose this emission rate before setting up such operations.

Effect on single spin memory

Since several years, it has been proposed to use the excedentary electron spin of the trion as a qubit [119, 120]. A pumping laser, resonnant with the transition ($|\downarrow\rangle \rightarrow |\downarrow\uparrow, \Downarrow\rangle$), ($\uparrow$ representing electron spin state and $\Uparrow$ representing electron spin state), which power is optimized to have all the $|\downarrow\rangle$ state population completely initialized to $|\uparrow\rangle$ provides the initialization.Then, a second "rotation laser" is added, with varying power, and photons count rates are measured from the transition ($|\downarrow\uparrow, \Downarrow\rangle \longrightarrow |\uparrow\rangle$) and, as shown in fig. 5.8, one can observe Rabi oscillations between the two spin states[121].

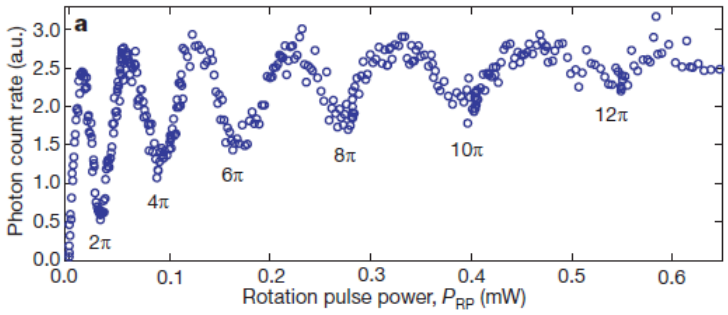

Figure 5.8: Rabi oscillations between the spin states evidence: photon signal versus rotation pulse power [121]

The amplitude of the Rabi oscillations decreases owing to incoherent processes such as trion dephasing. This can be understood as a decrease of the length of the Bloch vector of the two state system. Spectral diffusion can take an important part on such dephasing as it randomly shifts the trion state energy. This is an effect to avoid. The information on the excedentary electron spin might be lost quickly, it adds a limitation on the number of operations done with a qubit.

Of course such considerations are not relevant for semi-charged quantum dots, with alternance between charged and neutral exciton. Indeed, the information stored in the excedentary charge is destroyed each time an other charge neutralizes the quantum dot.

5.2 Theory and model

For the description of spectral diffusion, the Kubo Anderson seems the most apropriate. Despite a few approximations, it successfully predicted the motional narrowing observed in RMN spectra. During her thesis, where she demonstrated for the first time, motional narrowing on epitaxied quantum dots, Alice Berthelot succeeded to explain unconventionnal experimental results by adaptating this model to the environnement of a semi-conductor quantum dot. We will recall here how is constructed this theory, in particular how is built a realistic random process describing the electronic environnement of a quantum dot at the price of certain approximations. It will allow us to interpret our experimental results obtained by modifying excitation power and temperature, in the last section of this chapter.

5.2.1 Emission spectrum of a frequency fluctuating emitter

Relaxation function

As the system is influenced by fluctuation of its environment, the transition frequency of the two level system is a random variable $\omega(t)$. The dipole $\mu(t)$ evolution is described by the differential equation:

$$\frac{d\mu(t)}{dt} = i\omega(t)\mu(t) \tag{5.1}$$

After inegration on time:

$$\mu(t) = \mu(0)exp\left(i\int_0^t \omega(\theta)d\theta\right) \tag{5.2}$$

$\omega(t)$ can be decomposed as:

$$\omega(t) = \omega_0 + \delta\omega(t) \tag{5.3}$$

ω_0 is the transition frequency mean value $\langle\omega(t)\rangle_T$ $\delta\omega(t)$ is its fluctuating part, and $\langle\rangle_T$ represents the averaging over a periode T. The dipole autocorrelation function is:

$$\langle\mu^*(t+\tau)\mu(t)\rangle_T = \mid \mu_0 \mid^2 \phi(\tau)exp(-i\omega_0\tau) \tag{5.4}$$

$\phi(\tau)$ is the so called "system relaxation function". Its expression is:

$$\phi(\tau) = \langle exp(i\int_0^\tau d\theta\delta\omega(\theta))\rangle_T \tag{5.5}$$

The relaxation function is very important as it quantifies the accumulated phase caused by the random fluctuations $\delta\omega(t)$. It also has a direct relation with the intensity spectrum defined in the next section.

We obtain an analoguous relation for the electrical field autocorrelation function:

$$\langle E(t+\tau)E(t)\rangle_T = \mid E_0 \mid^2 \phi(\tau)exp(-i\omega_0\tau) \tag{5.6}$$

Hence$\mid \phi(\tau) \mid$verifies the equation:

$$\mid \phi(\tau) \mid = \frac{\mid \langle E^*(t+\tau)E(t)\rangle_T \mid}{E_0^2} = g^{(1)}(\tau) \tag{5.7}$$

$g^{(1)}(\tau)$ is the first order correlation function of the field.

Intensity spectrum and Wiener-Khintchine theorem.

The Wiener-Khintchine theorem asserts that the autocorrelation function of a stationnary random process and the intensity power (or spectral density) of the process form a Fourier transform pair:

$$S(\omega) = \frac{1}{2\pi}\int_{-\infty}^{\infty}\langle E^*(t+\tau)E(t)\rangle e^{i\omega\tau}d\tau \tag{5.8}$$

We can deduce a simple relation between the intensity spectrum and the electrical field.

$$\langle E*(t+\tau)E(t)\rangle_T = TF[S(\omega)] \tag{5.9}$$

introducing equation eq. 5.7 in eq. 5.9:

$$\mid \phi(\tau) \mid = \frac{\mid TF[S(\omega)] \mid}{E_0^2} \tag{5.10}$$

The relaxation function is the Fourier transform of the intensity spectrum. As defined in equation eq. 5.5 it is a time average value of the random variable $\delta\omega(t)$. To obtain the spectrum we need to know its probability distribution $P(\delta\omega)$.

5.2.2 Spectral diffusion modelisation: Random telegraph noise

Based on works achieved by Kubo[97], Anderson[98] and Burstein[99, 100], Eberly et al. [101] developped a model based on an arbitrary number of fluctuating two level systems (TLS) to describe theoretically the fluctuations of noisy laser-atom interactions. All this work is based on an elementary simple random process called "random telegraph signal'.'

Random telegraph noise: interaction with a TLS

The random process (fig. 5.2.2) called "random telegraph signal" $\delta\omega(t)$ takes on two fixed values, a and -a, alternately and jumps instantaneously between them at completely random times, at an average rate $\frac{1}{T}$.

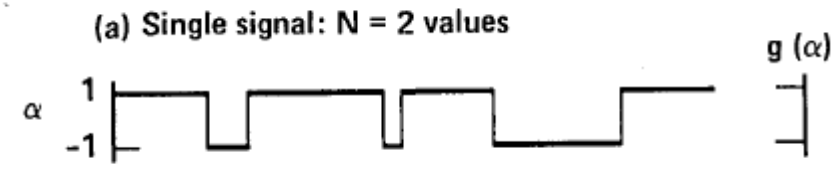

Figure 5.9: Illustrating a realization of the random telegraph signal $\delta\omega(t)$[101]

We first consider a single TLS and want to know how it is influencing the emitter spectrum. In this case the enegry evolves around its mean value ω_0. Its variable part $\delta\omega(t)$ oscillates by random jumps between +a and -a.

Let us now calculate the autocorrelation function $\Gamma(\tau) = \langle\delta\omega(t)\delta\omega(t+\tau)\rangle$.The product $\delta\omega(t)\delta\omega(t+\tau)$ can take on only two values a^2 or $-a^2$. If $\delta\omega(t)$ has switched an even number of times in the interval from t to $t+\tau$ then $\delta\omega(t)\delta\omega(t+\tau) = a^2$, whereas the product yields $-a^2$ if there have been an odd number of switches. If $p(n,\tau)$ is the probability of n switches in the interval τ, it follows that

$$\Gamma(\tau) = a^2 \sum_{n=0,2,4,\ldots}^{\infty} p(n,\tau) - a^2 \sum_{n=1,3,5}^{\infty} p(n,\tau)$$

$$= a^2 \sum_{n=0}^{\infty} (-1)^n p(n,\tau). \tag{5.11}$$

As the switches occur at random at an average rate $\frac{1}{T}$, $p(n,\tau)$ is a Poisson distribution with parameter $\langle n\rangle = \frac{\tau}{T}$, i.e.

$$p(n,\tau) = \frac{(\tau/T)^n e^{-(\tau/T)}}{n!}.$$

When this expression is inserted into eq. 5.11 it yields

$$\Gamma(\tau) = a^2 \sum_{n=0}^{\infty} \frac{(-\tau/T)^n e^{(-\tau/T)}}{n!}$$

for $\tau \geq 0$,

$$= a^2 exp(-2\frac{\tau}{T})$$

and since $\Gamma(-\tau) = \Gamma(\tau)$,

$$\Gamma(\tau) = a^2 exp(-2\frac{\mid \tau \mid}{T}) \tag{5.12}$$

It is possible to link the autocorrelation function with the relaxation function defined in section 2.1.1:

$$\phi(\tau) = \langle exp(i\int_t^{t+\tau} d\theta\delta\omega(\theta))\rangle_T = \langle f(\tau)\rangle_T$$

$f(\tau)$ is a function defined such as:

$$exp(i\int_t^{t+\tau} d\theta\delta\omega(\theta)).$$

If we differentiate $f(\tau)$ with the delay we have:

$$\frac{d}{d\tau}f(\tau) = i\delta\omega(t+\tau)f(\tau)$$

$$f(\tau) = 1 + i\int_0^{\tau} ds\delta\omega(t+s)f(s)$$

By combining the two previous equations:

$$\frac{d}{d\tau}f(\tau) = i\delta\omega(t+\tau)\left[1 + i\int_0^{\tau} ds\delta\omega(t+s)f(s)\right] \tag{5.13}$$

We calculate the stochastic average $\langle f(r)\rangle$, decorrelating $\delta\omega(t+s)$ from the function $f(s)$. This is possible because the random telegraph is a Markov process which has the following property:

$$\langle\delta\omega(t_1).....\delta\omega(t_n)\rangle = \langle\delta\omega(t_1)\delta\omega(t_2)\rangle\langle\delta\omega(t_3).....\delta\omega(t_n)\rangle$$

if $t_1 < t_2 < t_3 < ..... < t_n$.
using this property and eq. 5.13 ,$\phi(\tau)$ satisfies the equation[102]:

$$\frac{\partial\langle f(\tau)\rangle}{\partial\tau} = \frac{\partial\phi(\tau)}{\partial\tau} = -\int_0^{\tau} ds\langle\delta\omega(\tau)\delta\omega(s)\rangle\phi(s) = -\int_0^{\tau} ds\Gamma(\tau-s)\phi(s) \tag{5.14}$$

Injecting the autocorrelation function of $\delta\omega$ obtained in eq. 5.12:

$$\frac{\partial\phi(\tau)}{\partial\tau} = -a^2 \int_0^\tau ds.exp(-\frac{2}{T} \mid \tau - s \mid)\phi(s) \tag{5.15}$$

The solution of such an equation is written as:

$$\phi(\tau) = \frac{1}{2}(\frac{1}{T\lambda} + 1)exp(-(\frac{1}{T} - \lambda) \mid \tau \mid) - \frac{1}{2}(\frac{1}{T\lambda} - 1)exp(-(\frac{1}{T} + \lambda) \mid \tau \mid) \tag{5.16}$$

with $\lambda^2 = \frac{1}{T^2} - a^2$.

As explained in section 2.2.1, the intensity spectrum is the inverse Fourier transform of the autocorrelation function of the electrical field E(t).

$$S(\omega) \propto TF^{-1}[\langle E(t)E^*(t+\tau)\rangle]$$

$$\propto \frac{\frac{8\pi a^2}{T} \mid E_0 \mid^2}{(\omega - \omega_0)^4 + [\frac{4}{T^2} - 2a^2](\omega - \omega_0)^2 + a^4} \tag{5.17}$$

It is clear that the spectrum will depend on the sign of $\lambda^2 = \frac{1}{T^2} - a^2$. We can obtain a singlet or a doublet for the electrical field spectrum. As exposed on figure 3.2 with increasing fluctuation time T (a=1, $\omega_0 = 0$) the central part of the power spectrum splits in two components located at frequencies $\omega = \omega_0 \pm [a^2 - (1/T^2)]^{1/2}$. The spectrum is a direct representation of the energy distribution of the system. For fast fluctuations the spectrum is narrowing around the system average frequency. But even in this case It is non lorentzian: The far wing of the power spectrum, given by eq. 5.17, falls of as $1/\omega^4$, faster than the lorentzian.

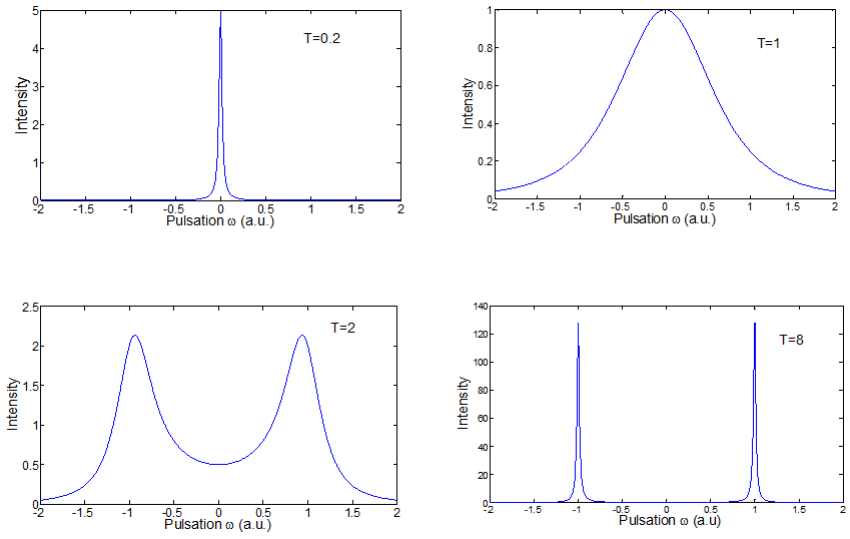

Figure 5.10: Intensity Spectra calculated for a dipole fluctuating as a telegraph random process, for 4 different average fluctuation times: T=0.2, T=1, T=2,T=8.

It is easier to understand it by writing the relaxation function $\mid \phi(\tau) \mid$ for the two extreme cases ($\alpha T \ll 1$ and $\alpha T \gg 1$).

In the case of very slow fluctuations ($aT \gg 1$),

$$\mid \phi(\tau) \mid = exp(-\frac{\mid \tau \mid}{T})cos(\alpha\tau)$$

In the limit of a infinitely large time T for a jump to occur, the system fluctuates between the 2 states corresponding to the TLS energy states distribution. The spectrum corresponding to such a relaxation function is an exact description of this energy distribution (fig. 5.10) with lorentzian line centered around the 2 energies of the TLS.

In the opposite case, if $aT \ll 1$,

$$\phi(\tau) \backsimeq exp(-\frac{\alpha^2 T}{2} \mid \tau \mid)$$

This is a monotonous exponential decay. The system doesn't have time to make a cycle between the 2 TLS states as it was the case for the slow fluctuation regime and as shown on fig. 5.10, the energy of the system is averaged around its mean value. This is an elementary manifestation of the so called motionnal narrowing.

Pre-gaussian noise:

To generate a more complexe fluctuation process, Wodkiezicz et al. [101] proposed to superpose N TLS. In this section we will calculate the associated relaxation function and see what approximation is used to complete the calculation. For very large N, the limit of this process is a gaussian-process named Kubo-Anderson process explained in the next section.

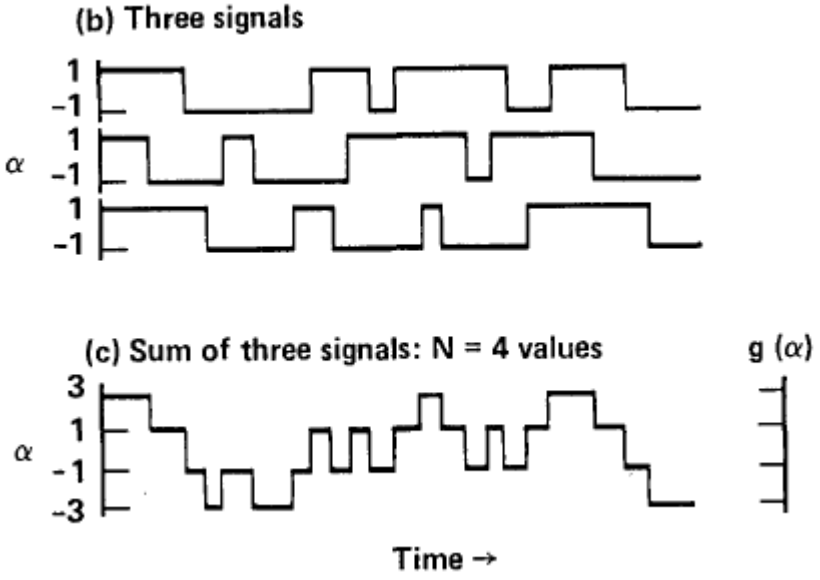

Figure 5.11: pregaussian noise

Processus construction: We consider N identical and uncorrelated TLS contributing to the generation of the pre-gaussian noise. An exemple is schematized on fig. 5.11 for N=3. The frequency is described by the following expression:

$$\omega(t) = \omega_0 + \delta\omega(t)$$

$$\delta\omega(t) = \sum_{i=1;N} \delta\omega_i(t) \tag{5.18}$$

$\delta\omega_i(t)$ is the fluctuating part of the i^{th} frequency TLS, evolving between +a and -a.

Relaxation function: Let us remind the relaxation function expression:

$$\phi_N(\tau) = \langle exp(i \int_0^\tau \delta\omega(t)dt)\rangle_T.$$

Introducing in this expression eq. 5.18:

$$\phi_N(\tau) = \langle exp(i \int_0^\tau \sum_{i=1,N} \delta\omega_i(t))dt >_T = \langle \prod_{i=1,N} exp(i \int_0^\tau \delta\omega_i(t))dt\rangle_T. \tag{5.19}$$

During the construction of this pre gaussian process we made the assumption that the N TLS were uncorrelated. Hence we are allowed to write:

$$\langle \prod_{i=1,N} exp(i \int_0^\tau \delta\omega_i(t))dt >_T = \prod_{i=1,N} \langle exp(i \int_0^\tau \delta\omega(t))\rangle dt$$

As a result, the relaxation function of a dipole in interaction with N uncorrelated TLS is the product of the N relaxation functions calculated for a single TLS.

In the case of N identical TLS we can write:

$$\phi_N(\tau) = [\frac{1}{2}(\frac{1}{T\lambda} + 1)exp(-(\frac{1}{T} - \lambda) \mid \tau \mid) - \frac{1}{2}(\frac{1}{T\lambda} - 1)exp(-(\frac{1}{T} + \lambda) \mid \tau \mid)]^N \tag{5.20}$$

Large N limit: Wodkiewicz et al. name this total process a "pre-gaussian noise"[101]. Indeed, they show in the same paper that in the limit where $N \to \infty$, the described process tends towards a Gaussian stochastic process and the variable $\delta\omega(t)$ follows a gaussian distribution. This is a consequence of the central limit theorem wich asserts that a sufficently large number of independant random variables will be approximately normally distributed.

5.2.3 Kubo-Anderson model

Kubo and Anderson used a gaussian fluctuation process to explain RMN spectra fluctuation due to nuclear spin fluctuations [73]. As for previous models we will calculate its relaxation function and deduce the intensity spectrum associated for such a process under extreme limit conditions.

Relaxation function:

We now consider a Gaussian process, described by a variable $\delta\omega(t)$ defined by its standard deviation Σ_s and its correlation time τ_c such as:

$$\langle \delta\omega(t)\delta\omega(0)\rangle = \Sigma_s^2 exp(\frac{t}{\tau_c}) \tag{5.21}$$

The relaxation function can be decomposed with the cumulant methods as follows:

$$\phi(\tau) = exp[-i \int_0^\tau dt\langle \delta\omega(t)\rangle + \frac{i^2}{2!} \int_0^\tau dt \int_0^\tau dt' \langle \delta\omega(t)\delta\omega(t')\rangle + ...] \tag{5.22}$$

In this expression the second order term only is non-zero:
-as $\langle\delta\omega(t)\rangle = 0$, the first term is equal to zero.
- as $\delta\omega(t)$ is a gaussian process, moments of orders greater than 2 are zero[103].
As a result the only remaining term is the second one:

$$\phi(\tau) = exp[-\frac{1}{2}\int_0^\tau dt \int_0^\tau dt^{'} \langle\delta\omega(t)\delta\omega(t^{'})\rangle]$$

$$= exp[-\int_0^\tau dt(\tau - t)\langle\delta\omega(\tau)\delta(0)\rangle] \tag{5.23}$$

We introduce eq. (2.21) in eq. (2.23):

$$\phi(\tau) = exp[-\int_0^\tau dt(\tau - t)\Sigma^2 exp(-\frac{\mid t \mid}{\tau_c})]$$

$$\phi(\tau) = exp[-\Sigma^2\tau_c^2(exp(-\frac{\mid \tau \mid}{\tau_c}) + \frac{\mid \tau \mid}{\tau_c} - 1)] \tag{5.24}$$

Fast and slow fluctuation regimes: conditions for the motional narrowing

Slow fluctuation regime: For $\Sigma\tau_c \gg 1$, the system is in the "slow fluctuation regime", its relaxation function regime can be approximated by:

$$\phi(\tau) = exp(-\frac{1}{2}\Sigma_s^2\tau^2)$$

The intensity spectrum corresponding to this relaxation function is the inverse fourier transform of $\phi(\tau)$ (section 2.1.2):

$$S(\omega) = exp(-\frac{(\omega - \omega_0)^2}{2\Sigma_s^2})$$

This is a gaussian profile spectrum, with a linewidth equal to: $\Gamma_s = 2\hbar\sqrt{2ln2\Sigma_s}$.

In the slow fluctuation regime, the spectrum is representative of the gaussian frequency distribution of the fluctuations.

Fast fluctuation regime: For $\Sigma\tau_c \ll 1$, the system is in the "fast fluctuation regime", its relaxation function regime can be approximated by:

$$\phi(\tau) = exp(-\Sigma^2\tau_c \mid \tau \mid)$$

The inverse fourier-transformation of this exponential relaxation function leads to a Lorentzian profile intensity spectrum:

$$S(\omega) = \frac{1}{(\omega - \omega_0)^2 + \Sigma_s^2\tau_c}$$

Its linewidth is: $\Gamma_f = 2\hbar\Sigma_s^2\tau_c$

When the rate of the fluctuations is increased the spectrum transits from a gaussian profile to a more narrow lorentzian lineshape. As for the simple example of the single telegraph noise (section 2.2.1), when the frequency fluctuations gets faster, the spectrum is narrowing around its average frequency. This phenomenon is called "motional narrowing". This phenomenon was observed on InAs/GaAs quantum dots and explained by A. berthelot et. al[104, 105] with the

help of the Kubo Anderson model. The originality was that the transition from the slow to the fast fluctuation regime occured when temperature or the excitation power was lowered. This is quite counter-intuitive as fluctuations tend to be slower when those 2 parameters decrease. This "unconventionnal" behaviour is due to a very important assymetry between the capture and the escape rates. In the next section, we explain how the Kubo model has been adapted to non symetrical fluctuation processes.

Generalization of the Kubo-Anderson model to non symetrical fluctuations.

Correlation time and intensity variance: R.J Cook et al. [106]calculated the correlation function corresponding to a 3 level system (fig. 5.12 a)). It includes 2 excited states: a low radiative rate level "weak" (1 photon per second for example), and a high radiative rate (10^8photons per second for exemple) level "Strong". These two levels are linked by a ground state. The result is a blinking system wich is behaving as a telegraph noise signal. The difference here is that, as the strong level is very fast-decaying the system jumps much faster in the weak level than the opposite. The fluctuations are non symmetrical.

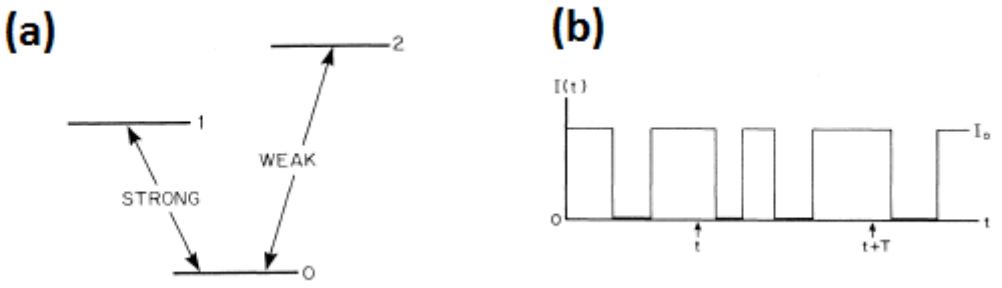

Figure 5.12: (a) 3 level system considered by R.J. Cook. Levels 1 and 2 are linked to the ground state 0 through a strong and weak transition respectively. (b) Fluorescent Intensity versus time. Interruptions of fluorescence are due to excitation of the weak transition $0 \rightarrow 2$.

They show that we can consider this 3 level system as an effective 2 level system. The upper level is (0+1) and the lower level is 2. These two levels are linked by an upward transition rate $R_+$and a downward rate R_-such as :

$$P_+ = P_2, \qquad P_- = P_0 + P_1 \tag{5.25}$$

which are the probabilities that the weak transition is excited or not excited respectively.

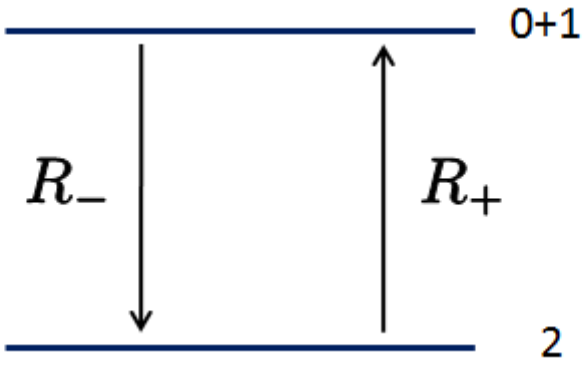

Figure 5.13: Effective 2 level system

They derived the second order correlation function, which is on the form [106]:

$$\Gamma(\tau) = \langle I(t)I(t+\tau)\rangle = M_I^2 + \sigma_I^2 e^{-(R_+ + R_-)\tau}$$

$M_I = \langle I\rangle = I_0 \frac{R_-}{R_+ + R_-}$is the mean value of the intensity and $\sigma_I^2 = \langle I^2\rangle - \langle I\rangle^2 = I_0^2 \frac{R_+ R_-}{(R_+ + R_-)^2}$ is the variance of the intensity.

It is also clear here that the correlation time is such as:

$$\frac{1}{\tau_c} = R_+ + R_-$$

Application to a quantum dot environnement: In section 1, we explained how the Stark shift of the exciton transition in an epitaxied quantum dot is caused by the captures and escapes of a free carrier in defects in the vicinity of the quantum dot. Those two processes, causing the energy fluctuation of the exciton, usually have different characteristic times ($\tau_\uparrow$ for the escape, $\tau_\downarrow$ for the capture).

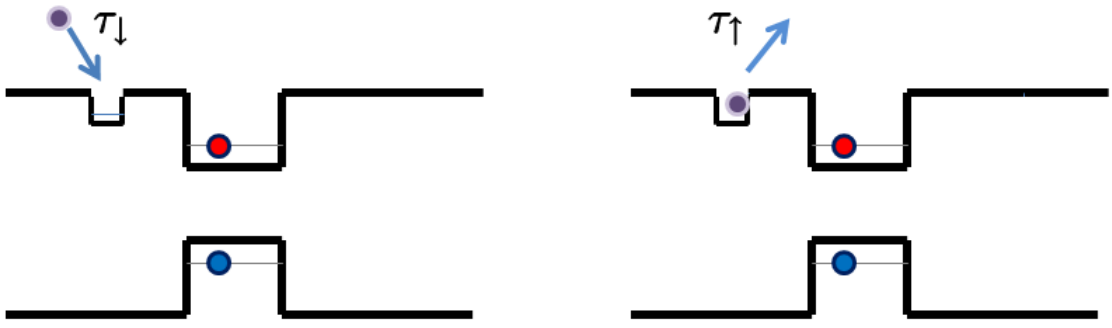

Figure 5.14: Capture and escape of a carrier near the quantum dot.

If we consider the presence of a single defect around the quantum dot, and that the presence of a charge in this defect is stark-shifting the transition of an energy Δ, we can approximate the charge-escape process of this charge with the non symmetrical random telegraph noise described by R.J. Cook et al. :

$$I_0 = \Delta.$$

$$\frac{1}{\tau_c} = \frac{1}{\tau_\downarrow} + \frac{1}{\tau_\uparrow}.$$

$$\sigma_I^2 = \Delta^2 \frac{1}{\tau_\uparrow \tau_\downarrow} / (\frac{1}{\tau_\uparrow} + \frac{1}{\tau_\downarrow})^2$$

Considering N uncorrelated and identical traps as we did for the transition from the single telegraph noise to the Pre-gaussian noise, the total variance of the fluctating system is:

$$\sigma_{Tot}^2 = \sum_{i=1,N} \sigma_i^2 = N\sigma_I^2$$

with σ_i the energy variance of the i^{th} trap. We can now deduce the standard deviation of the fluctuations $\sum_s$:

$$\Sigma_s = \sqrt{\sigma_{Tot}^2}/\hbar = \frac{\sqrt{N}\Delta}{\hbar(\sqrt{\frac{\tau_\downarrow}{\tau\uparrow}} + \sqrt{\frac{\tau\uparrow}{\tau_\downarrow}})}$$

The amplitude of the fluctuations depends on the number of traps around the quantum dot and on the ratio between the escape and the capture times. It reaches its maximum when the fluctuations are symetrical ($\tau_\downarrow = \tau_\uparrow$), $\Sigma_{s_{max}=} \frac{\sqrt{N}\Delta}{2\hbar}$, corresponding to the standard deviation given by the Kubo anderson model.

In the following we will deal with the full width half maximum of the gaussian distribution of the fluctuations $\Sigma = 2\sqrt{2ln2}\Sigma_s$, and we will call this quantity the fluctuation amplitude.

This concept of symmetrical fluctuation will be crucial in the understanding of experimental results presented in section 5. If we plot the amplitude versus the ratio of the escape and capture times $\frac{\tau_\downarrow}{\tau\uparrow}$ (fig. 5.15), we can notice that it is increasing as the ratio tends to 1, i.e. the fluctuations get more and more symmetrical. This is also quickly saturating around it's maximum value, which means that if the system is almost symetrical, a small variation of this ratio won't affect much the amplitude.

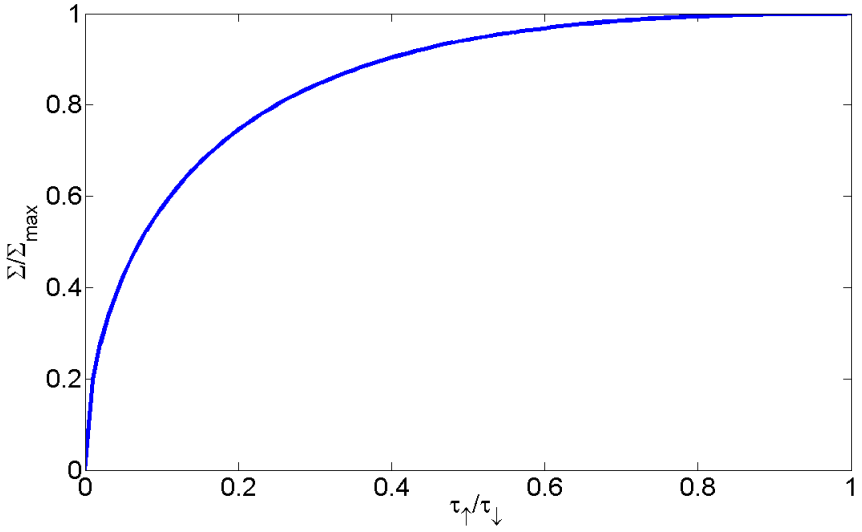

Figure 5.15: Fluctuation amplitude versus ratio between capture and escape rates

5.3 Correlation time measurement via photon counting.

To fully describe the spectral diffusion phenomen on a single object, one need to know 3 parameters: the correlation time of the fluctuations τ_c, the amplitude of the fluctuations Σ and the homogeneous linewidth σ of the transition. In this section, we will be interested in the measure of τ_c. In his thesis, Gregory Sallen developped a photon correlation method able to easily mesure this quantity[114]. Before briefly describing this technique, we make a short summary of the already existing techniques in order to compare their precision.

5.3.1 Other methods and time resolutions:

Photoluminescence spectroscopy

The first and simplest way to mesure the correlation time of the line spectral jumps is to collect and accumulate spectra on a timescale as short as possible.This way one can probe the different line positions between the successive integrations. Using a CCD camera, one can acquire a spectrum every 1 ms, which defines the time resolution of the method. This permitted to measure the first spectral diffusion characteristic times on quantum dots [75, 90].

Hole burning experiment

Spectral hole burning is the frequency selective bleaching of the absorption spectrum of a material, which leads to an increased transmission (a "spectral hole") at the selected frequency[108]. To observe such a phenomen, the spectrum needs to be inhomogeneously broadened as it is the case for dye molecules or an ensemble of quantum dots and the material must undergo, after light absorption (from the narrow band pump excitation) , a modification which changes its absorption spectrum probed by the large band laser. Such an absorption spectrum is plotted on fig. 5.16 a), it is called the spectral hole burning(SHB).

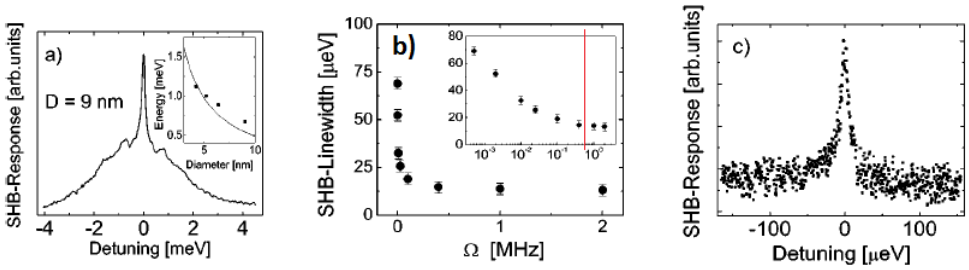

Figure 5.16: a)SHB-response versus detuning at a fixed frequency $\Omega = 20\,kHz$, b) SHB linewidth versus pump frequency. Inset plot in semi-log scale c) Expanded scan of the SHB-resonance.

We can extract from these datas the zero phonon line of a single transition and its corresponding phonon broadening. In this reference , Palinginis et al. modulate the pump intensity with a frequency Ω[109]. The SHB spectrum is strongly influenced by Ω. As shown in fig. 5.16 b), the SHB linewidth decreases with Ω. In the limit that the modulation period is long compared with the time scale at which the spectral diffusion takes place, spectral diffusion can lead to significant broadening of the SHB resonnance. The SHB linewidth obtained at modulation frequency of a few MHz approaches an assymptotic value, approaching the homogeneous linewidth. We can also estimate an order of magnitude of the correlation time of the spectral jumps (here $10^{-1}MHz$).

the precision of the measurement here is poor and the resolution is limited by the maximum intensity frequency of the pump.

This experiment is very well fitted to homogeneous linewidth measurements. On fig. 5.16, is plotted the SHB- response versus the detuning. We have access to the zero phonon linewidth (around $6\mu eV$) and also to the phonon coupling absorption spectrum.

This method, despite not being a time resolved experiment allows to have an order of magnitude of the correlation time and is the most precise method for homogeneous zero phonon linewidth evauation.

Fluctuating excitation wavelength time correlation:

This is a relatively old technique (1998)[110], which doesn't require any single photon counting system or APD. One need to be in a two photons excitation configuration, (excitation wavelength twice larger than the transition wavelength). Instead of recording one spectrum with an accumulation time long enough to have the required signal/noise ratio, N very fast laser frequancy scans over the same spectral region are acquired. Each of them is a SM spectrum with a high time reslution but very small signal/noise ratio. To keep this high time resolution and to improve the signal to noise, autocorrelation function (ACF's) are calculated for each scan, and then these functions are averaged:

$$\langle ACF(\omega')\rangle = \frac{1}{N}\sum_{k=1}^{N}\int_{-\omega_0/2}^{\omega_0/2} I_k(\omega)I_k(\omega+\omega')d\omega$$

where $I_k(\omega)$ is the kth single scan spectrum.

If ACF(ω') is significantly different from zero only for $0<\omega' < \omega'_{max} < \omega_0$, this indicates that a part of the scan interval $\omega_0$consists on no signal and can be narrowed without loosing the jumping object emission. Thus, ω'_{max}/r,where r is the scanning rate, can be defined as the time resolution.

In SM excitation spectra, $I_k$are proportional to the population of the excited state. This population is a solution of the optical Bloch equations when the molecular resonnance frequency ν and the laser frequency $\omega$are functions of time. $\omega(t) = -\omega_0/2 + rt$, with r the scan rate, and $\nu(t)$ is a stochastic function wich represents the random fluctuation of the molecular resonance. As the steady state population is a Lorentzian function of $\omega(t) - \nu(t)$,

$$\langle ACF(\omega')\rangle = \frac{1}{N}\int_{-\infty}^{\infty}\left\{[\omega-\nu(\frac{\omega}{r})]^2+\Gamma^2\right\}^{-1}\left\{[\omega+\omega'-\nu(\frac{\omega}{r})]^2+\Gamma^2\right\}d\omega$$

The total recording time is $N\omega_0/r$, and $\nu(t) = \sum_m \zeta_m(t)$ where $\zeta_m(t)$ are stochastic functions describing temporal frequency changes. Only $\zeta_m(t)$ with correlation times shorter than ω_0/r are significant.

An example of measurement with this technique is given on fig. 5.17. On part a) an integrated 2 photons excitation spectrum is plotted and on part b) The spectrum corresponding to a fast scan. In the inset where the corresponding ACF(ω) is plotted, they measure a correlation time contribution down to 40 ms, the temporal resolution of this method.

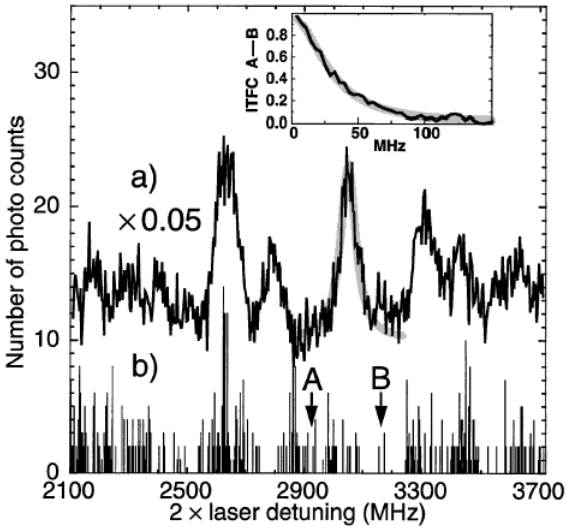

Figure 5.17: a) integrated TPE spectrum. b) one scan spectrum. A and B are the two extreme frequencies for the scan serie necessary for the ITFC integration. Inset: ITFC graph.

Photon-correlation Fourier spectroscopy

In order to avoid the limitations pointed out in the previous section about Standard Fourier spectroscopy, L. Coolen et al. developped a technique which is coupling to a Michelson interferometer experiment, a correlation setup able to convert spectral fluctuations into intensity fluctuations[113].

At the output of the two interferometer arms, two interference fringe patterns are obtained, troubled by the spectral diffusion. Thanks to the correlation setup, one can have a time resolved measurement of the spectral diffusion effect, as it will affect the correlation figure with respect to the delay between to photon detections. For large delays, the correlation figure will be more affected by the spectral diffusion than for small delays. A correlation time of the fluctuations can be extracted. L Coolen et al. measured a correlation time of 200 μs, achieving a maximum resolution of 20 μs, limited by the very sensitive stability of the experiment.

The fringe spectral spacing can be made infinitely small by increasing the optical path difference between the two arms, so that the resolution can be made arbitrarily small and exceed the homogeneous linewidth. When the fringe spectral periodicity becomes narrower than the homogeneous linewidth (ie. optical path difference is large), the intensity noise is no longer related to spectral diffusion. The authors take benefit from the infinitely high spectral resolution of interferometry technique. This way, they measured homogeneous linewidth of 6 μeV.

It is the ultimate method to fully characterize the spectral diffusion of a photon emitter, giving, in principle with the best resolution, all the characteristic parametters of the statistical distribution of the emission. However, this experiment is very difficult and demanding to be executed.

5.3.2 Experimental setup and technique:

Principle of the measurement.

As explained in Chapter 3, the object we are studying is emitting photons following a sub-poissonian statistic. In other terms, it is not emitting photons randomly but one by one. Under continuous excitation, the average emission rate of these single photons is Γ_{rad}, the radiative rate of the transition. If this emission rate is larger than the correlation rate of the spectral jumps, the photon statistic can be described as in plotted fig. 5.18 a). The right part of the line and photons emitted at an energy belonging to the right part are colored in blue. The left part of the line and photons emitted at an energy belonging to the left part are colored in red. The emitter has the time to send several photons in the right side before having its emission energy shifted to the left side by the spectral diffusion. If we now send these photons in a HBT setup, selecting spectrally the whole line, we perform a simple autocorrelation and observe the antibunching phenomen with a characteristic rate Γ_e.

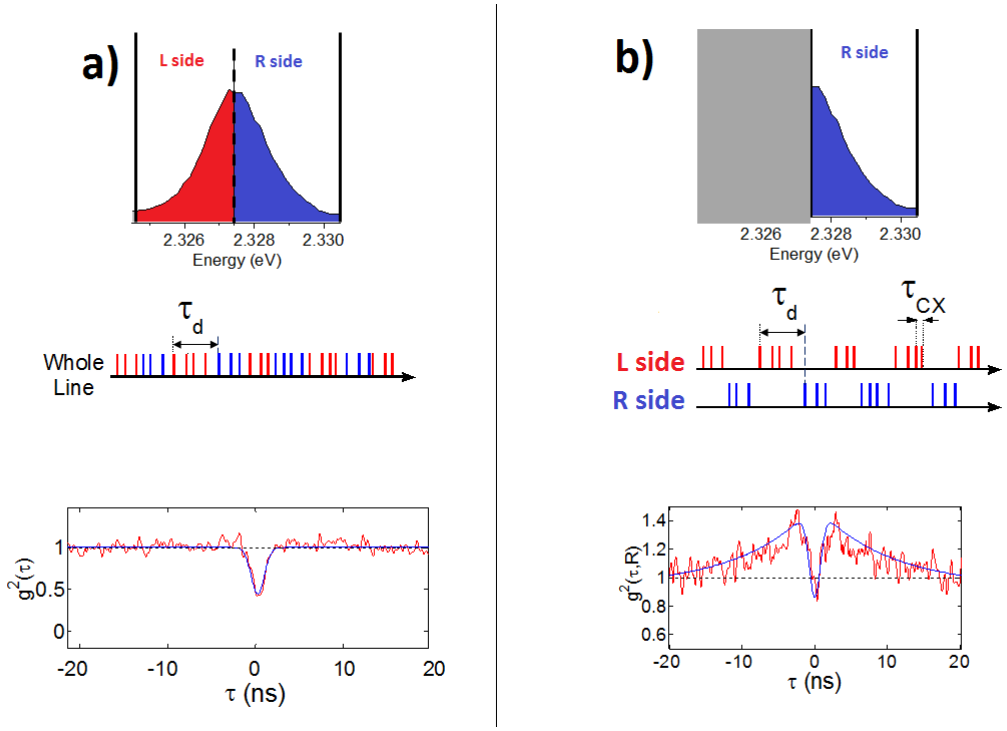

Figure 5.18: a) Autocorrelation of the whole line: spectrum, photon statistic and autocorrelation function. b)Autocorrelation of the right half-line: spectrum, photon statistic and autocorrelation function

We now select spectrally the right part of the line (see figure 3.3 b)) and perform the auto-correlation of the right side. The selected photons are now only detected when the homogeneous line is in the right part. After a time τ_c, the line gets out of the selected spectral zone and no photon is measured. The resulting emission is no longer a simple sub-poissonian source (it is represented in blue on fig. 5.18 b)). Photons are now detected by "bunches" and the result on the autocorrelation function of such a source at zero delay is a $g^2(\tau_c > \tau > \tau_{rad}) > 1$ as plotted on fig. 5.18 b). We already observed in chapter 2 such "bunching effect" in the cross correlation experiment on the exciton and the biexciton or on charged exciton and charged biexciton, 2 pairs

of transitions linked by a radiative cascade.

We can understand here such a "bunching effect" simply as follow: When the first photon hits one of the APD and gives the start, the line is in the right part of the line. There is more probability for the line to emit again a photon in the right side than at any random time and to give the stop. As a result there are more events measured on a short delay than for an infinite delay where detections of the start and stop photons are uncorrelated. After a longer delay, the $g^2(\tau)$ decreases exponentially with a characteristic time τ_c. The probability for the line to stay in the right side is getting lower for longer delays because it has more time to jump in the left side . The time τ_c measured can be considered as the time it needs to leave the right side.

Modelisation for an infinitely sharp homogeneous linewidth:

G. Sallen et. al. showed that we can model this mesurement and extract from it the correlation time of the fluctuations by a simple rate equation.[114]

It can be represented by a two-level system splitted in two parts (Right and Left) corresponding to the presence of the line in the left or right part of the inhomogeneous energy distribution. The system is pumped from the ground state (0) to the excited state (1), with a pump rate r, and can relax from the excited state to the ground state with a radiative rate γ. The line can also transit from the Left side (L) to the right side (R) with a rate γ_R and back with a rate γ_L. (fig. 5.19).

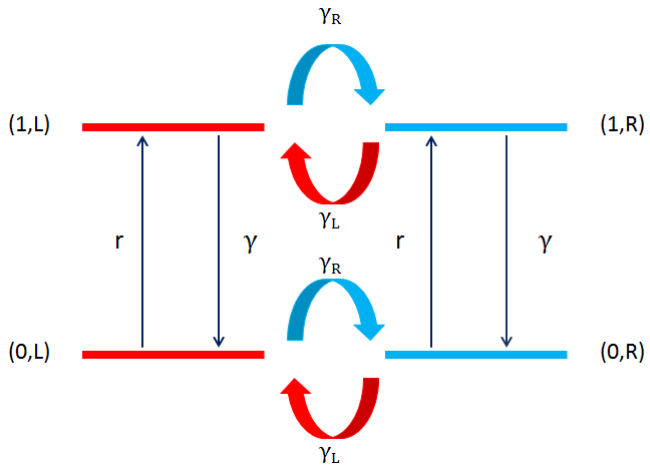

Figure 5.19: Splitted two-level system describing the spectral diffusion for an infinitely sharp homogeneous line transiting in the right and left side of the inhomogeneous energy distribution under countinuos excitation.

We can now derive the population of each state with the following set of rate equations [115]:

$$\frac{dn_{0L}}{dt} = -rn_{0L} - \gamma_R n_{0L} + \gamma n_{1L} + \gamma_L n_{0R} \tag{5.26}$$

$$\frac{dn_{1L}}{dt} = -\gamma n_{1L} - \gamma_R n_{1L} + rn_{0L} + \gamma_L n_{1R} \tag{5.27}$$

$$\frac{dn_{0R}}{dt} = -rn_{0R} - \gamma_R n_{0L} + \gamma n_{1R} + \gamma_R n_{0L} \tag{5.28}$$

$$\frac{dn_{1R}}{dt} = -\gamma n_{1R} - \gamma_L n_{1R} + r n_{0R} + \gamma_R n_{1L} \tag{5.29}$$

n_{0L}, n_{1L}, n_{0R}, n_{1R} are the population of the (0, L), (1, L), (0, R), (1, R) states respectively. We define $N_0 = \sum_i n_{oi}$ and $N_1 = \sum_i n_{1i}$, with $i = R, L$ and $N_0 + N_1 = 1$.
We also define

$$\gamma_c = \gamma_R + \gamma_L \tag{5.30}$$

From the previous set of equations we obtain:

$$\frac{dN_1(t)}{dt} = -\gamma N_1 + r N_0 \tag{5.31}$$

the solution of this differential equation is:

$$N_1(t) = \frac{r}{r+\gamma} + Cexp(-(r+\gamma)t) \tag{5.32}$$

with C a constant depending on the initial conditions.

We can do the same for the total population of one side i of the line: $N_i = n_{0i} + n_{1i}$, i=R,L. We have

$$\frac{dN_i(t)}{dt} = \frac{\gamma_i}{\gamma_c} + Kexp(-\gamma_c t) \tag{5.33}$$

K is a constant depending on the initial conditions. We also note that the population decay only depends on the γ_c parameter, it is the correlation rate.

The general solutions of the set of 4 equations presented above are such as:

$$n_{0i}(t) = N_0(t) N_i(t) \tag{5.34}$$

$$n_{1i}(t) = N_1(t) N_i(t) \tag{5.35}$$

In the experimental configuration we choose (ie. the autocorrelation of the right side of the line), the start photon is sent from the right side. So the system is in the (0,R) state at t=0: $n_{0R}(0) = 1$, and we considere the probability to detect an other photon comming from the same right side after a delay τ. This correspond to the following autocorrelation function $g^2(R, R, \tau) = \frac{n_{1R}(\tau)}{n_{1R}(\infty)}$.

Using the previous equations we find:

$$g^{(2)}(R, R, \tau) = [1 + (\frac{\gamma_c}{\gamma_R} - 1)exp(-\gamma_c \tau)][1 - exp(-(r+\gamma)\tau)]. \tag{5.36}$$

$\gamma_R(\gamma_L)$ can be seen as the probability for the line to jump from the left (right) side towards the right (left) side. As γ_c is the sum of those 2 probabilities, it is just the probability for the line to jump. As a result, this experiment gives a direct mesurement of the correlation time. This allowed the mesurement of the first nanosecond- scale correlation time on a fluctuating system[114].

It is also clear that the γ_R and γ_L rates depend on the right and left areas relative sizes as there is more probability for the line to jump in a large area than in a small one. We are here placed in the particular situation where we perform the autocorrelation of one half of the total

line. As a result, there is as much probability for the homogeneous line to jump in the right side than in the left side and we have:

$$\gamma_R = \gamma_L \tag{5.37}$$

$$\gamma_R = \frac{\gamma_c}{2} \tag{5.38}$$

The autocorrelation function becomes:

$$g^2(R, R, \tau) = [1 + exp(-\gamma_c \tau)][1 - exp(-(r + \gamma)\tau)] \tag{5.39}$$

It is the product of 2 expressions. As $[1-exp(-(r+\gamma)\tau)]$ describes the single photon behaviour of the emitter, $[1 + exp(-\gamma_c \tau)]$ describes the spectral diffusion phenomenon and its influence on the ability of the emitter to send photons in the right spectral window. We can always express the autocorrelation function as a product of a energy position term and an emission term, if energy position and emission are two independant events (see annexe 1). An exemple is plotted on fig. 5.20 a). The theoretical curve calculated in eq. 5.39 is convoluted with the temporal resolution of the setup used for the mesurement. The fig. 5.20 b) shows the contribution of the spectral diffusion on the autocorrelation function. We can notice that for zero delay the value of this bunching is 2. This means that the line has a probability 1/2 to be in the right side. By reducing the detection zone for the autocorrelation we can increase the contrast of this bunching, as the less the line is present in the measured area, the larger is the zero delay value of the bunching. But it would also degrade the count rate on each APD, and impose a longer integration time. When we increase the detection area, we go towards the autocorrelation function of the whole line and the bunching is decreasing. Thus, the measurement is very sensitive to the area chosen for the detection. In order to collect photons comming exactly from the half line, the slit is open in such way that all photons from the line are counted by the detectors N. Then, the grating orientation is corrected in order to put half of the line out of the detection slit and collect exactly $\frac{N}{2}$ photons.

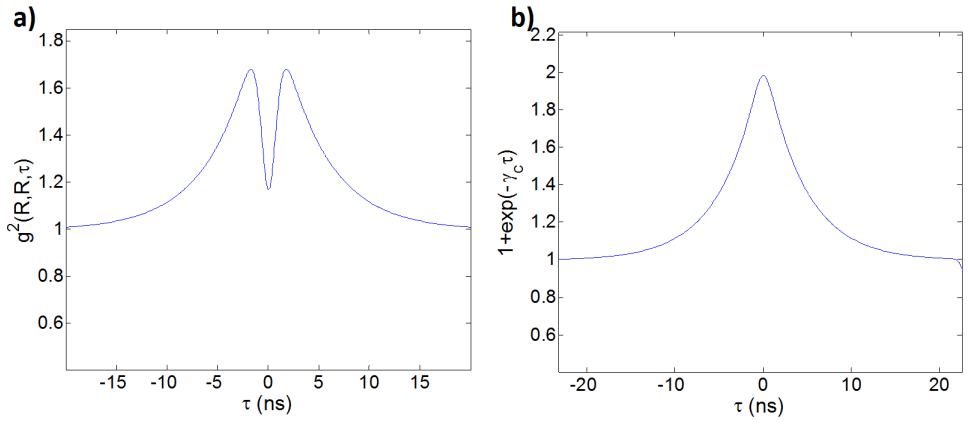

Figure 5.20: a) Theoretical half line autocorrelation function after convolution with the experimental temporal resolution. b) Contribution of the spectral diffusion to the autocorrelation function.

Experimental setup

The experimental apparatus is a HBT setup (see section 2.4 of chapter 1). We use 2 Perkin Elmer with 400 ps resolution APD's for photons detection. This leads for the whole experiment to 700 ps resolution. We choose this type of APD's here because the characteristic time of the phenomenon we want to observe is larger than the nanosecond and their quantum efficency is twice better than the faster APD's used for cross correlation or decay time experiments. This is particularly important as we collect photons only on half lines. A monochromator (about 300 μev resolution) is used for spectral selection of half line. Events are recorded on a HPCSPC counting card. The excitation laser is a continuous above ZnSe barrier 405 nm diode.

5.4 Mesurement of the homogeneous linewidth and fluctuation amplitude.

In the previous chapter, we explained how we can extract the correlation time from the half line autocorrelation measurement. We will show in this one how we can obtain informations about the homogeneous linewidth and the fluctuation amplitude, and obtain more information on the emission of a single nanowire quantum dot with this technique.

5.4.1 Separation of emission and energy position correlations

This aim of this subsection is the obtention of a preliminary result, which will simplfy the rather complex calculations leading to the derivation of the halfline autocorrelation function for a non infinitely sharp homogeneous linewidth.

We saw in the precedent example (section 3) that the autocorrelation function is the product of the spectral diffusion part (bringing information on the correlation of the homogeneous line energy) and the single photon part (bringing information on the correlation of the emission). We propose to show that this is a general result when emission and energy position of the line are independant, which is always the case for us.

Let's define the following ensembles:

-$\gamma(t)$: ensemble of events such as a photon is detected at time t.

- γ_{em}^{t}: ensemble of events such as a photon is emited by the two level system.

- γ_{in}^{t}: ensemble of events such as the two level system energy is in the right spectral window.

The emission of a photon by the TLS and its energy situated in the right spectral window are two independant events, so:

$$\rho(\gamma_{em}^{\tau} \cap \gamma_{in}^{\tau}) = \rho(\gamma_{em}^{\tau})\rho(\gamma_{in}^{\tau}) \tag{5.40}$$

We go back to the expression of autocorrelation function in term of probabilities:

$$g^2(\tau) = \frac{\rho(\gamma(\tau) \mid \gamma(0))}{\rho(\gamma(\tau))} \tag{5.41}$$

To detect a photon at time t, one need to have a photon emitted by the TLS at time t and to have the TLS energy in the right spectral window at time t:

$$\gamma(t) = \gamma_{em}^{t} \cap \gamma_{in}^{t} \tag{5.42}$$

Therefore,

$$\rho(\gamma(\tau) \mid \gamma(0)) = \rho(\gamma_{em}^{\tau} \cap \gamma_{in}^{\tau} \mid \gamma_{em}^{0} \cap \gamma_{in}^{0}) \tag{5.43}$$

Using eq. 5.40 in eq. 5.43, we have:

$$\rho(\gamma(\tau) \mid \gamma(0)) = \rho(\gamma_{em}^{\tau} \mid \gamma_{em}^{0} \cap \gamma_{in}^{0})\rho(\gamma_{in}^{\tau} \mid \gamma_{em}^{0} \cap \gamma_{in}^{0}) = \rho(\gamma_{em}^{\tau} \mid \gamma_{em}^{0})\rho(\gamma_{in}^{\tau} \mid \gamma_{in}^{0}) \tag{5.44}$$

We can now find the expected general expression, separating the TLS emission and energy correlation functions in the autocorrelation function of the right side of the emission line.

$$g^2(\tau) = \frac{\rho(\gamma_{em}^{\tau} \mid \gamma_{em}^{0})}{\rho(\gamma_{em}^{\tau})} \frac{\rho(\gamma_{in}^{\tau} \mid \gamma_{in}^{0})}{\rho(\gamma_{in}^{\tau})} = g_{em}^2(\tau) g_{in}^2(\tau) \tag{5.45}$$

This result will make our future calculations of correlation functions easier, especially in the next section, as the emission part $g_{em}^2(\tau)$ will always be the same and we'll only have to focus on the derivation of $g_{in}^2(\tau)$, the second order correlation function of the TLS energy position.

5.4.2 Modelization for a finite homogeneous linewidth

Evidence of the finite linewidth

The expression of the autocorrelation function calculated in section 5.3.2 shows that the correlation rate has no influence on the bunching height and that it reaches the value of 2 for the autocorrelation of an half-line (fig. 5.20 b)). In simple words, one can say that the probability for the line to be in the right spectral window does not depend on its jumping speed. An exemple is plotted in fig. 5.21 a). In blue is plotted the theoretical function derived previously:

$$g^2(R, R, \tau) = [1 + exp(-\gamma_c \tau)][1 - exp(-(r + \gamma)\tau)] \tag{5.46}$$

We observe that we can't fit the experimental datas (in red) with this expression. The bunching is lower than expected if we consider the model of an infinitely sharp line moving from one side to the other. In order to fit correclty the datas, we introduce an independant parameter β in the bunching part of the expression such as:

$$g^2(R, R, \tau) = [1 + \beta exp(-\gamma_c \tau)][1 - exp(-(r + \gamma)\tau] \tag{5.47}$$

The result of this new fit is plotted on figure 3.7 b) with a parameter $\beta = 0.5$, meaning that the value at zero delay of the bunching plotted for the infinitely sharp homogeneous line model (fig 3.6 b) is not longer 2, but 1.5. Two independant parameters are now ruling the characterization of spectral diffusion, the correlation rate γ_c and the 'bunching height' β.

We can conclude that the model we presented in section 5.3.2 does not fully describe the reality. In order to explain the origin of the parameter β, and to understand which other quantities are influent in this measurement, we need to produce a model considering a finite linewidth for the homogeneous line.

Consequences of a finite linewidth on photon statistic.

We now consider that the line fluctuating from one spectral window to the other is no longer infinitely sharp. The center of this line can be in the left side, but the corresponding photon detected can come from the right one, and vice versa. This behaviour is represented in fig. 5.22.

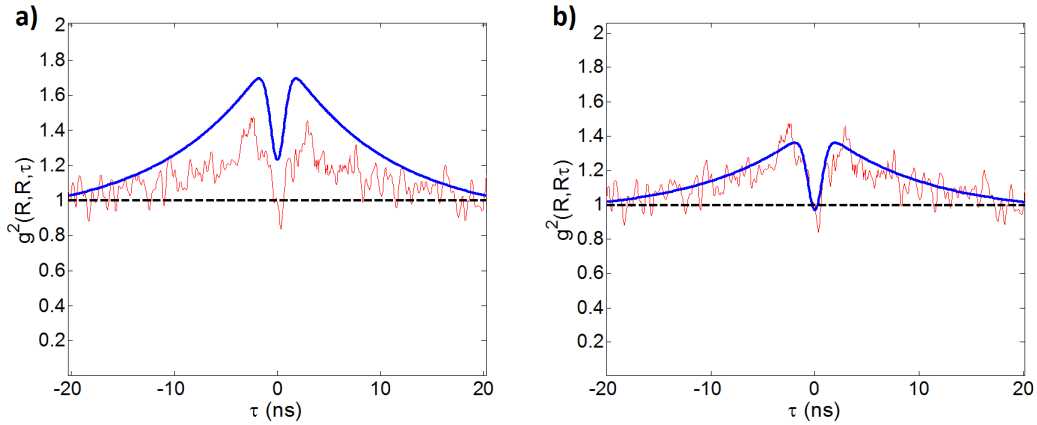

Figure 5.21: a) Autocorrelation of the half-line. The theoretical curve calculated with the infinitely sharp homogeneous line model is plotted in blue, experimental datas in red. b) Theoretical curve corrected with the parameter $\beta = 0.5$.

Whereas in the first case, the spectral windows where photons are emitted is the same as the position of the line, in the second case, it's no longer true. The direct consequence is a relative loss of the characteristic "photons bunching" emission for a more "poissonian type" emission. This is a way to explain the weakness of the measured bunching. In fact, to the bunching statistic we could derive from the rate equations of section 5.3.2, we have to superpose a random uncorrelated emission statistic introduced by the finite linewidth of the emitter.

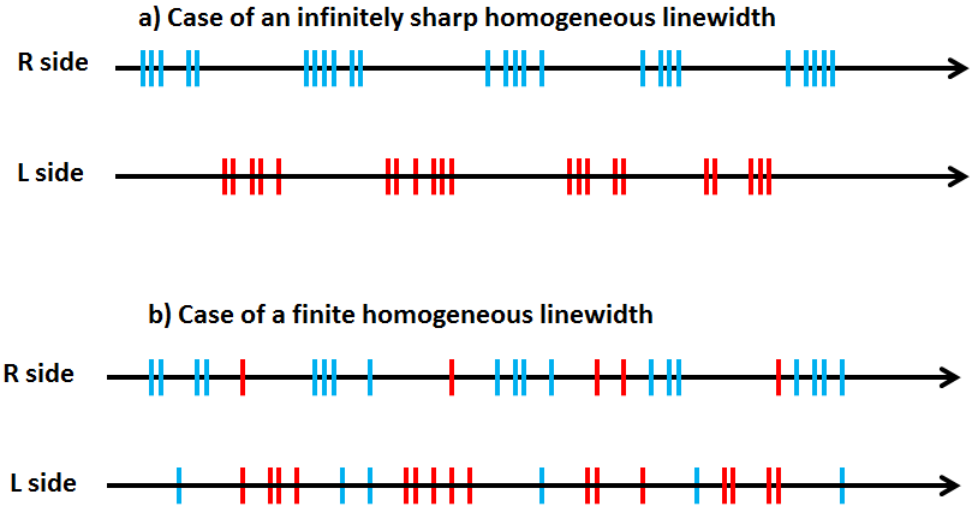

Figure 5.22: a) Photon statistic of the emitter in the case of an infinitely sharp homogeneous line. Blue (red) dots represent photons emitted in the right (left) spectral window. b) Photon statistic of the emitter in the case of a finite homogeneous linewidth. Blue (red) dots represent photons emitted when the center of the homogeneous line is in the right (left) spectral window

Finite homogeneous linewidth model

In the previous infinitely sharp model we define a model where a two-level system can be in the right or in the left window. The situation is now more complicated, as the TLS energy fluctuates from the right side to the other with a correlated statistic, but can also be randomly, and with no time correlation, distributed in energy along the lorentzian profile imposed by the homogeneous linewidth.

The total energy $E^t$of the TLS at time t is the sum of two random variables:

$$E^t = \mu^t + \varepsilon^t \tag{5.48}$$

where μ^t is the energy position of the center of the homogeneous linewidth at time t. It is distributed along the gaussian distribution of the fluctuations. This energy is time correlated. This means that the value of the random variable at time $t+\tau$ is influenced by its position at time t and :

$$\langle \mu^t \mu^{t+\tau} \rangle \neq \langle \mu^t \rangle \langle \mu^{t+\tau} \rangle \tag{5.49}$$

ε^t is the energy shift due to the homogeneous linewidth at time t. we assume it has a lorentzian distribution centered on μ^t. This variable is described by a poissonian process and is not time correlated.

$$\langle \varepsilon^t \varepsilon^{t+\tau} \rangle = \langle \varepsilon^t \rangle \langle \varepsilon^{t+\tau} \rangle = \langle \varepsilon^0 \rangle \langle \varepsilon^\tau \rangle = \langle \varepsilon^\tau \rangle^2 \tag{5.50}$$

The spectral window of detection is defined by the energy interval I_n. In the experimental configuration we consider, $I_n = [0, +\infty[$.

The energy of the TLS is in the right spectral window at time t when $E^t \epsilon I_n$, so when:

$$(\varepsilon^t + \mu^t)\epsilon I_n \tag{5.51}$$

If we define the ensemble γ^t_{in} as the ensemble of events such as the two level system energy is in the right spectral window, it corresponds to the ensemble of $\varepsilon^t$and μ^tsuch as $(\varepsilon^t + \mu^t)\epsilon I_n$:

$$\gamma^t_{in} \equiv \left\{(\varepsilon^t + \mu^t)\epsilon(I_n)\right\}$$
$$\gamma^0_{in} \equiv \left\{(\varepsilon^0 + \mu^0)\epsilon(I_n)\right\}$$

we also define the following ensembles :

-$\gamma(t)$: ensemble of events such as a photon is detected at time t.

- γ^t_{em}: ensemble of events such as a photon is emited by the two level system.

- γ^t_{in}: ensemble of events such as the two level system energy is in the right spectral window.

-μ^t_{in} : ensemble of μ such as $\mu^t \epsilon I_n$.

-μ^t_{out} : ensemble of μ such as $\mu^t \notin I_n$

We found out in the previous subsection that we can always write down the autocorrelation function as:

$$g^2(\tau) = g^2_{em}(\tau) g^2_{in}(\tau)$$

with $g^2_{in}(\tau) = \frac{\rho(\gamma^\tau_{in} | \gamma^0_{in})}{\rho(\gamma^\tau_{in})}$, the energy position part of the autocorrelation that we need to correct.

$$\rho(\gamma^\tau_{in} \mid \gamma^0_{in}) = \rho(\left\{(\varepsilon^t + \mu^t)\epsilon(I_n)\right\} \mid \gamma^0_{in}) \tag{5.52}$$

We use here the extended form of the Bayes theorem which asserts that for a ensemble A such as $A = \sum_i A_i$,

$$P(B) = \sum_i P(B \mid A_i)P(A_i)$$

so eq. 5.52 becomes:

$$\begin{aligned}\rho(\gamma_{in}^{\tau} \mid \gamma_{in}^{0}) = \rho(\{(\varepsilon^{\tau} + \mu^{\tau})\epsilon(I_n)\} \mid \mu_{in}^{\tau}) \mid \gamma_{in}^{0})\rho(\mu_{in}^{\tau} \mid \gamma_{in}^{0}) \\ + \rho(\{(\varepsilon^{\tau} + \mu^{\tau})\epsilon(I_n)\} \mid \mu_{out}^{\tau}) \mid \gamma_{in}^{0})\rho(\mu_{out}^{\tau} \mid \gamma_{in}^{0})\end{aligned} \tag{5.53}$$

$(\{(\varepsilon^{\tau} + \mu^{\tau})\epsilon(I_n)\} \mid \mu_{in}^{\tau})$, The ensemble of values taken by ε and μ such as $(\varepsilon+\mu)\epsilon(I_n)$ at time τ, knowing that $\mu\epsilon I_n$ at time τ is independant from the possible values taken by ε at time 0. Indeed, ε is a poissonnian random process. The condition on the μ value is already fixed at time τ in $(\{(\varepsilon^{\tau} + \mu^{\tau})\epsilon(I_n)\} \mid \mu_{in}^{\tau})$, a condition on its value at time 0 doesn't change the ensemble.

so we can conclude that the ensemble $(\{(\varepsilon^{\tau} + \mu^{\tau})\epsilon(I_n)\} \mid \mu_{in}^{\tau})$ and $\gamma_{in}^{0}$are independant ensembles, thus:

$$\rho((\{(\varepsilon^{\tau} + \mu^{\tau})\epsilon(I_n)\} \mid \mu_{in}^{\tau}) \mid \gamma_{in}^{0})\rho(\mu_{in}^{\tau} \mid \gamma_{in}^{0}) = \rho(\{(\varepsilon^{\tau} + \mu^{\tau})\epsilon(I_n)\} \mid \mu_{in}^{\tau})\rho(\mu_{in}^{\tau} \mid \gamma_{in}^{0}) \tag{5.54}$$

and

$$\rho(\gamma_{in}^{\tau} \mid \gamma_{in}^{0}) = \rho(\{(\varepsilon^{\tau} + \mu^{\tau})\epsilon(I_n)\} \mid \mu_{in}^{\tau})\rho(\mu_{in}^{\tau} \mid \gamma_{in}^{0}) + \rho(\{(\varepsilon^{\tau} + \mu^{\tau})\epsilon(I_n)\} \mid \mu_{out}^{\tau})\rho(\mu_{out}^{\tau} \mid \gamma_{in}^{0})$$

For any ensembles A and B, one have the basic relationship:

$$P(A \mid B) = P(B \mid A)\frac{P(A)}{P(B)}$$

so eq. 5.54 becomes:

$$\rho(\gamma_{in}^{\tau} \mid \gamma_{in}^{0}) = \rho(\{(\varepsilon^{\tau} + \mu^{\tau})\epsilon(I_n)\} \mid \mu_{in}^{\tau})\rho(\gamma_{in}^{0} \mid \mu_{in}^{\tau})\frac{\rho(\mu_{in}^{\tau})}{\rho(\gamma_{in}^{0})} + \rho(\{(\varepsilon^{\tau} + \mu^{\tau})\epsilon(I_n)\} \mid \mu_{out}^{\tau})\rho(\gamma_{in}^{0} \mid \mu_{out}^{\tau})\frac{\rho(\mu_{out}^{\tau})}{\rho(\gamma_{in}^{0})} \tag{5.55}$$

We apply again the Bayes Theorem on the probabilities $\rho(\gamma_{in}^{0} \mid \mu_{in}^{\tau})$ and $\rho(\gamma_{in}^{0} \mid \mu_{out}^{\tau})$.

$$\begin{aligned}\rho(\gamma_{in}^{0} \mid \mu_{in}^{\tau}) &= \rho((\gamma_{in}^{0} \mid \mu_{in}^{0}) \mid \mu_{in}^{\tau})\rho(\mu_{in}^{0} \mid \mu_{in}^{\tau}) + \rho((\gamma_{in}^{0} \mid \mu_{out}^{0}) \mid \mu_{in}^{\tau})\rho(\mu_{out}^{0} \mid \mu_{in}^{\tau}) \\ &= \rho(\gamma_{in}^{0} \mid \mu_{in}^{0})\rho(\mu_{in}^{0} \mid \mu_{in}^{\tau}) + \rho(\gamma_{in}^{0} \mid \mu_{out}^{0})\rho(\mu_{out}^{0} \mid \mu_{in}^{\tau}) \\ &= \rho(\gamma_{in}^{0} \mid \mu_{in}^{0})\rho(\mu_{in}^{\tau} \mid \mu_{in}^{0})\frac{\rho(\mu_{in}^{0})}{\rho(\mu_{in}^{\tau})} + \rho(\gamma_{in}^{0} \mid \mu_{out}^{0})\rho(\mu_{in}^{\tau} \mid \mu_{out}^{0})\frac{\rho(\mu_{out}^{0})}{\rho(\mu_{in}^{\tau})}\end{aligned} \tag{5.56}$$

The same way,

$$\rho(\gamma_{in}^{0} \mid \mu_{out}^{\tau}) = \rho(\gamma_{in}^{0} \mid \mu_{in}^{0})\rho(\mu_{out}^{\tau} \mid \mu_{in}^{0})\frac{\rho(\mu_{in}^{0})}{\rho(\mu_{out}^{\tau})} + \rho(\gamma_{in}^{0} \mid \mu_{out}^{0})\rho(\mu_{out}^{\tau} \mid \mu_{out}^{0})\frac{\rho(\mu_{out}^{0})}{\rho(\mu_{out}^{\tau})} \tag{5.57}$$

we inject the two last equations in eq. 5.55:

$$\begin{aligned}\rho(\gamma_{in}^{\tau} \mid \gamma_{in}^{0}) = {} & \rho(\gamma_{in}^{\tau} \mid \mu_{in}^{\tau})\rho(\gamma_{in}^{0} \mid \mu_{in}^{0})\rho(\mu_{in}^{\tau} \mid \mu_{in}^{0})\frac{\rho(\mu_{in}^{0})}{\rho(\gamma_{in}^{0})} \\ & + \rho(\gamma_{in}^{\tau} \mid \mu_{in}^{\tau})\rho(\gamma_{in}^{0} \mid \mu_{out}^{0})\rho(\mu_{in}^{\tau} \mid \mu_{out}^{0})\frac{\rho(\mu_{out}^{0})}{\rho(\gamma_{in}^{0})} \\ & + \rho(\gamma_{in}^{\tau} \mid \mu_{out}^{\tau})\rho(\gamma_{in}^{0} \mid \mu_{in}^{0})\rho(\mu_{out}^{\tau} \mid \mu_{in}^{0})\frac{\rho(\mu_{in}^{0})}{\rho(\gamma_{in}^{0})} \\ & + \rho(\gamma_{in}^{\tau} \mid \mu_{out}^{\tau})\rho(\gamma_{in}^{0} \mid \mu_{out}^{0})\rho(\mu_{out}^{\tau} \mid \mu_{out}^{0})\frac{\rho(\mu_{out}^{0})}{\rho(\gamma_{in}^{0})}\end{aligned} \tag{5.58}$$

For this experiment, $\rho(\mu_{in}^{0})$, $\rho(\mu_{out}^{0})$and $\rho(\gamma_{in}^{0})$ are respectively the probability to have $\mu \epsilon I_n$, $\mu \notin I_n$, and $\{(\varepsilon^{\tau} + \mu^{\tau})\epsilon(I_n)\}$ at any time. Thus:

$$\rho(\mu_{in}^{0}) = \rho(\mu_{out}^{0}) = \rho(\gamma_{in}^{0}) = \frac{1}{2}$$

and eq. 5.58 becomes

$$\begin{aligned}\rho(\gamma_{in}^{\tau} \mid \gamma_{in}^{0}) = {} & \rho(\gamma_{in}^{\tau} \mid \mu_{in}^{\tau})\rho(\gamma_{in}^{0} \mid \mu_{in}^{0})\rho(\mu_{in}^{\tau} \mid \mu_{in}^{0}) \\ & + \rho(\gamma_{in}^{\tau} \mid \mu_{in}^{\tau})\rho(\gamma_{in}^{0} \mid \mu_{out}^{0})\rho(\mu_{in}^{\tau} \mid \mu_{out}^{0}) \\ & + \rho(\gamma_{in}^{\tau} \mid \mu_{out}^{\tau})\rho(\gamma_{in}^{0} \mid \mu_{in}^{0})\rho(\mu_{out}^{\tau} \mid \mu_{in}^{0}) \\ & + \rho(\gamma_{in}^{\tau} \mid \mu_{out}^{\tau})\rho(\gamma_{in}^{0} \mid \mu_{out}^{0})\rho(\mu_{out}^{\tau} \mid \mu_{out}^{0})\end{aligned} \tag{5.59}$$

The probability for the TLS to be in a the right spectral window, knowing that it was at t=0, is the sum of 4 probabilities, describing the 4 configurations possible for this event:

-For the first term, the homogeneous line is in the spectral window at t=0 and also at t=τ.

-For the second, the homogeneous line is out of the spectral window at t=0 and in at t=τ

-For the third, the homogeneous line is in the spectral window at t=0 and out at t=τ.

-For the fourth term, the homogeneous line is out of the spectral window at t=0 and also at t=τ.

Let's evaluate $\rho((\gamma_{in}^{\tau} \mid (\mu_{in(out)}^{\tau})$, the probability that the TLS energy is in the right spectral window at time t when the center of the homogeneous line is in (out of) the right spectral window, making here the assumption that the homogeneous line is a lorentzian centered on $E = \mu$ and that, in accordance with the Kubo-Anderson model, the energy distribution of the fluctuations is gaussian.

$$\rho(\gamma_{in}^{\tau} \mid \mu_{in(out)}^{\tau}) = \frac{\rho(\gamma_{in}^{\tau} \cap \mu_{in(out)}^{\tau})}{\rho(\mu_{in(out)}^{\tau})} = 2\rho(\gamma_{in}^{\tau} \cap \mu_{in(out)}^{\tau}) \tag{5.60}$$

We consider a Lorentzian centered in the right spectral window,$(\mu\epsilon[I_{in}])$, and calculate the probability to measure a photon coming from it in the right spectral window.

For a given lorentzian centered in μ, the probability for the TLS to be in the right spectral window is the ratio between the lorentzian area in the right spectral window and its total area:

$$P_{\mu}(\gamma_{in}^{\tau}) = \frac{1}{\int^{\infty} lor(\sigma, E-\mu).dE} \int_{E\epsilon I_{in}} lor(\sigma, E-\mu).dE. \tag{5.61}$$

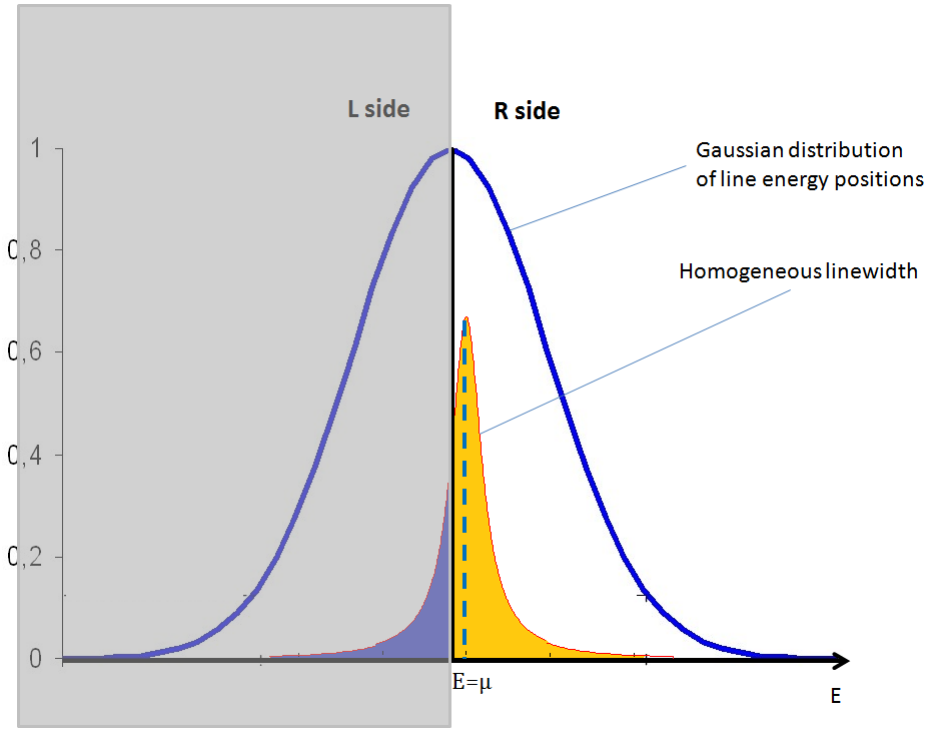

Figure 5.23: Lorentzian centered on energy μ and gaussian distribution of the possible μ positions. This distribution is cut by the spectral selection of the right part of the inhomogeneous line. It defines the area of the lorentzian where photons can be detected.

with

$$lor(\sigma, E-\mu) = \frac{\frac{2}{\pi\sigma}}{1+(\frac{E-\mu}{\sigma/2})^2}$$

We have then to consider the probability for the lorentzian to be centered at the position $E=\mu$, and have to multiply the previous expression by the probability density imposed by the gaussian distribution $Gauss(\Sigma,\mu)d\mu$ and integrate over all the μ such as: $\mu \epsilon I_{in}$.

$$\rho(\gamma_{in}^{\tau} \cap \mu_{in(out)}^{\tau}) = \frac{\int_{\mu \epsilon I_{in(out)}} (Gauss(\Sigma,\mu) \int_{E \epsilon I_{in}} (lor(\sigma, E-\mu).dE).d\mu)}{\int^{\infty} (Gauss(\Sigma,\mu) \int^{\infty} (lor(\sigma, E-\mu).dE).d\mu)} \tag{5.62}$$

with $Gauss(\Sigma,\mu) = \frac{1}{\Sigma_s 2\pi} exp\left(\frac{\mu^2}{2\Sigma_s^2}\right)$, the standard deviation $\Sigma_s = \frac{\Sigma}{2\sqrt{2ln2}}$.

This is the probability for the TLS to be in the right spectral window and the lorentzian centered in the right (left) spectral window at any time, so

it doesn't depend on the delay τ and are only functions of the homogeneous linewidth parameter $\sigma$and the flucutation amplitude Σ:

$$\rho(\gamma_{in}^{\tau} \cap \mu_{in(out)}^{\tau}) = \rho(\gamma_{in}^{0} \cap \mu_{in(out)}^{0}) = \alpha_{in(out)}(\sigma, \Sigma) \tag{5.63}$$

We rewrite the eq. 5.59 with these coefficients:

$$\rho(\gamma_{in}(\tau) \mid \gamma_{in}(0)) = 4\left[\alpha_{in}^2 \rho(\mu_{in}^{\tau} \mid \mu_{in}^{0}) + \alpha_{in}\alpha_{out}\rho(\mu_{in}^{\tau} \mid \mu_{out}^{0}) + \alpha_{out}\alpha_{in}\rho(\mu_{out}^{\tau} \mid \mu_{in}^{0}) + \alpha_{out}^2 \rho(\mu_{out}^{\tau} \mid \mu_{out}^{0})\right] \tag{5.64}$$

This probability depends on one hand on the coefficients $\alpha_{in}$and α_{out}which depend themselves on the geometry of the homogeneous lorentzian linewidth and of the gaussian distribution. They take into account the random uncorrelated statistic introduced by the finite homogeneous linewidth. On the other hand, eq. 5.64 depends on the probabilities $\rho(\mu^{\tau}_{in} \mid \mu^{0}_{in})$, $\rho(\mu^{\tau}_{in} \mid \mu^{0}_{out})$,$\rho(\mu^{\tau}_{out} \mid \mu^{0}_{in})$, $\rho(\mu^{\tau}_{out} \mid \mu^{0}_{out})$ which are describing how the center of the homogeneous linewidth is transiting from one spectral window to the other and take into account the correlated part of the statistic. All these probabilities can be determined analytically with the model of the infinitely sharp homogeneous linewidth presented in section 3.2 of this chapter and its associated rate equations.

For the first one,$\rho(\mu^{\tau}_{in} \mid \mu^{0}_{in})$, the probabitlity to have the line in the right spectral window at $t = \tau$ knowing it was at $t = 0$ is equal to the population of the right spectral window $n_R(\tau)$,with the initial condition $n_R(0) = 1$.

$$\rho(\mu^{\tau}_{in} \mid \mu^{0}_{in}) = (n_R(\tau) \mid n_R(0) = 1) \tag{5.65}$$

For simplicity, we consider the total population of the right spectral window and don't make a distinction between excited and ground states as it was in section 3.2.2. We will loose the single photon part of the autocorrelation function, but as explained in the same section, we'll just have to multiply by $[1 - exp(-(r + \gamma)\tau)]$ to find it back.

$\rho(\mu^{\tau}_{in} \mid \mu^{0}_{in})$ has already been calculated in section 3.2.2 and we also use eq. 5.30, eq. 5.37 and eq. 5.38, ($\gamma_R = \gamma_L = \frac{\gamma_c}{2}$):

$$\rho(\mu^{\tau}_{in} \mid \mu^{0}_{in}) = \frac{\gamma_R}{\gamma_c} + (1 - \frac{\gamma_R}{\gamma_c})exp(-\gamma_c\tau) = \frac{1}{2} + \frac{1}{2}exp(-\gamma_c\tau) \tag{5.66}$$

We do the same for the 3 other probabilities:

$$\begin{gathered}\rho(\mu^{\tau}_{in} \mid \mu^{0}_{out}) = (n_R(\tau) \mid n_R(0) = 0) = \frac{\gamma_R}{\gamma_c}[1 - exp(-\gamma_c\tau)] = \frac{1}{2}[1 - exp(-\gamma_c\tau)] \\ \rho(\mu^{\tau}_{out} \mid \mu^{0}_{in}) = (n_L(\tau) \mid n_R(0) = 1) = \frac{1}{2}[1 - exp(-\gamma_c\tau)] \\ \rho(\mu^{\tau}_{out} \mid \mu^{0}_{out}) = (n_L(\tau) \mid n_R(0) = 0) = [\frac{\gamma_L}{\gamma_c} + (1 - \frac{\gamma_L}{\gamma_c})exp(-\gamma_c\tau)] = [\frac{1}{2} + \frac{1}{2}exp(-\gamma_c\tau)]\end{gathered} \tag{5.67}$$

We put all these expressions in eq. 5.64 :

$$\rho(\gamma_{in}(\tau) \mid \gamma_{in}(0)) = \frac{1}{4}[\frac{1}{2}(\alpha^2_{in} + \alpha^2_{out}) + \alpha_{in}\alpha_{out} + (\frac{1}{2}(\alpha^2_{in} + \alpha^2_{out}) - \alpha_{in}\alpha_{out}).exp(-\gamma_c\tau)] \tag{5.68}$$

To obtain the correlation function, we divide this expression by the probability to detect a photon at any time: $\rho(\gamma_{in}(t)) = \rho(\gamma_{in}(\infty) \mid \gamma_{in}(0)) = \frac{1}{4}[\frac{1}{2}(\alpha^2_{in} + \alpha^2_{out}) + \alpha_{in}\alpha_{out}]$,

$$g^2_{in}(\tau) = 1 + \frac{(\frac{1}{2}(\alpha^2_{in} + \alpha^2_{out}) - \alpha_{in}\alpha_{out})}{(\frac{1}{2}(\alpha^2_{in} + \alpha^2_{out}) + \alpha_{in}\alpha_{out})}.exp(-\gamma_c\tau) \tag{5.69}$$

finally, rearranging terms and adding the emission part $g^2_{em}(\tau)$, one have:

$$g^2(R, R, \tau) = [1 + \frac{(\alpha_{in} - \alpha_{out})^2}{(\alpha_{in} + \alpha_{out})^2}.exp(-\gamma_c\tau)][1 - exp(-(r + \gamma)\tau)] \tag{5.70}$$

We recognize the β factor introduced in section 4.1.2, which was defining the importance of the bunching:

$$\beta = \frac{(\alpha_{in} - \alpha_{out})^2}{(\alpha_{in} + \alpha_{out})^2} \tag{5.71}$$

We can make two remarks about this factor:

- The bunching factor β is exclusively ruled by the uncorrelated random statistic of the finite homogeneous linewidth (expressed by coefficients $\alpha_{in}$and α_{out}), and is a function of σ and Σ. As shown on fig. 5.24, the bunching is important (red areas) for small σ and large the fluctuation amplitudes Σ.

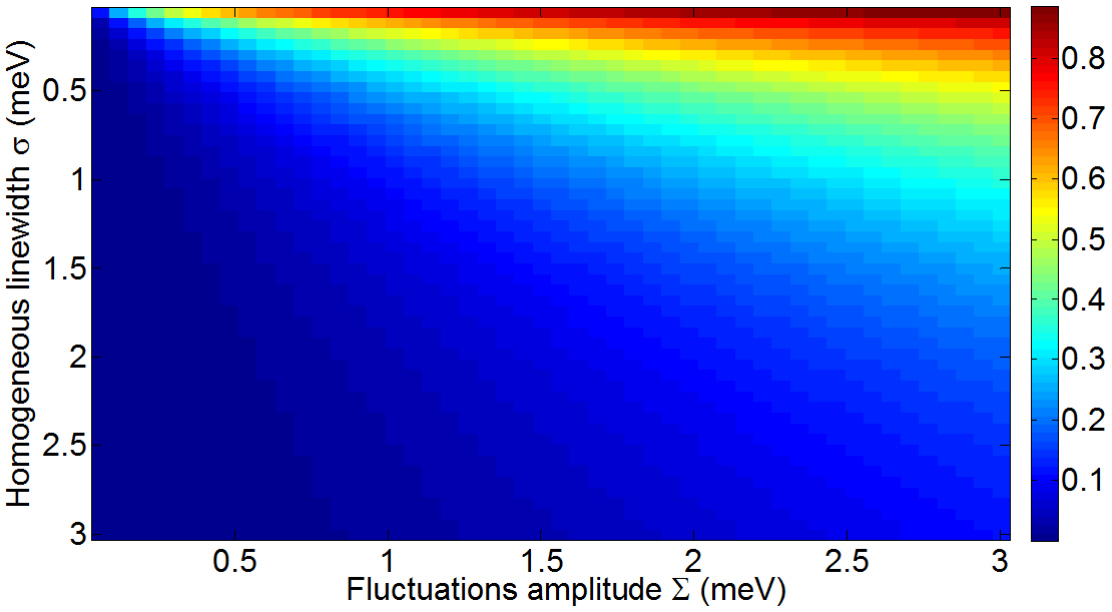

Figure 5.24: Bunching value depending on fluctuation amplitude Σ, and homogeneous linewidth σ

- The behaviour of β at the limits is interesting: When the homogeneous linewidth tends to 0, $\sigma \ll \Sigma$, and we have:

$$\alpha_{in} \to \frac{1}{2}$$
$$\alpha_{out} \to 0$$

so, $\beta \to 1$, which is its expected value in the case of the infinitley sharp linewidth.

When the homogeneous linewidth becomes much larger than the fluctuation amplitude, $\sigma \gg \Sigma$:

$$\alpha_{in} \to \frac{1}{2}$$
$$\alpha_{out} \to \frac{1}{2}$$

and $\beta \to 0$, the bunching is collapsing. This corresponds to a case where the poissonian satistic of the homogeneous linewidth takes over the correlated statistic of the spectral diffusion.

We'll see, in the last chapter of this part, that the phonon broadening of the homogeneous linewidth with increasing temperature finally dominates the spectral diffusion broadening of the gaussian fluctuation amplitude and defines the linewidth of the charged exciton transition.

To finish this section, lets remark that the halfline autocorrelation function bears simultaneously the signature of the subpoissonian emission statistic (zero delay dip), the correlated spectral diffusion energy statistic (bunching), and the poissonian energy statistic of the homogeneous linewidth (limitation of the bunching), the two last signatures, the correlated and the uncorrelated, having opposing effects.

5.4.3 Monte Carlo simulation:

In order to confirm the analytical expression of eq. 5.70 derived from complex calculi, we performed a montecarlo simulation, by building numerically the function $g^2(R,R,\tau)$ for a poissonnian emitter spectrally diffusing in and out of the detection spectral window. In this case, $g^2_{em}(\tau) = 1$ as for any poissonnian emitter. Thus, the simulation gives direct access to $g^2_{in}(\tau)$ and consequently to β.

After generating a poissonian photons stream we assign to each of them a random energy in a gaussian distribution. We calculate the probability of the homogeneous line to jump between the emission of the $(i-1)^{th}$ photon and the i^{th} photon:

The energy of the $(i-1)^{th}$ photon is in the interval:

$$I_{i-1} = I_{in} = \left[E_{i-1} - \frac{\delta E}{2}, E_{i-1} + \frac{\delta E}{2}\right]$$

with δE an infinitesimal energy.

In the case of a jump of the homogeneous line, the energy of the i^{th} photon is in the interval:

$$I_i = I_{out} = \left[-\infty, E_{i-1} - \frac{\delta E}{2}\right] \cup \left[E_{i-1} + \frac{\delta E}{2}, +\infty\right]$$

Thus, the probability for the homogeneous line to jump between the emission of the ith and the $(i-1)^{th}$ photon is:

$$P_{jump(i)} = \rho(\{\mu^{\tau} \epsilon I_{out}\} \mid \{\mu^0 \epsilon I_{in}\}) = \frac{\gamma_{out}}{\gamma_c}[1 - exp(-\gamma_c \tau)]$$

This probability has already been calculated in section 4.1 (fig. 5.67).

γ_{out} is the exit rate of the homogeneous line, from $I_{in}$to I_{out},$\gamma_c$is the "jump rate" of the homogeneous line.

For an infinitely small δE, $\gamma_c \backsim \gamma_{out}$ and:

$$P_{jump(i/(i-1))} = [1 - exp(-\gamma_c \tau)]$$

If the i^{th} photon doesn't jump it takes the same energy as the $(i-1)^{th}$ photon.

We then discriminate photons belonging to energies outside the detection area by applying an energy condition . They won't be counted in the correlation.

To calculate the correlation function of the resulting photons stream we compute the delay between the arrival of each photon and all the other photons of the stream. By building the histogram of these delays one obtain the correlation function of the stream. [122].

The result of the simulation is plotted on fig. 5.25a). We find again the result explained in previous section, the bunching part of the half line autocorrelation function takes a value of 2 at zero delay. To evaluate β from the simulated data, one onlys need to take $g^2(0)$.

To simulate the finite homogeneous linewidth effect we add for each photon an energy shift ε. ε is a random variable distributed along a lorentzian distribution of linewidth σ. The effect of this addition is shown on fig. 5.25b). As expected the bunching is less important and the β factor goes from 1 to 0.5 in the case of a finite homogeneous linewith $\sigma = 0.3meV$ and a fluctuation amplitude $\Sigma = 1.7\,meV$.

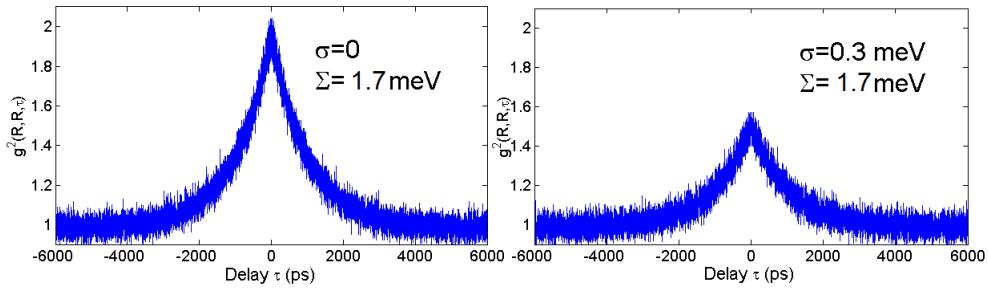

Figure 5.25: Calculated half line autocorrelation functions of a poissonnian emitter. a) for an infinitely small homogeneous linewidth, b) for an homogeneous linewidth $\sigma = 0.3meV$.

To compare this simulation with the analytical expression, we fix the Σparameter and change σ. We then report the calculated β values versus the ratio $\frac{\sigma}{\Sigma}$ (see fig. 5.26). We can notice that the two methods (analytical and Monte Carlo) give the same dependance, which validates the modelisation performed in the previous section.

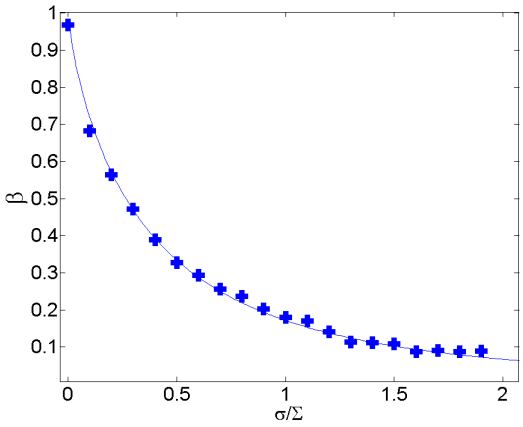

Figure 5.26: β versus the ratio between homogeneous linewidth and fluctuation amplitude. Red line: analytical model described in section 4.2. Blue dots: Monte Carlo simulation result.

5.4.4 Homogeneous linewidth and fluctuation amplitude determination

The fit of the experimental datas allows to extract, as 2 independant fit parameters, the correlation time τ_c and β. As shown in the previous section the latter depends on the fluctuation amplitude Σ and the homogeneous linewidth σ. To estimate them separately, we can use the emission spectrum measured, and by making the same assumptions as before (the homogeneous line is lorentzian and the fluctuation distribution is gaussian) we obtain a second equation linking

the 2 parameters.

$$S(\sigma, \Sigma, \omega) = \int_{-\infty}^{+\infty} lor(\sigma, \omega).gauss(\Sigma, \omega - \xi)d\xi \tag{5.72}$$

$$\beta = \beta(\sigma, \Sigma) \tag{5.73}$$

The spectrum $S(\sigma, \Sigma, \omega)$ is the convolution of the homogeneous line and the fluctuation distribution and is represented in eq. 5.72 by a Voigt function. We need to perform a double fit to extract the good values of $\sigma$and Σ, as it exists an infinity of couples (σ, Σ) satisfying the first or the second equation. The solution couples of the the spectrum fit are tested with the second equation and the good values of σ and Σ are then selected.

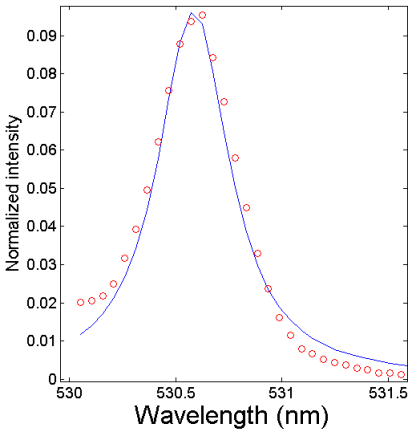

Figure 5.27: Spectrum of the charged exciton line fitted with a Voigt profile.

This process was repeated on 3 nanowire quantum dots. The correlation measurements and spectrum fits were done on the charged exciton lines as they were the most luminescent for most of the temperature and excitation power applied. On fig. 5.28, the 3 resulting experimental points are plotted. They represent the mesured β parameters versus the homogeneous linewidths. We can notice that despite the emission lines of these 3 charged excitons correspond to 3 different fluctuation amplitudes (1.2 meV, 1.4 meV and 1.7 meV), the homogeneous linewith we find is the same (around 300 μeV). This value is actually the spectral resolution of the experiment, and it limits our measurement. The true homogeneous linewidth is probably smaller but, one needs a better spectral resolution to have acces to it. For the 3 different fluctuation amplitudes considered, the curves $\beta(\sigma)$ are plotted. They follow the same trend: For an increasing homogeneous linewidth, β is decreasing, ie the bunching contrast gets lower. It also shows that for large Σ, the autocorrelation of the half-line gives a more pronounced bunching. The last interesting point is that, for a very small homogeneous linewidth, bunching is larger but the fluctuation amplitude is less influent on its value and it becomes harder to have a good precision on its measurement.

5.4.5 Measurement precision

The last interesting point is that, for a very small homogeneous linewidth, bunching is larger but the fluctuation amplitude is less influent on its value. Hence it becomes harder to have a good precision on its measurement. Indeed, as shown in fig. 5.28, the 3 bunching curves are converging

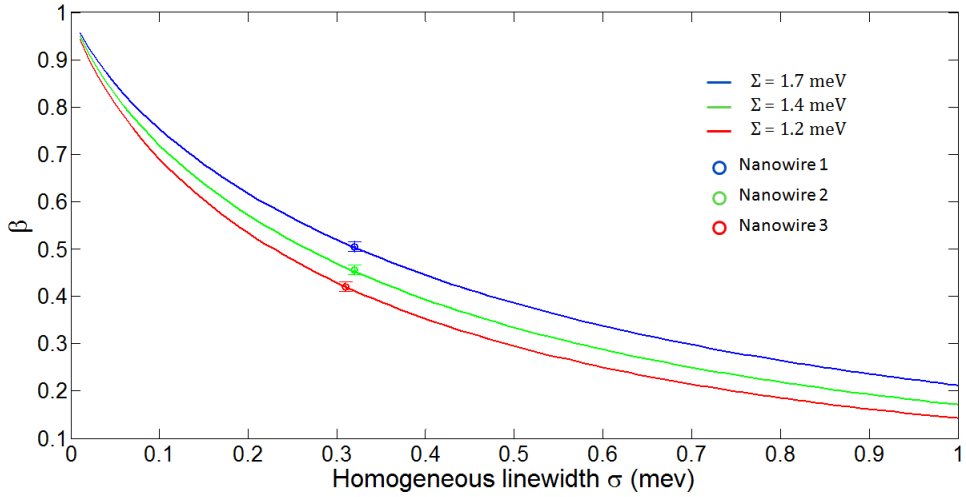

Figure 5.28: Parameter β versus homogeneous linewidth for 3 different fluctuation amplitudes Σ (1.2 meV, 1.4 meV, 1.7 meV). The 3 points are experimental datas taken from the emission of the charged exciton of 3 different quantum dots.

for very small homogeneous linewidth values. When $\sigma \ll \Sigma$, the precision on the measurement is very poor. It is also the case when $\sigma \gg \Sigma$. To estimate what is the measurement precision and determinate an optimal ratio, where the experiment is the most performant we define the quantity p such as:

$$p = \left| \frac{\sigma}{\Sigma} \cdot \frac{d\beta}{d(\frac{\sigma}{\Sigma})} \right|$$

p quantifies the sensitivity of the bunching value to a variation of the ratio. In fig. 5.29, p is plotted as a function of the ratio. The precision is optimal for a ratio $\frac{\sigma}{\Sigma} = 0.37$, corresponding to the abscisse of the maximum value of p (see fig. 5.29). Thus, the experiment is generally well adaptated to homogeneous linewidth σ which are on the same order of magnitude as Σ, and still smaller than Σ. If we consider the precision good enough when p=0.2, the condition on σ is:

$$0.1\Sigma < \sigma < \Sigma$$

5.4.6 Conclusion

We showed here that the auto-correlation technique can bring all the informations for the full characterization of a spectrally diffusing emitter. Indeed, after data treatment technique presented in the last section of this chapter, one can obtain seperately σ (homogeneous linewidth), Σ (fluctuation amplitude) and Γ_c (correlation rate)

It is however limited spectrally by the monochromator resolution (300 μev in this work) and temporally by the single photons detectors resolution (700 ps in this work). Even if the spectral resolution can be optimized, it will be hard to reach resolution obtained by PCFS method, and even if it was possible we saw that the precision of the measurement would be degraded for such large fluctuation amplitudes. Though, the correlation technique is much easy to set up.

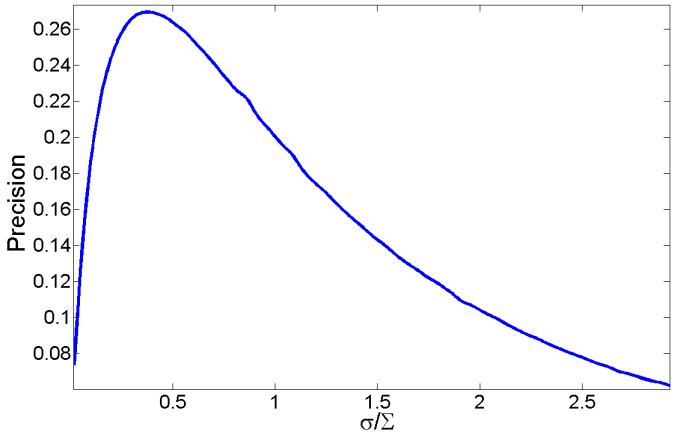

Figure 5.29: Precision of the measurement versus ratio $\frac{\sigma}{\Sigma}$

5.5 Application to spectral diffusion in a single nanowire quantum dot

Effects of a fluctuating environnement of a quantum dot has already been studied by several methods described in section 3 of this chapter. We showed in the previous chapter how powerful and easy to set up was the photon correlation method and until which point it allows the user to have access to many of the characteristic physical values of a frequency fluctuating emitter, at the same time . Indeed, we now have quite easily access to the correlation rate, the fluctuation amplitude and, under some restrictions, the homogeneous linewidth. To study how these quantities are evolving, we will tune the environnement fluctuations by the 3 parameters at our disposal: excitation power, temperature and excitation wavelength. Finally, we will interpret the evolution of these quantities following the Kubo Anderson model[111] and will extract some important conclusions on the line braodening of a single photon emitter.

5.5.1 Correlation rate and fluctuation amplitude

Correlation rate

Keeping in mind the idea of the quantum confined Stark effect introduced in section 1, we can write down the expression of capture and escape rate of a carrier in the vicinity of a quantum dot by summing the possible physical processes. A carrier can be captured or can escape from a trap by optical or accoustic phonons absorption or emission and by Auger processes.

Thus, the capture rate $\Gamma_{\downarrow}$ and escape rate $\Gamma_{\uparrow}$ can be written as:

$$\Gamma_{\downarrow} = \Gamma_{ac}(N_{B1}+1) + \Gamma_{op}(N_{B2}+1) + f(P)$$
$$\Gamma_{\uparrow} = \Gamma_{ac}N_{B1} + \Gamma_{op}N_{B2} + f^{'}(P)$$

Γ_{ac} and Γ_{op} are the accoustic and optical phonon assisted capture rates at 0K, $N_{B1}$and N_{B2}

are the accoustic and optical phonon populations and are function of temperature such as:

$$N_{B1} = \frac{1}{1 - e^{-\frac{E_1}{k_B T}}}$$
$$N_{B2} = \frac{1}{1 - e^{-\frac{E_2}{k_B T}}}$$

E_1 is the energy of an accoustic phonon and E_2 the energy of an optical phonon.

$f(P)$ and $f^{'}(P)$ describe the Auger processes involved in the escape or capture of a carrier. They depend on power but their dependancies are not known and are probably different. We can only give their general expression:

$$f(P) = \Gamma_{aug} \left(\frac{P}{P_0} \right)^{\beta} \tag{5.74}$$

If we approximate the environning traps of the quantum dot as N independant TLS with non symmetrical fluctuations (sec 2.3.3.), the correlation rate is the sum of the escape and capture rates:

$$\Gamma_c = \Gamma_{\uparrow} + \Gamma_{\downarrow} \tag{5.75}$$

Fluctuation amplitude

In section 2.3.3, we derived the expression of the fluctuation amplitude as a function of the capture and escape times, given by the non symmetrical Kubo Anderson model:

$$\Sigma = \frac{\sqrt{N}\Delta}{\hbar(\sqrt{\frac{\tau_{\downarrow}}{\tau_{\uparrow}}} + \sqrt{\frac{\tau_{\uparrow}}{\tau_{\downarrow}}})}, \tag{5.76}$$

It is a function of the ratio between $\Gamma_{\uparrow}$ and $\Gamma_{\downarrow}$. The symmetry of the escape and capture processes will highly influence the amplitude of the fluctuations.

5.5.2 Power dependence

At 4K, the expressions of capture and escape rates are more simple, as $N_{B1} \approx N_{B2} \approx 0$.

$$\Gamma_{\downarrow} = \Gamma_{ac} + \Gamma_{op} + f(P)$$
$$\Gamma_{\uparrow} = f^{'}(P) \tag{5.77}$$

The ratio between these rates which are ruling the amplitude are such as:

$$\frac{\Gamma_{\downarrow}}{\Gamma_{\uparrow}} = \frac{\Gamma_{ac} + \Gamma_{op} + f(P)}{f^{'}(P)} \tag{5.78}$$

To simplify the problem, we will make the approximation that the same auger process is involved in the capture or the escape of a carrier:

$$f(P) = f^{'}(P) \tag{5.79}$$

The relaxation of carriers in traps by coupling to optical phonons are reported at the picosecond scale[118]. If we were probing them, they would dominate the correlation rate and limit the correlation time to a few ps, which is not the case. Measured time are in the nanosecond scale. These ultrafast fluctuations are probably in the "homogeneous linewidth" we defined in the previous chapter, and are out of sight of our experiment for temporal resolution reasons. In the following we will only consider optical phonon processes for the capture or the escape of carriers.

Thus,

$$\frac{\Gamma_{\downarrow}}{\Gamma_{\uparrow}} = \frac{\Gamma_{ac}}{f(P)} + 1 \tag{5.80}$$

In the last expression it is easy to predict how the ratio will evolve with power. In the low power regime, the Auger process contribution is very small and the ratio is such as $\frac{\Gamma_{\downarrow}}{\Gamma_{\uparrow}} \gg 1$. This means that the fluctuations are highly non symmetrical: the capture of carriers dominates the fluctations at low power. In the high power regime, the Auger term becomes larger than the capture assisted by phonon coupling Γ_{ac}, then $\frac{\Gamma_{\downarrow}}{\Gamma_{\uparrow}} \to 1$. Auger processes are dominant for both the escape and capture, and as a result fluctuation become symmetrical.

On fig. 5.30 are plotted the correlation rates and amplitudes as a function of excitation power. As described above, the correlation rate and FWHM increase with power. The power dependent Auger process become faster and makes the fluctuations symetrical, ie the FWHM gets larger. Both of the experimental measurements of the amplitude and the correlation rate with power are fitted with a global method. The best global fit is given for the following set of parameters: $\beta = 0.65$, $\Gamma_{ac} = 0.03ns^{-1}$, $\Gamma_{aug} = 0.06ns^{-1}$, $P_0 = 1.1mW$. We can notice that the Auger processes dominate quickly the phonon-carrier coupling mechanisms which are relatively inefficient at 0K ($T_{ac} = 33ns$), this is why the FWHM is saturating in the high power regime.

5.5.3 Temperature dependance

We saw that we could interpret the experimental datas obtained via photon correlation technique and with varying power with the help of the Kubo Anderson model. In this section,we study how temperature influences the emitted photons energy statistic and the environnement fluctuation processes.

Homogeneous linewidth broadening and fluctuation amplitude

When the temperature is increased, the first striking consequence on the half line autocorrelation measurement is a quick collapse of the bunching. In fig. 5.31, are plotted the right half line autocorrelation figures for different temperatures from 4K to 60K. The value of the β factor we introduced in chapter 4 is decreasing from the initial value of 0.5 to almost 0 near 60K. No bunching is observed at higher temperatures for this quantum dot with fluctuation amplitude for the charged exciton of 1.7 meV.

Such decrease of β with temperature can only be attributed to a broadening of the homogeneous linewidth, thanks to exciton-phonon coupling. The energies of photons resulting from such coupling are randomly distributed along a complex temperature dependant energy profile [123] that we will approximate here by a lorentzian with variable linewidth $\sigma(T)$. These energies are governed by a poissonian process and are not time correlated . This bunching collapse means that total photon energy statistic belongs more and more to a poissonian process type and is less and less time correlated by the spectral diffusion process.

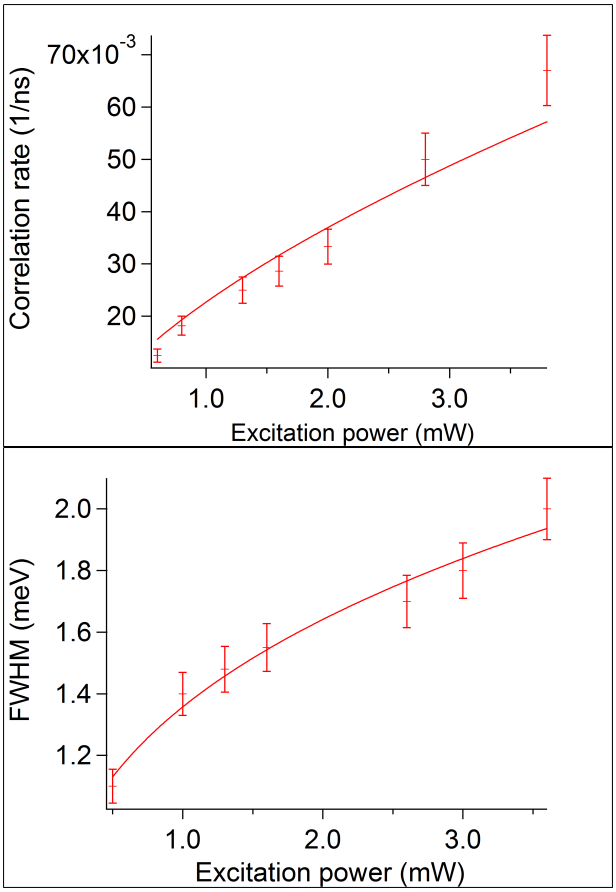

Figure 5.30: a) Correlation rate versus power exictation for the 3 different nanowires. b) FWHM vs excitation power. Fit parameters are given in the text.

For a different quantum dot, with weaker fluctuation amplitude Σ (1.2 meV), the the bunching totally collapses around around 40K. As the value of β depends on the ratio between the fluctuation amplitude and the homogeneous linewidth, the latter needs to be less broadened (ie at smaller temperature) to catch up a smaller fluctuation amplitude.

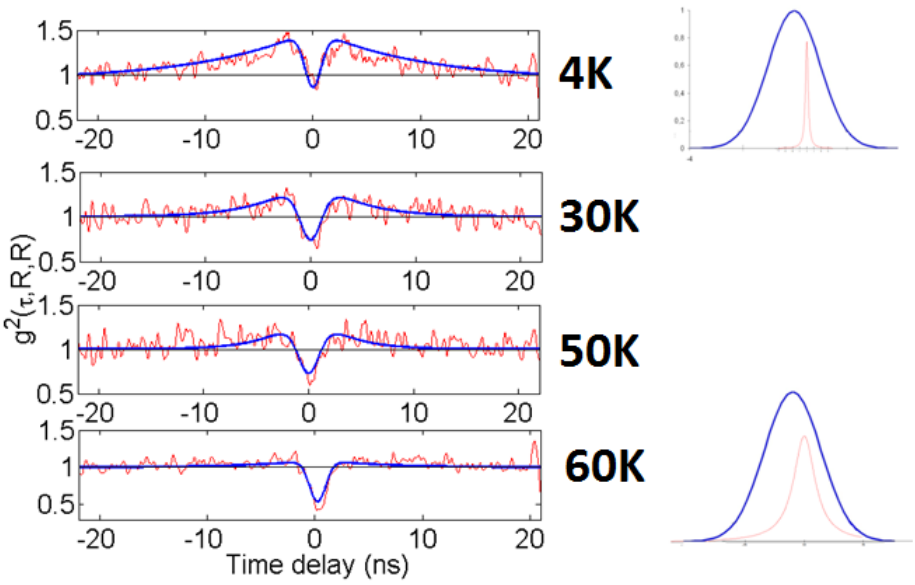

Figure 5.31: Autocorrelations of the right spectral side of the line for increasing temperature. On the right of the figure, illustration of the broadening of the homogeneous line (red line) in the Gaussian distribution of the fluctuations (blue), in the approximation of a Lorentzian homogeneous line profile model.

We can have more precise informations on the temperature dependance of the photon energy statistic by evaluating the effective homogeneous linewidths and the fluctuation amplitudes for different temperatures. This is reported on fig. 5.32 (dots for the homogeneous linewidth and squares for the fluctuation amplitudes), for two different quantum dots (blue and red color). The two quantities are determined with the method exposed in section 4.2. As suspected during the observation of the autocorrelation figures, the effective homogeneous linewidths increase with temperature, they reach the same order of magnitude as the fluctuation amplitude and even become larger for high temperatures (40-60K). The increase of the linewidth is similar for the two quantum dots, which is a good indication on the reproductibility of the measurement.

The other important information is that the fluctuation amplitude is constant with temperature (for the investigated 2 quantum dots). We will discuss more precisely this surprising phenomen in the next subsection. By increasing the temperature, one only broadens the distribution of the energy-shifts imposed by the homogeneous linewidth, and the distribution of the fluctuations due to the spectral diffusion remains the same. This has two consequences:

-The temperature broadening of the FWHM observed on the spectra are only due to the phonon broadening of the homogeneous linewidth.

-At room temperature the measured FWHM of 16 mev is in very large part the result of the phonon broadening. The energy of the photons detected from these large lines are randomly distributed with a poissonian process. The time correlated jumps of the spectral diffusion are negligible. Thus, if someone has the objective to generate coherent single photon emission with a very sharp band energy at room temperature, it is useless to fight against spectral diffusion. To begin, it is more relevant to try to reduce the temperature induced phonon coupling.

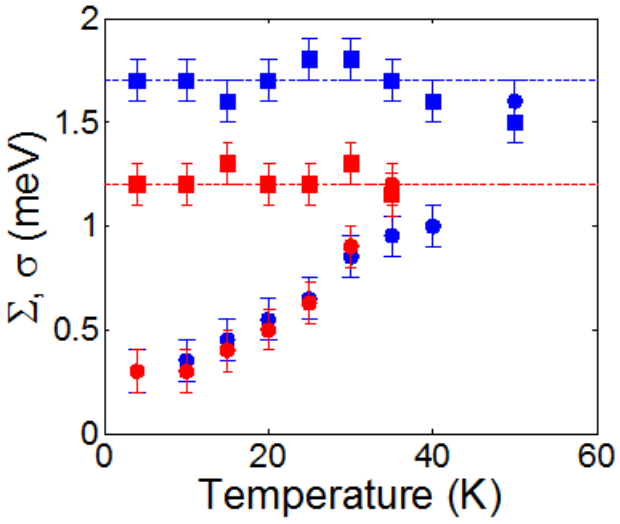

Figure 5.32: Fluctuation amplitude (squares) and homogeneous linewidth (dots) for 2 different quantum dots (red and blue)

Temperature effect on the Correlation rate

As we did for the power dependance of the spectral diffusion, we will interpret the correlation rate and fluctuation amplitude temperature dependances with the help of the Kubo Anderson model. In the previous subsection we pointed out that the amplitude of the fluctuations were constant with temperature. In fig. 5.33, we plotted the correlation rate versus temperature. We observe a slight increase of this quantity, which is due to the enhancement of the phonon population.

$$\Gamma_c = \Gamma_{ac}(2N_{B1}+1) + 2f(P) \tag{5.81}$$

At the same time the ratio between escape and capture rates is:

$$\frac{\Gamma_\downarrow}{\Gamma_\uparrow} = \frac{\Gamma_{ac}(N_{B1}+1)+f(P)}{\Gamma_{ac}N_{B1}+f(P)} = 1 + \frac{\Gamma_{ac}}{\Gamma_{ac}N_{B1}+f(P)} = 1 + \frac{\frac{\Gamma_{ac}}{f(P)}}{1+\frac{\Gamma_{ac}N_{B1}}{f(P)}} \tag{5.82}$$

For efficiency and integration time reasons, these temperature dependent measurements where done at high power, for $\frac{\Gamma_{ac}N_{B1}}{f(P)} \ll 1$, so we can approximate this expression as follows:

$$\frac{\Gamma_\downarrow}{\Gamma_\uparrow} \approx 1 + \frac{\Gamma_{ac}}{f(P)} - \Gamma_{ac}^2 N_{B1}(T).\left(\frac{1}{f(P)}\right)^2 \tag{5.83}$$

In the high power regime, where Auger processes are dominating, the temperature increase of the phonon population have much less influence on the $\frac{\Gamma_\downarrow}{\Gamma_\uparrow}$ ratio, as they belong to the power second order term.

The second reason why tempretaure is not affecting the FWHM in the high power regime is that the amplitude is saturating when $\frac{\Gamma_\downarrow}{\Gamma_\uparrow} \sim 1$. Indeed, as we discussed in section 2.3.3. on the

gerneralization of the Kubo anderson model for non symetrical fluctuations:

$$\left(\frac{d\Sigma}{d\left(\frac{\Gamma_\downarrow}{\Gamma_\uparrow}\right)}\right)_{(\frac{\Gamma_\downarrow}{\Gamma_\uparrow})\to 1} = 0.$$

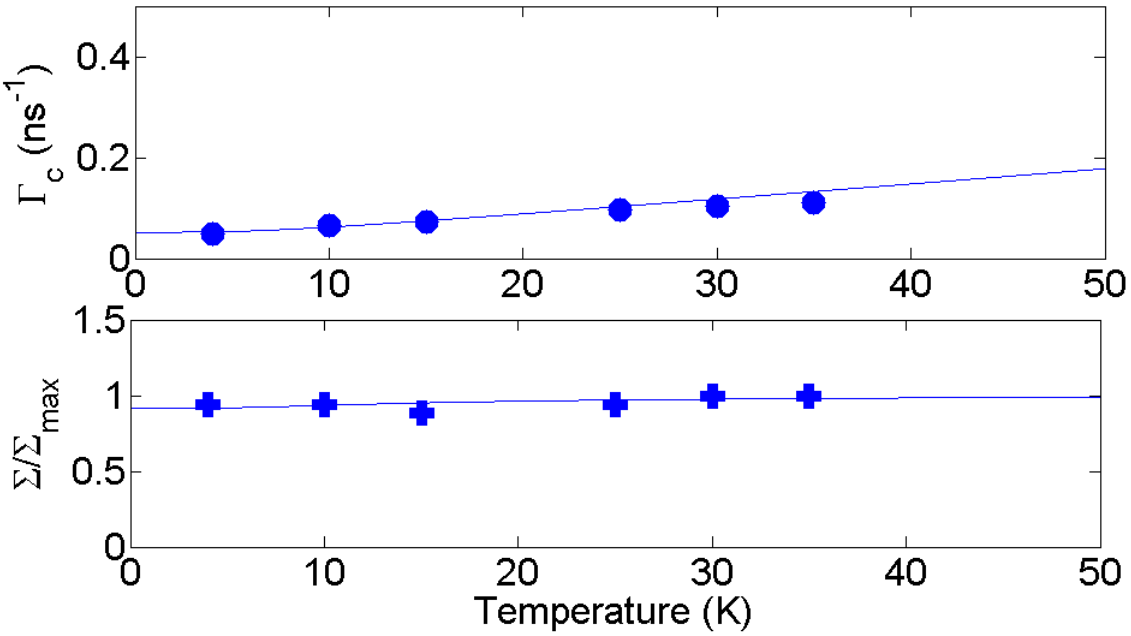

Figure 5.33: The correlation rate (blue dots) , and the relative fluctuation amplitude (blue crosses) versus the temperature. Plain lines are results given by the Kubo Anderson model.

For the fits, we used the same parameters determined for the power dependance: $\Gamma_{ac} = 0.03ns^{-1}$, $\Gamma_{aug} = 0.06ns^{-1}$, $\beta = 6.5$. the power is fixed at P=3mW, and the fit gives an accoustic phonon energy $E_{ac} = 1.5$meV, It can be interpreted as the mean energy given by the carrier to the system during its relaxation in the trap.

5.5.4 Conclusion

Thanks to the Kubo anderson model, we are able to explain qualitatively the evolution of the fluctuations with temperature or power, by paying the price of a few approximations. Increase of the excitation power activates auger processes which are quickly overcoming relatively inefficient accoustic phonons assisted relaxations and make escape and capture rates symmetrical. This results in an increase and eventually in a saturation of the line FWHM. This interpretation is in opposition with the model proposed in this reference [116], where a single charge is trapped in the vicinity of the quantum dot, all the other charges being repulsed by coulomb interaction. This picture would explain a constant FWHM with increasing power but is not consistent with the increase of the FWHM observed in our case. On the contrary, their experimental observations can be interpreted via the kubo Anderson model. Indeed, for accoustic phonons relaxation totally inefficient or negligible, one can imagine that the Auger processes are ruling capture and escape

processes, even at low power, thus fluctuations would be aways symmetrical and the fluctuation amplitude would be constant with power.

We also obtained conclusions about how temperature influences the energy emission statistic. Indeed, the amplitude of the time correlated spectral diffusion is constant with temperature, while phonon broadening gets more and more important, and is actually the only responsible for the observed spectral line broadening. Thus, at high temperature, the uncorrelated phonon broadening process is dominating the correlated spectral diffusion process, and the expression of this domination is a constant half line energy correlation function.

General conclusions and perspectives

The results obtained in this thesis are the result of the exploitation of a unique sample, except a few results concerning correlation of optical measurements and microscopy. The latters are related to characterisation work on the different samples produced during 3 years. Dispersion of the optical properties observed on the quantum dots of the same sample allowed us to conduct fine studies and to show different interesting dependances. One could say that we turned imperfections of our objects into opportunities -the spectral diffusion topic is a good example- to understand their physical properties, and we even opened our experiments and reflexions towards more general considerations. We present here the main conclusions of this work in the order of presentation of this manuscript, each of them followed by the description of the corresponding perspectives.

Neutral nanowire quantum dots

We investigated the excitonic dynamic in the CdSe/ZnSe nanowire quantum dots. Early studies were performed by Gregory Sallen on these structures during his thesis but they were limited to a characterisation work - identification of the emission lines, influence of the dark exciton state on the dynamic of charged quantum dots. By a theoretical work, we detailed the exciton-acoustic phonon coupling, responsible for the hole spin flip transition from the bright to the dark state. We investigated the quantum dots size effects, we determined for which conditions the efficiency of the coupling is the most important, explaining the increase of the bright exciton depopulation with exchange energy. We then included the effects of a thermal phonon bath, induced by the increase of the temperature in the model. It allowed us to explain experimental results obtained at high temperature and to extract a very interesting conclusion: the exciton luminescence intensity remains smaller than the biexciton intensity at room temperature. This set of results is specific to the studied structure, and exhibits a few original behaviour for a condensed matter single photon emitter, especially for a semi-conductor quantum dot. The large measured exchange interactions and fast spin-flip processes are the result of small dimensions of the quantum dot and very good confinement. This is a consequence of the nanowires VLS growth mode, which implies the absence of the wetting layer and a more abrupt confining interface between the small gap and the large gap semi-conductors.

This is one of the reasons why research on nanowires in our group switched towards the fabrication of magnetic nanowires in the hope that coupling between the quantum dot carriers and magnetic atoms spins inserted around the quantum dot will be enhanced. In addition, control on the quantum dots size and geometry is expected in these structures in order to provide tunable magnetic anisotropy. The main idea is to insert manganese magnetic atoms in the nanowires. As radiative internal transitions of the Mn atom are in the emission range of CdSe/ZnSe nanowire quantum dots, it has been decided to investigate the growth of CdTe/ZnTe nanowire quantum dots. The growth of such structures is relatively new and first optical results were reported very

recently by an other group [72].

Room temperature single photon emission

We demonstrated room temperature single photon emission. This result is specific to this system for two reasons. First, the use of the biexcitonic transition is a very original choice if we consider other room temperature operating emitters such as nanocrystals where biexciton is hardly observed because of very efficient Auger processes. The presence of the exciton and of the biexciton in a close energy range is a major obstacle to the production of quality single photon emission signal at high temperature. We showed that, by essence, the pollution of biexcitonic single photon emission by the exciton emission is important because of their correlation. Thus, the weakness of the exciton luminescence in our system was a decisive feature. The second reason which was not less decisive, was the very good resistance against temperature. Again, this is due to the nanowire growth mode and the abscence of a 2D layer which is an undesirable connection between quantum dots and the main channel for carriers escape in self-assembled systems.

To finish on this point, note an appreciable property of these quantum dots: a very fast spontaneous emission rate, with a lifetime of only 300 ps. This could allow to reach an extremely high single photon emission frequency (2.5 Ghz) and to avoid slower decoherence processes which are reducing the photons indistinguishability, without the need to use any microcavity and the associated Purcell effect. The eventual implementation of such microcavity would accelerate even more an already very fast emission of the quantum dots[72], potentially leading to very efficient two-photon interferences [95] and a high fidelity generation of polarization entangled photons pairs[125, 126]. In the case of nanowire quantum dots, with an intrinsec very good in-plain isotropy, the latter idea can be an extremely interesting perspective.Providing the nanowires could be observed as grown, from the top.

Temperature robustness and indistinguishability of photons are not the only issues in the quest of single photon emission from quantum dots. One can also expect them to be efficient. During the last years Julien Claudon et. al. developed a top down fabrication strategy leading to photonic nanowires guiding the emission of III-V quantum dots. They even optimized their etching process in order to fabricate a taper with a special angle and eventually extracted 72% of the light emitted by the quantum dot[127]. This is an impressive achievement if we consider that a quantum dot is shining in every direction and that only a small fraction of the light emitted in the light cone defined by the numerical aperture of the objective is collected. The VLS growth mode of the nanowires forbbids to use the top down approach. However the bottom up version of Julien Claudon' s work would be the fabrication of core shell structures, with lateral growth of ZnSe shells around the nanowires. The advantage is the assurance to have one single quantum dot in each core shell structure. And more important: the quantum dot would be perfectly centered. The efficiency of the emission guide is dependent on the position of the quantum dot with respect to the photonic wire axis[128]. Instead of having randomly distributed quantum dots in the photonic wire, we would obtain a deterministically centered single quantum dot in every photonic wire.

Dynamic of charged quantum dots

We also studied the dynamic of charged quantum dots. We didn't use them for room temperature single photon emission even though they represent 80% of the explored quantum dots. The charged exciton line could be a good candidate, as its emission is not correlated with exciton and biexciton lines. However its energy position (between exciton and biexciton) is not favourable.

At high temperature, we would detect the correlated pollutions of the exciton and the biexciton. The solution would be to use permanently charged quantum dots, with no neutral line, but no clear identification of such spectra has been done.

Charged quantum dots were interesting for an other reason: they exhibited two charged biexciton lines. Cross correlation measurements between these lines and the charged exciton line allowed us to detail the excited trion fine structure and to measure the speed of its different relaxation mechanisms, in particular to give a carrier spin flip time of around 200 ps. The different mechanisms measured times led us to think we were dealing with p-doped quantum dots, which is relatively surprising for a naturally n-doped material such as CdSe. There is no easy experiment to test this hypothesis. It is extremely difficult to apply a voltage bias on 10 nm nanowires, even if the skills necessary to contact sub-micrometer nanowires are present in the group. Presently, the resolution of the SEM associated with the electron gun insulating the resine for the fabrication of nanowires contact is not sufficient. Moreover, we didn't detect any luminescence from the ZnSe nanowires, wich could have constituted a good marker. Such nanowire electroluminescence technology was developped recently with the fabrication of quantum light emitting diodes comprised on a single InAsP quantum dot embedded within the depletion region of a p-n structure[129]. After optimization, and reduction of non radiative processes in the doped nanowire, one can expect the possibility to product electrically pumped single photon emitter with nanowires. The production of such an object requires the intentional p and n doping of the nanowire. Even though this operation is routinely performed in III-V nanowires, this is far to be our case.

One dimensionnal effects

From the geometry of the nanowires, one would suppose that 1D effects can be probed on these structures. Physics on 1D systems is very appealing on the paper but is extremely hard to demonstrate experimentally. The two attempts made in this direction failed. For the first one, the strong lateral confinement in the nanowire imposes a discretisation of the phonon dispersion[130]. Theoretically, the consequence on the emission spectrum is the presence of resonances in the phonon broadening, which should appear clearly on both sides of the zero-phonon line when the temperature is increased[131]. Because of the very small diameter of the nanowires (10 nm) the resonances should be well separated ($\sim 1\,meV$ between the resonnances). The fact we observed a bulk-like phonon broadening makes us think that we don't study a clean 1D system, but the presence of numerous defects convolve the nice discretisation of the phonon dispersion we expected. The purpose of the second attempt was to probe the electronic 1 D density of state of the nanowire by a photoluminescence excitation above the ZnSe 442 nm bandgap. In principle, one should observe a characteristic $\frac{1}{\sqrt{E}}$ dependance with multiple resonances due to the lateral confinement. The calculations predicted a 4 meV separation between the 2 first resonnace peaks. But no such resonnance was observe clearly and the PLE spectrum looked flat.

Spectral diffusion

The spectral diffusion topic was already approached by Gregory Sallen during his thesis. He developped the experimental technique allowing to measure correlation time in the nanosecond range. From this, we sophisticated the understanding of the measurement and extended its possibilities. By a theoretical work, we showed that the half-line autocorrelation function gives access not only to the emission statistic (as the traditionnal HBT setup does), but also to the emission energy statistic. We extricated the influences of the uncorrelated homogeneous

linewidth energy distribution and the correlated spectral diffusion process. By measuring the bunching contrast, one can extract the relative importance of the two different statistics. Direct applications of this theoretical approach is the determination of the homogeneous linewidth, in the limit of the experimental resolution, and the amplitude of the spectral diffusion. In particular, temperature dependant experiments showed that the latter amplitude was constant and the exciton-phonon coupling was the only responsible for the temperature induces line broadening. This phonon braodening proves to be the dominant mechanism in the high temperature ranges and the spectral diffusion effect is then negligible. This conclusion is important. This means, that the main obstacle to indistinguishable single photon emission at room temperature is not spectral diffusion, but coupling of the emitter to phonons. It would be interesting to see if this behaviour is general to all the condensed matter systems, or if it is very specific to our quantum dots. Anyway, we believe that the experimental method we propose is realistic and easy to set up for any spectroscopy group.

We also analyzed the influence of the temperature and the excitation power on the fluctuation of the quantum dots electronic environnement. After interpretating the experimental results with the help of the Kubo-Anderson model, the main conclusions we extracted was that the symmetrisation of the fluctuations was playing an important role on their amplitude and speed and that the Auger process was the dominant process for capture and escape of the carriers, especially at high power where they are responsible for a total symetrisation of the fluctuations. This symmetrisation of the fluctuations leads to a saturation of the spectral diffusion amplitude. When temperature is increased, the amplitude is the same. Thus, phonon broadening amplitude can catch up spectral diffusion and dominate the spectrum, this explains the conclusion we did on the relative importance of emission energy statistics derived from the bunching contrast.

Bibliography

[1] H. J. Kimble, and L. Mandel, Theory of resonance fluorescence,Phys. Rev. A 13, 2123–2144 (1976)

[2] H. J. Kimble, M. Dagenais, and L. Mandel, Photon Antibunching in Resonance Fluorescence, Phys. Rev. Lett. 39, 691–695 (1977)

[3] C. K. Hong, Z. Y. Ou, and L. Mandel, Measurement of subpicosecond time intervals between two photons by interference, Phys. Rev. Lett. 59, 2044–2046 (1987)

[4] Nielsen, M.A. and Chuang I.L., Quantum computation and quantum information, Cambridge Univ. Press, Cambridge, UK, 2000.

[5] H.J. Kimble, The quantum internet, Nature 453, 1023-1030 (2008)

[6] X. Peng, L. Manna, W. Yang, J. Wickham, E. Scher, A. Kadavanish, and A. P. Alivisatos, Nature London 404, 59 2000.

[7] P. Michler, A. Kiraz, C. Becher, W. V. Schoenfeld, P. M. Petroff, Lidong Zhang, E. Hu, A. Imamoglu, A Quantum Dot Single-Photon Turnstile Device, Science 290, 2282 (2000).

[8] B. Lounis and W. E. Moerner. Single photons on demand from a single molecule at room temperature. Nature 407, 491 (2000).

[9] Benoit Mahler, Piernicola Spinicelli, Stephanie Buil, Xavier Quelin, Jean-Pierre Hermier, Benoit Dubertret, Towards non-blinking colloidal quantum dots, Nature Materials 7, 659 - 664 (2008)

[10] R. Hanbury Brown & R. Q. Twiss, Correlation between Photons in two Coherent Beams of Light, Nature 177, 27 - 29 (07 January 1956)

[11] Nicolas Gisin, Gregoire Ribordy, Wolfgang Tittel, and Hugo Zbinden, Quantum cryptography, Rev. mod. phys., Vol. 74 (2002)

[12] E. Knill, R. Laflamme & G. J. Milburn, A scheme for efficient quantum computation with linear optics, Nature 409, 46 (2001)

[13] S. Le Goff and B. Stobe, Influence of lateral and longitudinal confinements on excitons in cylindrical quantum dots of semi-conductors

[14] C. B. Murray, D. J. Norris, and M. G. Bawendi. Synthesis and characterization of nearly monodisperse CdE (E = sulfur, selenium, tellurium) semiconductor nanocrystallites. Journal of the American Chemical Society, 115(19):8706–8715, 1993.

[15] R.S. Wagner and W.C. Ellis. Vapor-liquid-solid mechanism of single crystal growth. Applied Physics Letters, 4(5):89–90, 1964.,

[16] J. Westwater, D.P. Gosain, S. Tomiya, S. Usui, and H. Ruda. Growth of silicon 23 nanowires via gold/silane vapor–liquid–solid reaction. J. Vac. Sci.Technol. B: Microelectronics and Nanometer Structures, 15(3):554–557, 1997.

[17] Y. Wu and P. Yang. Germanium nanowire growth via simple vapor transport. Chemistry of Materials, 12(3):605–607, 2000.

[18] J. Westwater, D.P. Gosain, S. Tomiya, S. Usui, and H. Ruda. Growth of silicon nanowires via gold/silane vapor–liquid–solid reaction. J. Vac. Sci.Technol. B: Microelectronics and Nanometer Structures, 15(3):554–557, 1997.

[19] C.-C. Yeh C.-C. Chen. Large-scale catalytic synthesis of crystalline gallium nitride nanowires. 12 10:738–741, 2000.

[20] M. Lopez-Lopez, A. Guillen-Cervantes, Z. Rivera-Alvarez, and I. Hernandez-Calderon. Hillocks formation during the molecular beam epitaxial growth of znse on gaas substrates. Journal of Crystal Growth, 193(4):528–534, 1998.

[21] A. M. Morales and C. M. Lieber. A Laser Ablation Method for the Synthesis of Crystalline Semiconductor Nanowires. Science, 279(5348):208–211, 1998.

[22] I. Robin, R. Andre, C. Bougerol, T. Aichele, and S. Tatarenko. Elastic and surface energies: Two key parameters for cdse quantum dot formation. Applied Physics Letters, 88(23):233103, 2006.

[23] T. Aichele, M. Scholz, S. Ramelow, and O. Benson. Non-classical light states from single quantum dots, volume 53 of Advances in Atomic, Molecular, and Optical Physics, chapter 1. Academic Press USA, 2006, G. Rempe, M. Scully edition, 2006.

[24] Martien Den-hertog, M. Elouneg-Jamroz, E. Bellet-Amalric, S. Bounouar, C. Bougerol, R. Andre, Y. Genuist, J. P. Poizat, K. Kheng, and S. Tatarenko, Insertion of CdSe quantum dots in ZnSe nanowires: Correlation of structural and chemical characterization with photoluminescence, J. Appl. Phys. 110, 034318 (2011)

[25] Mandel and Wolf, Optical coherence and quantum optics, chapter 14, sec 2.

[26] R. Hanbury Brown & R. Q. Twiss, Correlation between Photons in two Coherent Beams of Light, Nature 177, 27 - 29 (07 January 1956)

[27] H. J. Kimble, M. Dagenais, and L. Mandel, Photon Antibunching in Resonance Fluorescence, Phys. Rev. Lett. 39, 691–695 (1977)

[28] H. J. Kimble, and L. Mandel, Theory of resonance fluorescence,Phys. Rev. A 13, 2123–2144 (1976)

[29] Mandel and Wolf, Optical coherence and quantum optics, chapter 15, sec 6.

[30] R. Short and L. Mandel, Observation of Sub-Poissonian Photon Statistics, Phys. Rev. Lett. 51, 384–387 (1983)

[31] Adrien Tribu, Gregory Sallen, Thomas Aichele, Regis Andre, Jean-Philippe Poizat, Catherine Bougerol, Serge Tatarenko and Kuntheak Kheng, A High-Temperature Single-Photon Source from Nanowire Quantum Dots, Nano Lett., 2008, 8 (12), pp 4326–4329

[32] R. Hanbury Brown & R.Q. Twiss, A Test of a New Type of Stellar Interferometer on Sirius. Nature 178, 1046 (1957)

[33] P. Michler, A. Kiraz, C. Becher, W. V. Schoenfeld, P. M. Petroff, Lidong Zhang, E. Hu, A. Imamoglu, A Quantum Dot Single-Photon Turnstile Device, Science 290, 2282 (2000).

[34] L. Besombes, K. Kheng, L. Marsal, and H. Mariette, Phys. Rev. B 63, 155307 (2001).

[35] T. Takagahara, Phys. Rev. B 60, 2638 (1999)

[36] Al. L. Efros, and M. Rosen, M. Nirmal, D. J. Norris, M. Kuno, and M. G. Bawendi, Band-edge exciton in quantum dots of semiconductors with a degenerate valence band: Dark and bright exciton states Phys. Rev. B 54, 4843 (1996).

[37] L. M. Woods, T. L. Reinecke, and R. Kotlyar, Phys. Rev. B 69, 125330 (2004)

[38] A. Grodecka, L. Jacak, P. Machnikowski, and K. Roszak, arXiv:cond-mat/0404364 (2004).

[39] A. Grodecka, C. Weber, P. Machnikowski, and A. Knorr, Phys. Rev. B 76, 205305 (2007)

[40] J. Puls, F. Henneberger, M. Rabe, and A. Siarkos, Journal of Crystal Growth 184/185, 787 (1998)

[41] O. Labeau, P. Tamarat, and B. Lounis, Phys. Rev. Lett. 90, 257404 (2003).

[42] M. Den Hertog, M. Elouneg-Jamroz, E. Bellet-Amalric, S. Bounouar, C. Bougerol, R. Andre, Y. Genuist, J.-Ph. Poizat, K. Kheng and S. Tatarenko, J. Appl. Phys. 110, 034318 (2011) (2011).

[43] G. Bacher, R. Weigand, J. Seufert, V. D. Kulakovskii, N. A. Gippius, and A. Forchel, Biexciton versus Exciton Lifetime in a Single Semiconductor Quantum Dot, Phys. Rev. Lett., 83 (21), 4417 (1999).

[44] M. Nirmal, D. J. Norris, M. Kuno, M. G. Bawendi, Al. L. Efros, and M. Rosen, Observation of the “dark exciton” in CdSe quantum dots, Phys. Rev. Lett. 75, 3728 (1995).

[45] H. J. Kimble, M. Dagenais, and L. Mandel. Photon Antibunching in Resonance Fluorescence. Phys. Rev. Lett. 39, 691 (1977).

[46] F. Diedrich and H. Walther. Nonclassical radiation of a single stored ion. Phys. Rev. Lett. 58, 203 (1987).

[47] B. Lounis and W. E. Moerner. Single photons on demand from a single molecule at room temperature. Nature 407, 491 (2000).

[48] A. Beveratos, R. Brouni, T. Gacoin, J.Ph. Poizat and P. Grangier. Single photon quantum cryptography. Phys. Rev. Lett. 89, 187901 (2002).

[49] Ch. Kurtsiefer, S. Mayer, P. Zarda, and H. Weinfurter: "A stable solid-state source of single photons", Phys. Rev. Lett. 85, 290 (2000).

[50] A. Hoegele, C. Galland. M. Winger. A. Imamoglu. Photon antibunching in the photoluminescence spectra of a single carbon nanotube. Phy. Rev. Lett 100, 217401 (2008).

[51] P. Michler, A. Kiraz, C. Becher, WV Schoenfeld, PM Petroff, L. Zhang, E. Hu, A. Imamoglu, Science 290, 2282 (2000)

[52] S. Kako, C. Santori, K. Hoshino, S. Gotzinger, Y. Yamamoto and Y. Arakawa. A gallium nitride single-photon source operating at 200K. Nature Materials, 5, 887 (2006).

[53] K. Sebald, P. Michler, T. Passow, D. Hommel, G. Bacher and A. Forchel. Single-photon emission of CdSe quantum dots at temperatures up to 200 K. Appl. Phys. Lett. 81, 2920 (2002).

[54] A. Tribu, G. Sallen, T. Aichele, R. Andre, J-Ph. Poizat, C. Bougerol, S. Tatarenko, K. Kheng. A high-temperature single photon source from nanowire quantum dots. Nano Letters 8, 4326 (2008).

[55] Xiaoyong Wang, Xiaofan Ren, Keith Kahen, Megan A. Hahn, Manju Rajeswaran, Sara Maccagnano-Zacher, John Silcox, George E. Cragg, Alexander L. Efros & Todd D. Krauss, Non-blinking semiconductor nanocrystals, Nature 459, 686-689 (2009)

[56] Benoit Mahler, Piernicola Spinicelli, Stephanie Buil, Xavier Quelin, Jean-Pierre Hermier, Benoit Dubertret, Towards non-blinking colloidal quantum dots, Nature Materials 7, 659 - 664 (2008)

[57] Bennett, C. H. & Brassard, G. Proc. IEEE Int. Conf. on Computers, Systems and Signal Processing 175–179 (IEEE, New York, 1984).

[58] Alexios Beveratos, Realisation experimentale d'une source de photons uniques par fluorescence de centres colores individuels dans le diamant ; application a la cryptographie quantique, these Universite Paris Sud - Paris XI (2002-12-20).

[59] G. Sallen, A. Tribu, T. Aichele, R. Andre, L. Besombes, C. Bougerol, S. Tatarenko, K. Kheng, and J. Ph. Poizat, Exciton dynamics of a single quantum dot embedded in a nanowire, Phys. Rev. B 80, 085310 (2009)

[60] Gregory Sallen, Spectroscopie optique de boites quantiques de CdSe inserees dans des nanofils de ZnSe, Universite Joseph Fourier, Grenoble.

[61] L. Besombes, K. Kheng, L. Marsal, and H. Mariette, Few-particle effects in single CdTe quantum dots, Phys. Rev. B 65, 121314 (2002)

[62] I. A. Akimov, K. V. Kavokin, A. Hundt, and F. Henneberger, Electron-hole exchange interaction in a negatively charged quantum dot, Phys. rev. b 71, 075326 (2005)

[63] Fine structure of the trion triplet state in a single self-assembled semiconductor quantum dot, I. A. Akimov, A. Hundt, T. Flissikowski, and F. Henneberger, Appl. Phys. Lett. 81, 4730 (2002)

[64] T. Warming, E. Siebert, A. Schliwa, E. Stock, R. Zimmermann, and D. Bimberg, Hole-hole and electron-hole exchange interactions in single InAs/GaAs quantum dots, Phys Rev B 79, 125316 (2009)

[65] S. Rodt, A. Schliwa, K. Petschke, F. Guffarth, and D. Bimberg, Correlation of structural and few-particle properties of self-organized InAs/GaAs quantum dots, Phys Rev B 71, 155325 (2005)

[66] Y. Igarashi, M. Shirane, Y. Ota, M. Nomura, N. Kumagai, S. Ohkouchi, A. Kirihara, S. Ishida, S. Iwamoto, S. Yorozu, and Y. Arakawa. Spin dynamics of excited trion states in a single InAs quantum dot, Phys. rev. B 81, 245304 2010.

[67] B. Urbaszek, R. J.Warburton, K. Karrai, B. D. Gerardot, P.M. Petroff, and J.M. Garcia, Phys. Rev. Lett. 90, 247403 (2003)

[68] J. Puls, I. A. Akimov, and F. Henneberger, Phys. Status Solidi B 234, 304 (2002)

[69] J. J. Finley, P. W. Fry, A. D. Ashmore, A. Lemaitre, A. I. Tartakovskii, R. Oulton, D. J. Mowbray, and M. S. Skolnick, Observation of multicharged excitons and biexcitons in a single InGaAs quantum dot, Phys. Rev. B 63, 161305 (R).

[70] C. Le Gall, Coherent control of a magnetic manganese spin in a CdTe/ZnTe quantum dot, Universite Joseph Fourier, Grenoble.

[71] Sebastian Moehl, Etude des proprietes optiques de boites quantiques semiconductrices II-VI pour leur application a l'emission a un photon a haute temperature,Universite Joseph Fourier, Grenoble.

[72] Piotr Wojnar, Elżbieta Janik, Lech T. Baczewski, Slawomir Kret, G. Karczewski, Tomasz Wojtowicz, Mateusz Goryca, Tomasz Kazimierczuk, and Piotr Kossacki, Growth and optical properties of CdTe quantum dots in ZnTe nanowires, Appl. Phys. Lett. 99, 113109 (2011).

[73] H. Y. Carr, E. M. Purcell, Effects of Diffusion on free precession in nuclear magnetic resonance experiments, Phys. Rev. 94, 630–638 (1954) .

[74] John M. Hayes, Gerald J. Small, Non-photochemical hole burning and impurity site relaxation processes in organic glasses. Chem. Phys., 27(1) :151, 1978.

[75] A. Empedocles, D. J. Norris, and M. G. Bawendi,Photoluminescence Spectroscopy of Single CdSe Nanocrystallite Quantum Dot, Physical Review Letters,77, 18, 2005

[76] Fluorescence intermittency in single cadmium selenide nanocrystals, Nature 383, 802 - 804 (1996)

[77] H. D. Robinson, Light-induced diffusion in single self-assembled quantum dots. Phys. Rev. B, 61(8) :R5086, 2000.

[78] N. Bloembergen, E. M. Purcell, and R. V. Pund. Relaxation effects in nuclear magnetic resonance absorption. Phys. Rev, 9(6) :935, 1947.

[79] Mahler B., Spinicelli P, Buil S. Quelin X., Hermier, J-P., Dubertret B., Towards non-blinking colloidal quantum dots. Nature materials, 7, 659 - 664 (2008)

[80] Xiaoyong Wang, Xiaofan Ren, Keith Kahen, Megan A. Hahn, Manju Rajeswaran, Sara Maccagnano-Zacher, John Silcox, George Cragg, Alexander L. Efros & Todd D. Krauss, Non-blinking semiconductor nanocrystals. Nature 459, 686-689 (2009)

[81] H. Peter. Lu, Luying Xun, and X. Sunney Xie. Single-Molecule Enzymatic Dynamics. Science, 282 :1877, 1998.

[82] M. Berg, C. A. Walsh, L. R. Narasimham, K. A. Littau, and M. D. Fayer. Dynamics in low temperature glasses : Theory and experiments on optical dephasing, spectral diffusion, and hydrogen tunneling. J. Chem. Phys, 88(3) :1564, 1988.

[83] Correlation between Fluorescence Intermittency and Spectral Diffusion in Single Semiconductor Quantum Dots R. G. Neuhauser, K. T. Shimizu, W. K. Woo, S. A. Empedocles, and M. G. Bawendi Phys. Rev. Lett. 85, 3301 (2000), 2000

[84] S. A. Empedocles and M. G. Bawendi, Influence of Spectral Diffusion on the Line Shapes of Single CdSe NanocrystalliteQuantum Dots, J. Phys. Chem. B, 103, 1826-1830, (1999)

[85] V. Turck, S. Rodt, O. Stier, R. Heitz, R. Engelhardt, U. W. Phol, D. Bimberg,and R. Steingruber. Effects of random field fluctuations on excitonic transitions of individual CdSe quantum dots. Phys. Rev. B, 61(15) :9944, 2001.

[86] Electric field dependence of optical absorption near the band gap of quantum-well structures, D. A. B. Miller, D. S. Chemla, T. C. Damen, A. C. Gossard, W. Wiegmann, T. H. Wood, and C. A. Burrus Phys. Rev. B 32, 1043 (1985)

[87] Quantum-Confined Stark Effect in Single CdSe Nanocrystallite Quantum Dots S. A. Empedocles and M. G. Bawendi Science 2114-2117 (1997)

[88] H. D. Robinson, BB Goldberg, Light-induced diffusion in single self-assembled quantum dots. Phys. Rev. B, 61(8) :R5086, 2000.

[89] J. Seufert, R. Weigand, G. Bacher, T. Kummell, A. Forchel, K. Leonard, and D. Hommel , Spectral diffusion of the exciton transition in a single self-organized quantum dot

[90] Few-particle effects in single CdTe quantum dots L. Besombes, K. Kheng, L. Marsal, and H. Mariette Phys. Rev. B 65, 121314 (2002)

[91] Bennett, C. H. & Brassard, G. Proc. IEEE Int. Conf. on Computers, Systems and Signal Processing 175–179 (IEEE, New York, 1984).

[92] Bouwmeester, D., Ekert, A. Zeilinger, A. The Physics of Quantum Information 49–92 (Springer,Berlin, 2000).

[93] Shih, Y. H. Alley, C. O. New type of Einstein–Podolsky–Rosen–Bohm experiment using pairs of light quanta produced by optical parametric down conversion. Phys. Rev. Lett. 61, 2921–2924(1988).

[94] Knill, E., Laflamme, R. Milburn, G. J. A scheme for efficient quantum computation with linear optics. Nature 409, 46–52 (2001).

[95] C. Santori, D. Fattal, J. Vuckovic, G. Solomon, and Y. Yamamoto, Nature 419, 594 (2002).

[96] Fan, X., Takagahara, T., Cunningham, J. E. Wang, H. Pure dephasing induced by exciton–phonon interactions in narrow GaAs quantum wells. Solid State Commun. 108, 857–861 (1998).

[97] R. Kubo. Note on the Stochastic theory of resonance Absorption. J. Phys .Soc. Jap, 9(6) :935, 1954.

[98] P. W. Anderson. A Mathematical Model for the Narrowing of Spectral Lines by Exchange or Motion. J. Phys. Soc. Jpn., 9 :316, 1954.

[99] A. I. Burshtein. Kinetics of the relaxation induced by a sudden potential change. Sov. Phys. JETP, 21(3) :567, 1965.

[100] A. I. Burshtein. Kinetics of induced relaxation. Sov. Phys. JETP, 22(4) :939, 1966.

[101] K. Wodkiewicz, B. W. Shore, and J. H. Eberly. Pre-Gaussian noise in strong laser-atom interactions. J. Opt. Soc. Am. B, 1(3) :398, 1984.

[102] K. Wodkiewicz, B. W. Shore, and J. H. Eberly. Noise in Strong laser-atom interactions : Frequency fluctuations and nonexponential correlations. Phys. Rev. A, 30(5) :2390, 1984.

[103] C.L. Nikias and A.P. Petropulu, Higher-Order Spectra Analysis: A Non linear Signal Processing Framework, Prentice Hall Inc., New Jersey: Englewood Cliffs, 1993

[104] A. Berthelot, I. Favero, G. Cassabois, C. Voisin, C. Delalande, Ph. Roussignol, R. Ferreira, and J. M. Gerard, Nature Phys. 2, 759 (2006).

[105] Alice Berthelot, Diffusion spectrale et retrecissement par le mouvement dans les boites quantiques, THESE de DOCTORAT de L'UNIVERSITE PARIS VI (2008)

[106] R. J. Cook and H. J. Kimble. Possibility of direct observation of quantum jumps. Phys. Rev. Lett, 54(10) :1023, 1985.

[107] Gregory Sallen, Spectroscopie optique de boites quantiques de CdSe inserees dans des nanofils de ZnSe, Universite Joseph Fourier, Grenoble.

[108] H.P. Trommsdorff, A. Corval, and L. von Laue Spectral hole burning: Spontaneous and photoinduced tunneling reactions in low temperature solids Pure Appl. Chem., Vol. 67, No. 1, pp. 191-198, 1995.

[109] Phedon Palinginis, Sasha Tavenner, Mark Lonerga, and Hailin Wang, Spectral hole burning and zero phonon linewidth in semiconductor nanocrystals, Phys. Rev. B 67, 201307(R) (2003)

[110] Taras Plakhotnik and Daniel Walser, Time Resolved Single Molecule Spectroscopy, Phys. Rev. Lett. 80, 4064-4067 (1998)

[111] Kammerer, C. et al. Interferometric correlation spectroscopy in single quantum dots. Appl. Phys. Lett.81, 2737 (2002).

[112] I. Favero,A. Berthelot, G. Cassabois, C. Voisin, C. Delalande, Ph. Roussignol, R. Ferreira, and J. M. Gerard Temperature dependence of the zero-phonon linewidth in quantum dots:Aneffect of the fluctuating environment, PHYSICAL REVIEW B 75, 073308 2007

[113] L. Coolen, X. Brokmann, P. Spinicelli, Emission characterization of a single CdSe-ZnS nanocrystal by high temporal and spectral resolution photon correlation Fourier spectroscopy, Phys Rev Lett., 100, 027403, (2003)

[114] G. Sallen, A. Tribu, T. Aichele, R. Andre, L. Besombes, C. Bougerol, M. Richard, S. Tatarenko,K. Kheng and J.-Ph. Poizat, Subnanosecond spectral diffusion measurement using photon correlation, Nature Photonics (2010)

[115] G. Sallen, A. Tribu, T. Aichele, R. Andre, L. Besombes, C. Bougerol, M. Richard, S. Tatarenko,K. Kheng and J.-Ph. Poizat, Subnanosecond spectral diffusion measurement using photon correlation, Supplementary informations Nature Photonics (2010)

[116] G. Sallen, A. Tribu, T. Aichele, R. Andre, L. Besombes, C. Bougerol, M. Richard, S. Tatarenko, K. Kheng, and J.-Ph. Poizat Subnanosecond spectral diffusion of a single quantum dot in a nanowire

[117] K. E. O'Hara, J. R. Gullingsrud, and J. P. Wolfe, Auger decay of excitons in Cu2O, Phys. Rev. B 60, 10872-10885 (1999)

[118] Lohner, A.,Woerner, M., Elsaesser, M. Kaiser,W. Picosecond capture of photoexcited holes by shallow acceptors in p-type GaAs. Phys. Rev. Lett. 68, 3920–3923 (1992).

[119] Imamoglu, A. et al. Quantum information processing using quantum dot spins and cavity QED. Phys. Rev. Lett. 83, 4204–4207 (1999).

[120] Chen, P., Piermarocchi, C., Sham, L. J., Gammon, D. & Steel, D. G. Theory of quantum optical control of a single spin in a quantum dot. Phys. Rev. B 69, 075320 (2004).

[121] David Press, Thaddeus D. Ladd, Bingyang Zhang & Yoshihisa Yamamoto, Nature, Vol 456 (2008).

[122] D. Meiser and M. J. Holland, Intensity fluctuations in steady-state superradiance, Phys Rev A 81, 063827 (2010).

[123] L. Besombes, K. Kheng, L. Marsal, and H. Mariette, Acoustic phonon broadening mechanism in single quantum dot emission, Phys. Rev. B 63, 155307 (2001)

[124] C. K. Hong, Z. Y. Ou, and L. Mandel, Measurement of subpicosecond time intervals between two photons by interference, Phys. Rev. Lett. 59, 2044–2046 (1987)

[125] Spyros Varoutsis, Generation de photons uniques indiscernables par une boite quantique semi-conductrice dans une microcavite optique, Universite Paris Sud - Paris XI (2005-11-18).

[126] Oliver Benson, Charles Santori, Matthew Pelton, and Yoshihisa Yamamoto, Regulated and Entangled Photons from a Single Quantum Dot, Phys. Rev. Lett. 84, 2513 (2000).

[127] J. Claudon, J. Bleuse, N. S. Malik, M. Bazin, P. Jaffrennou, N. Gregersen, C. Sauvan, P. Lalanne, and J.-M. Gerard, A highly efficient single-photon source based on a quantum dot in a photonic nanowire, Nature Photonics 4, 174 (2010).

[128] I. Friedler, C. Sauvan, J. P. Hugonin, P. Lalanne, J. Claudon, and J.-M. Gerard, Solid-state single photon sources: the nanowire antenna, Optics Express 17, 2095 (2009)

[129] Michael E. Reimer, Maarten P. van Kouwen, Maria Barkelid, Moira Hocevar, Maarten H. M. van Weert, Leo P. Kouwenhoven, Val Zwiller, Rienk E. Algra and Erik P. A. M. Bakkers, Mikael T. Bjork, Heinz Schmid, and Heike Riel, Single photon emission and detection at the nanoscale utilizing semiconductor nanowires, J. Nanophoton. 5, 053502 (2011)

[130] Michael A. Stroscio, K. W. Kim and SeGi Yu, Arthur Ballato, Quantized acoustic phonon modes in quantum wires and quantum dots, J. Appl. Phys. 76, 4670 (1994).

[131] Greta Lindwall, Andreas Wacker, Carsten Weber and Andreas Knorr, Zero-Phonon Linewidth and Phonon Satellites in the Optical Absorption of Nanowire-Based Quantum Dots, Phys. Rev. Lett. 99, 087401 (2007).

Annexe: Random processes

The concept of a random process represents a generalization of the idea of a set of random variables $x_1, x_2, x_3, ...$, when the set is no longer countable and the variables form a continuum. We therefore introduce a continuos parameter t, representing the time, that labels the variates. We call x(t) a random process if x does not depend on t in a deterministic way.

Stationnarity

Random functions of time frequently have the property that the character of the fluctuations does not change with time, even though any realization of the ensemble x(t) changes continually in time. Such process is said to be statistically stationary. We call a random process process stationary if all the probability densities p_1, p_2, p_3,... governing the fluctuations are invariant under an arbitrary translation of the origine of time ie. if, for all T:

$$p_n(x_n, t_n, x_{n-1}, t_{n-1}, ..., x_1, t_1) = p_n(x_n, t_n + T, x_{n-1}, t_{n-1} + T, ..., x_1, t_1 + T)$$

Under these circumstances, the expectation values of $x(t_1)$, $x(t_2)$ and $x(t_3)$... are also invariant under time translation.

And one can show the correlation function has the following property:

$$\Gamma(t_1, t_2) = \langle x(t_1)x(t_2)\rangle = \Gamma(t_1 - t_2)$$

Poissonian process

A Poisson process at rate is a renewal point process in which the interarrival time distribution is exponential with rate : interarrival times $\{X_n : n \geqslant 1\}$ are i.i.d. with common distribution$F(x) = P(X \leq x) = 1 - e^{-\lambda x}$, $x \geq 0$; $E(X) = 1/\lambda$.

The reason that the Poisson process is named so is because: For each fixed t $>$ 0, the distribution of N(t) is Poisson with mean λt:

$$P(N(t) = k) = e^{-\lambda t}\frac{(\lambda t)^k}{k!}$$

with $k \geq 0$.

In particular, $E(N(t)) = t$, $Var(N(t)) = \lambda t$, $t \geq 0$. In fact, the number of arrivals in any interval of length t, N(s + t) - N(s) is also Poisson with mean λt:

$$P(N(s + t) - N(s) = k) = e^{-\lambda t}\frac{(\lambda t)^k}{k!}$$

with $s > 0$, $k \geq 0$, and $E(N(s + t) - N(s)) = \lambda t$, $Var(N(s + t) - N(s)) = \lambda t$, $t \geq 0$.

$N(s+t) - N(s)$ is called a length t increment of the counting process $\{N(t) : t \geq 0\}$; the above tells us that the Poisson counting process has increments that have a distribution that is Poisson and only depends on the length of the increment. Any incrementof length t is distributed as Poisson with mean λt. This is an example of a process having stationary increments: Any increment of length t has a distribution that only depends on the length t. The Poisson process also has independent increments, meaning that non-overlapping increments are independent: If $0 \leq a < b < c < d$, then the two increments $N(b) - N(a)$, and $N(d) - N(c)$ are independent intervalls.

Remarkable as it may seem, it turns out that the Poisson process is completely characterized by stationary and independent increments:

Suppose that is a simple random point process that has both stationary and independent increments. Then in fact, is a Poisson process. Thus the Poisson process is the only simple point process with stationary and independent increments.

Gaussian process

Gaussian process is a stochastic process whose realisations consist of random values associated with every point in a range of times (or of space) such that each such random variable has a normal distribution. It can be completely defined by its mean value $\langle x(t) \rangle$ and its correlation function $\langle x(t_1)x(t_2) \rangle$. A gaussian process is not necessarily stationary.

First order markovian process

Unlike the poissonian process, which is independant of its history, the first order markovian process is influenced by its immediate or most recent past. Its probability density satisfies the equation:

$$p_{n,k}(x_{k+n}, t_{k+n}; ...; x_{k+1}, t_{k+1} \mid x_k, t_{k;}..., x_1, t_1) = p_{n,1}(x_{k+n}, t_{k+n}; ...; x_{k+1}, t_{k+1} \mid x_k, t_{k;})$$

with $(t_1 \leq t_2 \leq t_3 ...)$

The most recent past governs the time evolution of the process.

One can show that the joint probability of n events governed by a Markovian process can be decomposed as follows:

$$p_n(x_n, t_n, x_{n-1}, t_{n-1}, ..., x_1, t_1) = p(x_n, t_n \mid x_{n-1}, t_{n-1}) p(x_{n-1}, t_{n-1} \mid x_{n-2}, t_{n-2}) \ldots p(x_1, t_1 \mid x_1, t_1) p(x_1, t_1)$$

The telegraph noise process is a first order markovian process.

Résumé

Le travail proposé dans cette thèse est basé sur des expériences de corrélation de photons faites sur un émetteur de photons uniques semi conducteur: une boite quantique de CdSe dans un nanofil de ZnSe. La première démonstration de production de photons uniques d'une boite quantique épitaxiée à température ambiante y est présentée. La transition biexcitonique est la source utilisée et son rapide taux d'émission spontanée (temps de vie radiatif de 300 ps) en fait un emetteur extremement rapide. Pour expliquer ce résultat, nous avons étudié expérimentalement et théoriquement l'efficacité de couplage exciton-phonon et ses conséquences sur l'intensité de l'exciton avec la température. Nous présentons également des résultats optiques portant sur la robustesse de cette structure à haute température. La technique de corrélation de photons est également appliquée sur des boites quantiques chargées. La présence du biexciton chargé nous a permis de sonder la structure fine du trion excité, de décrire ses processus de relaxations et d'obtenir une mesure directe du temps de spin flip du trou sur l'état p. Des indications sont également données sur la nature possible du dopage. Nous avons aussi étudié la diffusion spectrale de l'émetteur causée par les fluctuations électroniques de son environnement. Par un travail théorique nous montrons comment interpréter l'effet de l'élargissement phonon de la raie homogène, (processus Poissonien) combiné avec l'effet de la diffusion spectral (processus Markovien) sur la fonction d' autocorrélation de la demi-raie. Grace à l'expérience, nous concluons sur la statistique de l'énergie d'émission de l'émetteur à haute température. Nous appliquons cette théorie sur les nanofils et interprétons les dépendances en température et en puissance des fluctuations de l'environnement grace au modèle de Kubo-Anderson.

Summary

The work proposed in this thesis is based on photon correlation experiments performed on a semi-conductor single photon emitter: CdSe/ZnSe nanowire quantum dot. Is presented the first demonstration of single photon emission at room temperature from an epitaxied quantum dot. To explain this result we investigated by a theoretical and experimental study, the exciton-phonon coupling efficiency and its consequence on the exciton luminescence intensity with temperature. We also present optical results on the robustness against temperature of this structure. Photon correlations techniques are also applied on charged quantum dots. Presence of the charged biexciton allowed to probe the fine structure of the excited trion, to describe its carrier relaxation processes, and to obtain a direct measurement of the p-shell hole spin flip time. Indications are also given on the possible doping nature. We also investigated spectral diffusion of the emitter caused by electronic fluctuations of the environnement. By a theoretical work, we show how to model the effect of the homogeneous phonon broadening, (poissonian emission energy process) combined with the spectral diffusion effect (markovian emission energy process) on the half line autocorrelation function. Thanks to experiments, We conclude on the statisic of the emission energy of the emitter at high temperature. We apply this theory on CdSe/ZnSe nanowire quantum dots and interpret temperature and power dependance of the environnement

fluctuation thanks to the Kubo-Anderson Model.